Water Vapor Absorption Thermometry for Practical Combustion Applications

by

Andrew W. Caswell

A dissertation submitted in partial fulfillment of the

requirements for the degree of

Doctor of Philosophy

(Mechanical Engineering)

at the

UNIVERSITY OF WISCONSIN-MADISON

2009

WATER VAPOR ABSORPTION THERMOMETRY FOR PRACTICAL COMBUSTION APPLICATIONS

Andrew W. Caswell

Under the supervision of Associate Professor Scott T. Sanders

At the University of Wisconsin – Madison

Thermometry in combustion applications by means of laser absorption spectroscopy is a well established diagnostic. The experimental simplicity and wealth of knowledge that can be readily gained from an absorption spectrum makes it often times the diagnostic of choice when interrogating the flow fields of practical combustion devices such as internal combustion engines.

This project develops techniques for optimizing the design of absorption based sensors by providing strategies for selecting optimal wavelengths in order to improve thermometry. Descriptive relations are derived in order to predict the performance of an absorption based sensor and through numerical optimization, ideal selections of wavelengths can be made.

Furthermore, this work applies novel hyperspectral lasers to practical combustion environments in order to infer gas properties based on direct absorption spectroscopy. The measurements are designed for high-speed (30 kHz and up) data rates of useful engineering parameters such as temperature and species concentration. Measurements have been performed across the cylinder of an optically accessible HCCI engine using a rapidly-swept (5 μs measurement time) broad wavelength (1333-1377 nm) tunable laser. Temperature results were obtained at 100 kHz with 0.25% RMS precision at a temperature of 1970 K.

ACKNOWLEDGMENTS

This work would not have been possible without the support and guidance of Professor Scott Sanders. His ubiquitous enthusiasm for the subject matter is contagious and it provided a constant source of inspiration

I also would like to express my gratitude towards the rest of my faculty defense committee: Professors Jaal Ghandhi, Dave Rothamer, John Wright and Claude Woods.

The sheer number of the exceptional people I have been honored to have the opportunity to work with makes it difficult to name any single one of them and I will be forever indebted to the many students from the Sanders group and the Engine Research Center for providing me their valuable time and friendship. However, the insightful discussions over the years with Laura Kranendonk, Chris Hagen, and Randy Herold have only allowed me to grow both personally and professionally. I would like to thank Keith Rein for his willingness to drop everything for a trip to Dayton, Xinliang An for his enthusiasm in taking data at all hours of the night, and Thilo Kraetschmer for too many reasons to elaborate.

My time at the university would not have been possible without the love and support of my parents and I will be forever grateful for the opportunities they've given me.

Finally, I would like to thank my wife, Tarina, for her unwavering support, friendship, and love.

TABLE OF CONTENTS

TABLE OF FIGURES

LIST OF TABLES

CHAPTER 1. INTRODUCTION

The foundation of this research is based on developing a better understanding of how to perform direct absorption spectroscopy measurements in practical combustion environments in order to infer gas properties such as temperature and absorber concentration. The work presented here focuses solely on water vapor absorption but the main ideas should be tractable to other gas phase species.

Optical diagnostics are a useful tool for performing measurements in practical combustion environments owing to their inherent ability to probe the sample gas without disrupting the flow field. Contrast this to other techniques for measuring temperature, such as thermocouples and sample probe based methods where insertion errors must always be considered. Direct absorption spectroscopy is especially attractive given the fact that it provides a measure of the gas properties irrespective of any type of calibration and is typically only limited in accuracy to the degree in which the absorbers fundamental spectroscopy is known.

Absorption spectroscopy, specifically H_2O absorption, is not without its challenges. Limited optical access, interferences in the optical path, beamsteering, and a multitude of other bias and precision error sources tend together to make the act of measuring the spectrum in the harsh environment of a modern combustion system difficult at best. This is especially true when the goal is to capture the dynamic nature of these systems requiring overall measurement rates on the order of tens of kilohertz.

1.1 MOTIVATION

Many descriptions of gas sensing using diode lasers are not uncommon [1-4]. Much work has been put forth expanding the applicability of absorption based sensors to practical flows of interest and much progress has been made in expanding the usefulness of the results obtained with these sensors [5, 6].

When considering a measurement in a combustion application, one of the first key choices is the decision of the species to probe. The ubiquity of water vapor throughout the entire thermodynamic cycle of nearly all practical heat engines makes it a prime candidate. For instance, it is usually naturally abundant in the intake air streams and is a major product of combustion of hydrocarbon and other hydrogen-containing fuels. Water also has the desirable characteristic of having spectroscopic transitions in the spectral region where modern semiconductor and fiber optic components have undergone much development owing to the large telecom market that utilizes this same spectral range.

In the past, typical H_2O absorption thermometry sensors have been based on measuring two points in the spectrum (either at a single wavelength or tuning over an entire feature) and inferring the temperature from the ratio of these measurements [7]. More recently, high speed thermometry has been performed utilizing broadly tunable lasers and discrete color time division multiplexed lasers [4,8-10].

Driven by ever advancing laser source development, a methodology for choosing appropriate wavelengths for optimizing thermometry is needed now more than ever. The sensor design no longer is limited by the availability of lasers but rather the source can be engineered to meet the requirements of the sensor. Complicating the wavelength selection problem even

further is the latest work on transitioning from a single line-of-sight absorption measurement to a two dimensional measurement through tomographic reconstructions of data recorded along many lines of sight [11,12]. Hyperspectral tomography based on H_2O absorption spectroscopy offers the promise of truly quantitative 2D representations of the scalar temperature and concentration field but current reconstruction techniques are costly in computation and would benefit from measurements that focused on the key points in the spectrum that offer the best temperature sensitivity.

1.2 THESIS OVERVIEW

The progression of this thesis is as follows:

Chapters 2-4 will introduce novel ideas and practices for absorption thermometry experiments in practical combustion applications

Chapter 2 offers the reader a background in H_2O absorption spectroscopy and how it relates to inferring gas properties such as temperature and absorber mole fraction

Chapter 3 will offer ideas for solving the wavelength selection problem. Novel semiconductor based lasers have recently been developed that permit an almost arbitrary selection of output wavelength versus time [13,14]. The standard 2 color ratiometric technique doesn't directly apply to experiments utilizing these multi-color, dynamic light sources. The selection of wavelengths can pose multiple challenges to the sensor designer and some rules/guidelines for optimizing these selections are put forth.

Chapter 4 Gives real world practical examples of applying some of the techniques presented here utilizing some of the latest diode laser based sensors. Three specific measurement

campaigns are highlighted with each having its own flavor whilst all three sharing the common theme of inferring the gas temperature and water concentration through absorption spectroscopy.

Finally, Chapter 5 will conclude this thesis with a summary of main concepts and important results presented in this thesis with a few recommendations for future work.

CHAPTER 2. H_2O ABSORPTION THERMOMETRY

The use of absorption spectroscopy for measuring gas properties in combustion applications has been well researched and documented [15-18]. H_2O as the target absorber has been given much attention owing to its ever abundant presence in both the air used in most practical combustors and as a major product of hydrocarbon combustion [4,16,19-21]. This constant presence along with available absorption bands in the telecom range of wavelengths (1300-1550 nm) allows it to be a key probe species when using optical interrogation methods to study the performance of practical combustors. However, the spectroscopy of the H_2O molecule is not simple and much empiricism must be used to effectively apply these techniques to real world sensors.

Absorption spectroscopy is a simple linear technique used to study the quantized energy levels of an atom or molecule. It provides quantitative information about the population of molecules inhabiting their various energy levels. Assuming local thermodynamic equilibrium (LTE), the population distribution of these energy levels is governed by the Boltzmann distribution which is a function of the gas temperature. Temperature can be inferred by measuring the relative population in two or more distinct energy levels.

There are two primary classes of wavelength management techniques used for gas thermometry by absorption spectroscopy. One technique involves using multiple, discrete wavelengths supplied by either single color multiplexed laser sources or a single source that outputs different colors multiplexed in time and the other technique relies on a continuous wavelength scan over a broad range of wavelengths. This continuous scanned technique can be achieved by using either a monochromatic laser that can tune its color in time or using a

broadband light source and dispersing the light and capturing the various colors in time with a single detector or capturing multiple colors at the same time with an array detector. Each of the two primary wavelength management techniques have pros and cons associated with them and the selection of one over the other may be application driven. With the advent of current semiconductor gain media and fiber optic technology an almost arbitrary selection of wavelengths is possible with a single laser source opening the door to more advanced and innovative thermometry experiments while at the same time complicating the choices to be made by the sensor designer.

2.1 H_2O SPECTROSCOPY FOR SENSOR APPLICATIONS

Perhaps the single most important tool in the experimental spectroscopist's toolbox is the Beer-Lambert relation that relates the fractional transmission of a laser beam passing through an absorbing medium to an absorption coefficient.

$$\left(\frac{I}{I_o}\right)_{\nu,x} = \exp\left(-\int_0^L k(y;\nu)dy\right) \tag{2.1}$$

For a 2D problem, this is the general form of the relation when considering a single absorber with non-uniform properties. In this equation, Io is the intensity of a laser beam at some location x before it passes through the absorbing medium, I is the intensity after passing through the sample, L is the length of the sample where absorption occurs, and k_ν is the spectral absorption coefficient. In this form of the equation, the spectral absorption coefficient is allowed to vary along the length of the beam in the y dimension and thus must

be included inside the integral over the length. If the gas properties are assumed uniform along the entire path of the laser beam, this relation can be simplified to the following form.

$$\left(\frac{I}{Io}\right)_{\nu} = \mathrm{e}^{(-k_{\nu}L)} \tag{2.2}$$

This form of Beer's law is the one most commonly presented and forms the basis for quantitative absorption spectroscopy experiments. However, in order to infer gas properties, the dependence of the spectral absorption coefficient on temperature, pressure, and absorber mole fraction must be known or reliably predicted. For thermometry experiments, it would be ideal to measure the absorbance at the wavelengths of interest over the conditions hypothesized for the problem in order to create an empirical database of spectra to be used for comparison to further measurements at unknown conditions. In practice, this is often difficult to obtain under highly controlled conditions and furthermore concomitant measures of the gas temperature may be unreliable. For these reasons, gas temperature sensing using H_2O absorption spectroscopy is often done by comparing measurements to simulated spectra.

2.2 SPECTRAL DATABASES

For quantitative absorption measurements in practical combustors, the experimental results usually are the result of comparing the measurements to simulated spectra. In order to accurately simulate a spectrum, one usually refers to a spectral line list comprised of the pertinent parameters necessary to evaluate the absorption coefficient. For the water molecule, two spectral line lists have received the most attention for combustion sensor design.

2.2.1 HITRAN

The HITRAN (HIgh-resolution TRANsmission molecular absorption database) database is currently in version 2004 after its beginnings in the 1960s at the Air Force Cambridge research labs [22]. In addition to H_2O, HITRAN contains infrared spectroscopic parameters for 39 total molecules with the choice of species tailored to the atmospheric sciences researcher. A variant of the HITRAN database exists that is more suitable to combustion applications. The HITEMP database uses the same data contained in HITRAN but employs a smaller line intensity cutoff used for reducing the number of included transitions and this reduces the chance of an important line missing when simulating high temperature spectra.

The data of relevance to simulating the absorption spectrum included in these compilations are the line center frequency in units of cm^{-1}, the intensity (also commonly called the line strength, S), the lower state energy of the transition (E”), and the parameters for estimating the spectral widths when using a Voigt lineshape function.

2.2.2 BT2

The need for an all encompassing solution for simulating the H_2O spectrum has been of great interest not only for the combustion diagnostic community but for a wide range of applications and studies such as astrophysics. Building on this need, the THAMOS group at University College London led by Jonathon Tennyson developed the entirely synthetic H_2O line list BT2 [23]. Using a variational technique in conjunction with highly accurate potential energy and dipole moment surfaces, the BT2 database is the most complete and accurate H_2O line list to date (221,097 energy levels, cut-offs of J=50 and E”=30,000 cm^{-1}, and totaling 505,806,202 transitions) [23]. With that being said, experimental validation of the database is

an ongoing project and one that will continue to be necessary since only ~80,000 out of the approximately 1 billion transitions are known experimentally.

Unlike HITRAN/HITEMP, BT2 does not contain any information related to modeling the line shape function. For the combustion researcher, this poses added complexity to the sensor design since most practical combustors operate at pressures at and above where collisional broadening mechanisms begin to dominate. Assumptions on the lineshape can have greatly varying results on the calculated absorbance which in turn can substantially affect parameters inferred from the spectrum such as the absorbers number density and temperature (see section 4.1). However, the greatly improved line intensities (especially at elevated temperatures) and higher number of included transitions versus HITEMP has made the BT2 database an invaluable tool to the H_2O laser absorption sensor designer.

2.2.3 Comparing the databases

The HITRAN and HITEMP spectral line lists have become an accepted standard for simulating absorption spectra in combustion studies, especially for the most abundant isotope of water, $^{1}H_2{}^{16}O$, even though the primary focus of the HITRAN database is for terrestrial atmospheric transmission simulations [22]. Discrepancies between measured H_2O vapor spectra and HITRAN simulations are evident when comparing results at typical combustion temperatures (T >1000 K). The sources of these discrepancies include a lack of quality high temperature experimental spectra for updating line parameters in HITRAN, and the standard temperature ($T_{o,\ HITRAN}$ = 296 K) intensity cut-off used when compiling the HITRAN database. While the HITEMP database doesn't utilize the same low temperature cut-off, the database has not been updated as regularly as HITRAN. However, when considering high

temperature water vapor, HITEMP is the appropriate choice versus HITRAN due to the inclusion of more lines with high lower state energies [24].

With improvements in light sources and experimental techniques used to acquire absorption spectra of hot water vapor, there is a strong need for a more complete water line list to more accurately infer temperature in combustion environments. The BT2 spectral line list of Barber and Tennyson is a computed line list that is aimed towards providing spectral line parameters valid for temperatures of up to at least 4000 K and has proven to be more complete than any other line list in existence [23].

Optical combustion studies using absorption or emission spectroscopy often rely heavily on spectral line lists of the species of interest. For simulating a detailed absorption or emission spectrum, the minimum information needed is the line center frequency, ν [cm^{-1}], the temperature dependent line intensity, S(T) [cm/molecule], and the lower state energy [cm^{-1}] of each transition in a desired spectral range. From this information, a spectrum can be simulated by dressing each transition with an appropriate line shape function. The HITRAN database provides information for the pressure and temperature dependent line broadening coefficients for collision broadened lines to include in the line shape function where as BT2 only provides information for modeling the line position and intensity. To simulate spectra using BT2, the Doppler line width was computed for each line position and a Voigt profile was applied using a uniform Lorentzian width based on the average experimental width for the entire spectrum.

While H_2O absorption simulations utilizing HITRAN agree well with experiments at low temperatures, there are often large discrepancies at high temperatures. The differences arise

from missing transitions at high rotational quantum numbers, J, and lines from upper vibrational states. These hot lines and bands provide negligible absorption at atmospheric conditions but are important in high temperature combustion studies. In order to accurately simulate high temperature water spectra, the BT2 database employs a J cutoff of 50 and energy level cutoff of 30000 cm^{-1}, which allows for nearly all lines, especially in the infrared, to be listed [23].

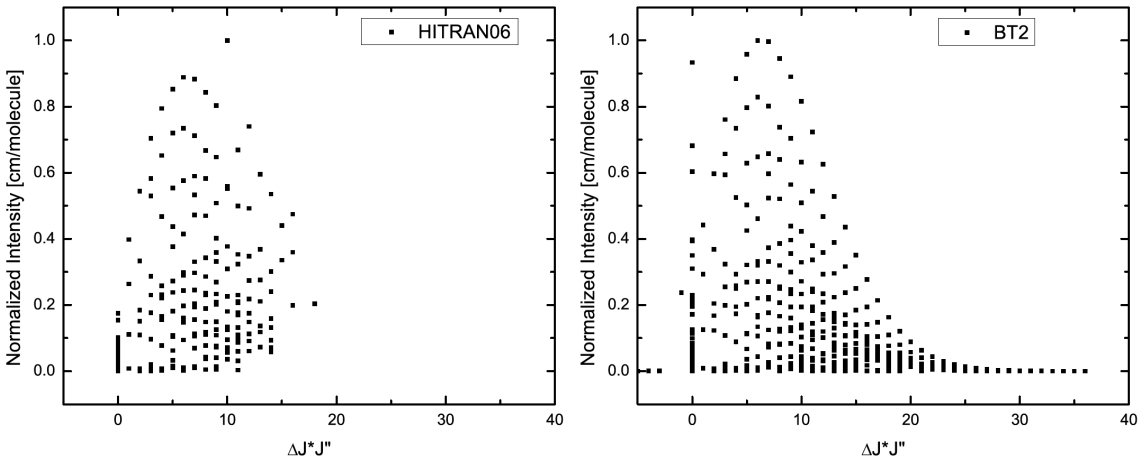

Figure 2.1 Shown are the normalized line intensities versus rotational quantum number J for the R branch of the $\nu_1+\nu_3$ band of water (~1330-1370 nm) for the HITRAN (left) and BT2 (right) databases. The exclusion of high rotational energy lines is evident in the HITRAN data versus the completeness of the BT2 database.

An example of the completeness of the BT2 database can be seen in the experimental H_2O vapor absorption spectrum recorded during the combustion stroke of a homogeneous charge compression ignition (HCCI) internal combustion engine. This engine provides nearly homogeneous gas samples appropriate for single line-of-sight absorption measurements. Spectra were acquired every 0.25 crank angle degree (CAD) using an advanced swept-wavelength laser source that scanned from 7245 – 7520 cm^{-1} every 5 μs [4]. Each spectrum

was compared to a library of HITEMP simulations to find the best-fit temperature of the gases in the cylinder. Plotted in Figure 2.2 is a subset of the spectrum measured at top dead center (TDC) along with simulation results from three different spectral databases; the best fit HITEMP spectrum at the inferred temperature of 1500 K, a HITRAN simulation at 1500 K and simulations using the BT2 database at temperatures of 1500 K and 2200 K. It is easily seen that the BT2 simulation provides a better fit at 1500 K than the HITRAN or HITEMP simulations and even better visual agreement at a temperature of 2200 K. These results provide evidence of HITRAN's propensity to bias results toward colder temperatures when fitting spectra recorded in combustion environments.

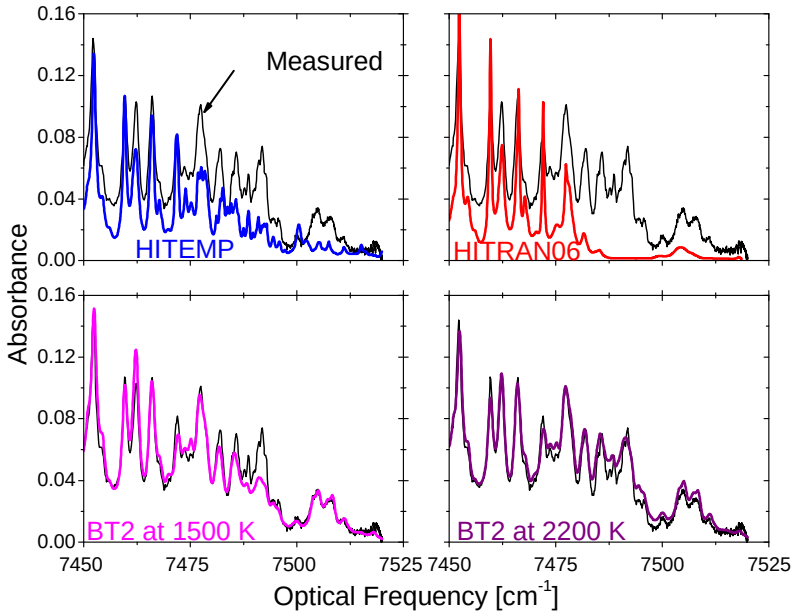

Figure 2.2 Subset of spectrum recorded in HCCI piston engine at top dead center (TDC). The cylinder pressure was 31.8 bar and the absorption path length 9.5 cm. Plotted against the experimental spectrum are simulations using multiple databases: HITEMP, HITRAN, and BT2. The HITEMP and HITRAN simulations are at 1500 K which was the inferred temperature from fitting to the HITEMP library. The BT2 simulations show improved agreement at 1500 K and even better agreement at 2200 K.

The above result is corroborated by comparisons of best-fit temperatures derived from the HITEMP and BT2 databases independently. In a steady gas turbine combustor test facility, H_2O vapor absorption measurements were performed using the same swept-wavelength sensor used to obtain the piston engine data shown in Figure 2.2[25]. During this test, gas was sampled from the combustion zone and a concomitant temperature was determined from the gas composition using a chemical equilibrium analysis. Measured spectra were fit to a library of HITEMP and BT2 simulations in order to infer the temperature. Figure 2.3 shows the measured temperature from the absorption spectra plotted versus the temperature from the gas sampling calculations. The equivalence ratio and pressure were varied to produce the varied operating temperatures. The cold bias of HITEMP results at high temperatures is again evident, whereas the BT2 results follow the actual gas temperatures to within the uncertainty visible from the scatter in the data.

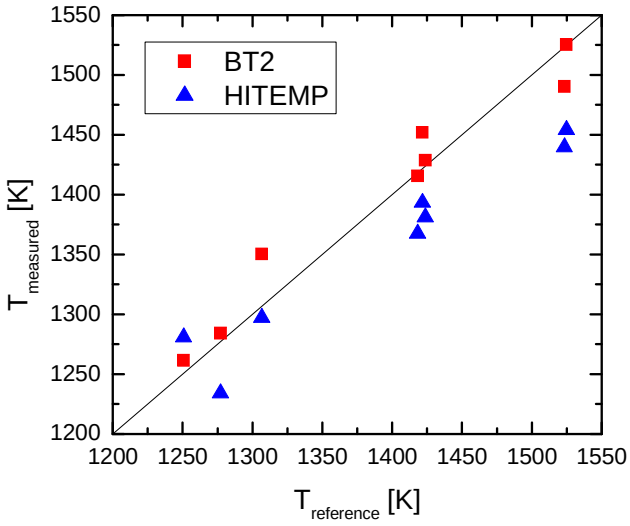

Figure 2.3 Temperatures inferred from infrared water vapor absorption versus temperatures calculated from gas sampling. The cold bias is readily seen in the HITEMP results whereas the BT2 data more closely follows the ideal trend line.

From experimental evidence, the BT2 database can provide higher temperature results when compared to HITRAN. This database provides an alternative to HITRAN for either designing or interpreting results from water vapor absorption experiments conducted at elevated temperatures. While BT2 does not provide any input parameters for lineshape modeling, the inclusion of high lower state energy lines improves sensitivity at elevated temperatures. An assumption of uniform Lorentzian linewidth across spectra spanning ~ 250 cm^{-1} in the 7200 cm^{-1} range, although strictly incorrect, resulted in negligible error for the experiments considered here.

In addition to improved thermometry, there are other benefits of advanced databases such as BT2. As an example, H_2O_2 and H_2O properties were inferred from experimental spectra containing contributions from both species. Since H_2O was the stronger absorber, the strategy was to subtract simulated H_2O spectra from the measured spectra to reveal H_2O_2 spectra. However, intensity imperfections in the HITEMP database caused the residual spectrum to retain H_2O contamination. Using BT2, there is better access to absorbers weaker than H_2O when analyzed in this fashion [26].

2.3 TWO COLOR RATIOMETRIC THERMOMETRY

For a typical H_2O absorption experiment, the absorption is quantified using the Beer-Lambert relation discussed earlier and repeated here in equation 2.3 for simplicity.

$$\left(\frac{I}{Io}\right)_{\nu} = \mathrm{e}^{(-k_{\nu}L)} \tag{2.3}$$

This relation relates the ratio of the laser intensity (W/cm^2, W/cm^{2}s^{-1} or W) incident on the sample (Io) and the intensity after passing through the sample (I) to the product of the length, L, of the sample and the spectral absorbance coefficient, k_ν. This product, $k_\nu L$, is termed the absorbance, α, and can be related to more fundamental parameters of the species of interest.

$$\alpha_\nu = k_\nu L = N \cdot L\left(\sum_i S_i(T) \cdot \phi\left(\nu - \nu_i, T, P, x\right)\right) \tag{2.4}$$

This equation shows that the magnitude of the absorbance at a frequency, ν, depends on the absorber number density N, the length of the path in which the absorber is present, and the weighted sum of line strengths, S_i, of absorption transitions in the vicinity of ν with the weighting factor being determined through a line shape function ϕ.

In order to make a temperature measurement, two separate wavelengths are chosen and the ratio of their absorbances is computed. For simplicity, if it is assumed that the chosen wavelengths are the result of absorbance from a single transition (i.e. the transitions are isolated) the ratio can be written as:

$$R(T) = \frac{\alpha_{\nu 1}}{\alpha_{\nu 2}} = \frac{S_1(T)}{S_2(T)} \cdot \frac{\phi_1(\nu_1 - \nu_{1,0})}{\phi_2(\nu_2 - \nu_{2,0})} \tag{2.5}$$

If it is further assumed that collisional broadening dominates the line shape function and that the resulting Lorentzian lineshape is the same for both chosen wavelengths, the ratio then becomes the following pure function of temperature.

$$R(T) = \frac{S_1(T)}{S_2(T)} \tag{2.6}$$

The line strength $S_i(T)$ can be calculated from the line strength at a known temperature using the following scaling relationship [27].

$$S_i(T) = S_i(T_0)\frac{Q(T_0)}{Q(T)}\exp\left[-\frac{hcE_i^{"}}{k}\left(\frac{1}{T}-\frac{1}{T_0}\right)\right]\left[1-\exp\left(\frac{-hc\nu_{0,i}}{kT}\right)\right]\left[1-\exp\left(\frac{-hc\nu_{0,i}}{kT_0}\right)\right]^{-1} \quad (2.7)$$

Inserting equation 2.7 into equation 2.6 yields the following function for the ratio when neglecting the induced emission ($1-e^x$) terms which is valid given the frequencies and temperatures involved for near infrared combustion studies (i.e. low upper state populations).

$$R(T) = \frac{S_1(T_0)}{S_2(T_0)}\exp\left[-\left(\frac{hc}{k}\right)\left(E_1^{"}-E_2^{"}\right)\left(\frac{1}{T}-\frac{1}{T_0}\right)\right] \quad (2.8)$$

From this expression, the temperature sensitivity for the chosen line pair can be found by differentiating equation 2.8 with respect to T.

$$\frac{dR}{dT} = \left(\frac{hc}{k}\right)\frac{\left(E_1^{"}-E_2^{"}\right)R}{T^2} \quad (2.9)$$

In practical combustion applications, the assumption of isolated lines is often difficult to use especially when the pressures are high and significant blending and overlap occurs. In practice, it's often easier to work directly with the absorbance values. Typically, the absorption coefficient is simulated for the wavelengths of interest over a postulated temperature range and a calibration curve R(T) is computed from which the temperature can be found.

2.4 HYPERSPECTRAL THERMOMETRY

Extending the analysis of temperature inference from spectral measurements at two wavelengths to N wavelengths is not trivial. For instance, assuming the absorber concentration and the gas pressure is known, measurements of 3 wavelengths results in at most 3 equations with a single unknown temperature. Therefore, a simple yet robust methodology is needed for dealing with measurements consisting of multiple wavelengths.

2.4.1 Linear system of equations

One possible method would be to solve a linear system of equations based on simulations at various temperatures such as **Ax** = **b**. A possible formulation is as follows:

$$\begin{bmatrix} k_{T_1,\nu_1} & \cdots & k_{T_1,\nu_n} \\ \vdots & \ddots & \vdots \\ k_{T_m,\nu_1} & \cdots & k_{T_m,\nu_n} \end{bmatrix} \begin{bmatrix} x_1 \\ \vdots \\ x_n \end{bmatrix} = \begin{bmatrix} T_1 \\ \vdots \\ T_m \end{bmatrix} \tag{2.10}$$

Upon solving this set of equations for the vector **x**, one can make a measurement at an unknown T (within the calibration range $T_1 \ldots T_m$) and multiply the measured row vector by **x** to obtain the temperature. If the number of wavelengths and temperatures is the same then the solution is exact for the temperatures considered but interpolation errors will exist when attempting to use the result at some other intermediate temperature. In the more general $m \times n$ case, there will be exactly m or n exact solutions depending on which is smaller of the two as shown in Figure 2.4.

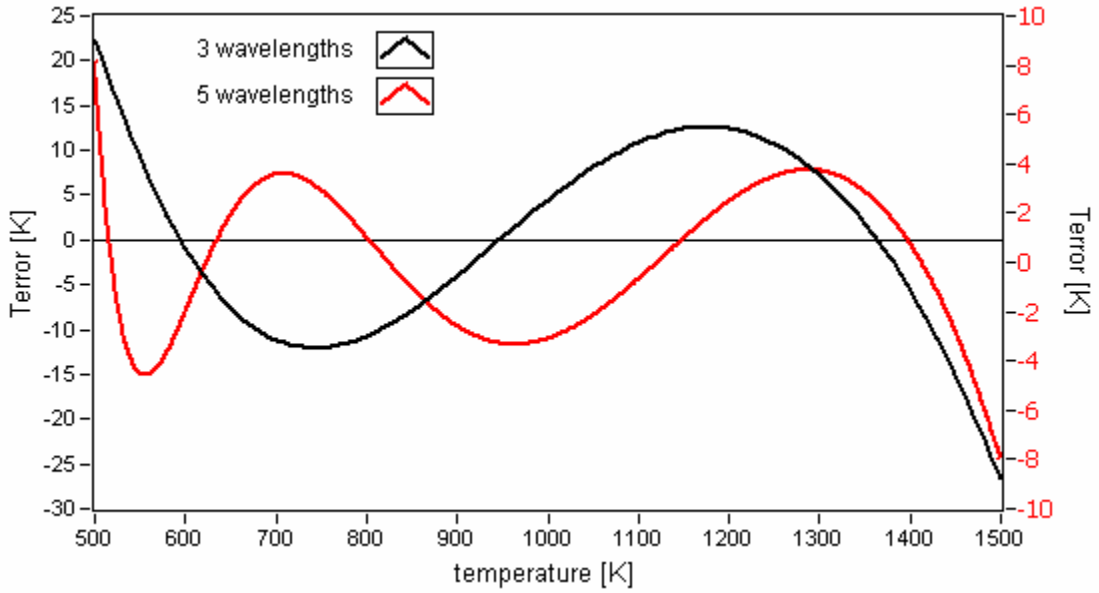

Figure 2.4 Temperature errors (Tactual – Tmeasured) when using the linear system of equations (Equation 2.10) to solve for an unknown temperature assuming a perfect measurement (zero noise). The 3 wavelength case (left axis) has 3 points where a perfect solution occurs versus the 5 wavelength case (right axis) which has 5 zero crossing points. Both of these results used a 101 point temperature vector.

If enough temperatures and wavelengths are used, it is possible to make these errors quite small and perhaps smaller than a particular design criterion of the sensor. However, even though this method is suitable for pure temperature measurements it lacks the robustness for making simultaneous temperature, concentration, and pressure measurements.

2.4.2 Spectral fitting

Another possible technique involves fitting the measured spectrum to a simulated spectrum by minimizing the sum of the squared errors (SSE) between the two. In practice, the easiest way to accomplish this task is to build a database of simulated spectra spanning a temperature range that extends past the predicted temperatures encountered in the experiment. The database method is especially useful for cases involving lots of wavelengths

(e.g. broad spanning high pressure spectra or low pressure spectra requiring high resolution). For these cases, the time penalty occurred in computing spectra on-the-fly usually warrants the database procedure.

If the concentration or mole fraction of the absorber is unknown, simply minimizing the SSE as a function of temperature may bias the results if the concentration was maintained constant in building the database and no other normalization of the data is performed. One way to alleviate this and to simultaneously solve for the concentration and temperature is to perform a linear fit between the simulated and measured spectra [28]. The figure-of-merit for this procedure then becomes the mean-squared-error (MSE) between the best fit line and the simulated data. As the temperature is varied, the measurement matches a simulated spectrum when the MSE is minimized. Concurrently, the concentration is inferred by scaling the known value used in the simulations by the slope of the best fit line.

For simplicity, assume the pressure (spectral line widths) is known therefore requiring a 2D database (temperature in the vertical direction and wavelength in the horizontal). The process of inferring the temperature would then be to loop through the N spectra and compute the MSE versus temperature and this process is depicted in Figure 2.5. The best fit temperature is then the minimum of this curve. However, because of the discrete temperatures used in the database, the temperature resolution in picking the minimum will be limited by the resolution of the database. Adding more temperatures to the database will improve this resolution at the expense of computation time. However, using a curve fit near the minimum of the MSE versus T curve and through either interpolation or a derivative of the polynomial fit to find the minimum, the resolution can be greatly enhanced.

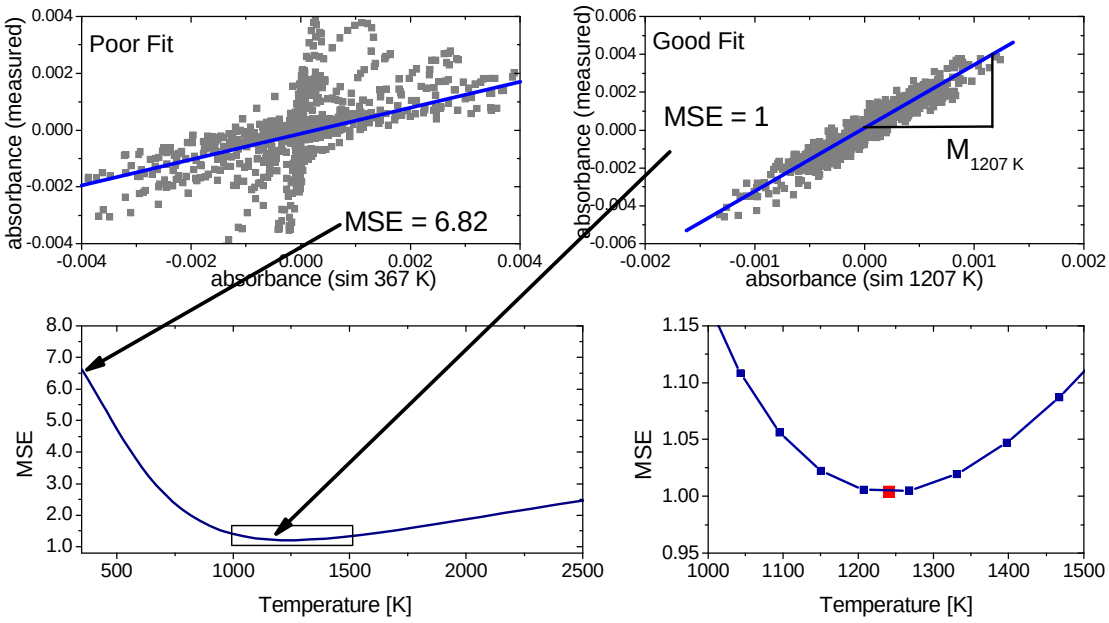

Figure 2.5 TOP LEFT: Plotting the measured spectrum at an unknown temperature versus a simulated spectrum at 367 K showing an example of a poor fit. TOP RIGHT: This fit between the measured and simulated spectrum at 1207 K is much better as indicated by the MSE of the fit. BOTTOM LEFT: The arrows point to the MSE values found in the fits in the top two graphs. The fit at 1207 K is shown to be near the minimum of the MSE versus temperature curve indicating a much better fit. BOTTOM RIGHT: The final best fit temperature is found by applying a polynomial curve fit near the bottom of the MSE versus temperature curve.

It is worth mentioning that an optimization routine can be used in place of the brute force method of converging to the best fit spectrum in the database. For instance, the downhill simplex routine (non-gradient based unconstrained minimization technique) can be used to find the minimum MSE and will reduce the number iterations to at least N/2 depending on the guess value used and the cut-off criteria. However, it may still be worthwhile to compute the MSE at the neighboring temperatures of the minimum in order to perform the curve fit for improved temperature resolution. If the database is relatively small (coarse in

temperature) the use of an optimization routine might not have much added value in relation to the added complexity of implementation. However, a hybrid routine involving both the linear system of equations and spectral fitting using the downhill simplex minimization routine can be formed where the result from the linear system of equations is used as the initial “guess” value for the downhill simplex routine resulting in faster convergence. This hybrid method can be especially attractive when processing large experimental data sets.

CHAPTER 3. WAVELENGTH SELECTION

3.1 INTRODUCTION

Current diode laser technology has allowed novel laser designs of unprecedented speed, low noise characteristics, and wavelength flexibility to be realized. In the 1300-1500 nm range, the almost arbitrary choices of wavelengths accessible for H_2O absorption sensors for combustion applications leads to the need for better understanding of the role wavelength selection plays in the overall performance of the sensor. For instance, one recent laser that has been developed can provide N discrete (single color) time division multiplexed wavelengths [13]. These wavelengths can be placed anywhere within the emission band of current semiconductor optical amplifiers (SOA) thus allowing for unprecedented flexibility in the design of absorption sensors. Another new laser design can provide 3 distinct, essentially arbitrary wavelength scans [14]. This laser also has the flexibility in locating the center locations of the scans to anywhere within the working range of SOAs. This flexibility from the source side makes the choices of the wavelengths probed for thermometry that much more important versus previous ideas of scanning an entire rotational branch for inferring gas properties.

Previously, much work and attention was given to sensors based on 2 wavelengths using a ratiometric strategy for measuring temperature and from this offered guidelines to aid the sensor designer in choosing appropriate wavelengths for their application. Nagali et.al. mentioned that for maximum temperature sensitivity, the derivative of the ratio of two absorbances with respect to temperature, dR/dT, should be maximized over the range of temperatures under consideration [29]. Specifically, wavelength pairs were chosen to

maximize the ratio of relative changes in R and T or (dR/R)/(dT/T). As an add-on requirement, they also mention that R should lie in the interval (0.25, 4) to assure similar absorption at both wavelengths but this range was specified arbitrarily.

More recently, Zhou published expanded recipes for guiding decisions on wavelength selection for situations where one or two (narrowly) tunable diode lasers are used [19,30]. Both recipes were based on a ratiometric approach to thermometry with one approach applicable to the case of a single laser and the other considering the case of using two narrowly tunable lasers. The combinations of these findings are outlined below.

1. Sufficient absorption required for high signal-to-noise ratio measurements (SNR > 10 desired although this number is somewhat arbitrary)
2. Transitions are selected to minimize interference from ambient H2O
    a. This is mainly for combustion applications where the temperature is much greater than the ambient
3. The wavelengths of both absorption lines must lie within a single laser scan and not overlap significantly (not applicable to the 2 laser case)
4. The line pair must represent sufficiently different lower state energies, E”, to yield a peak height ratio that is sensitive to temperature over the range of consideration
5. The two lines must be isolated from nearby transitions
    a. Unless the lower state energies of the overlapping transitions are similar in lower state energy thus adding constructively and increasing the SNR without loss of temperature sensitivity

6. The wavelength must be in the 1.25-1.65 µm range (specific to the lasers considered in this work)

In conjunction with these guidelines, criterion can be set specific to the absorber considered, technique employed, and limits of the equipment used. For instance, in step 1, usually the required absorption can be set by estimating the noise of the experiment and requiring the absorbance to be at least 10 times this leading to a minimum SNR of 10. It can also be advantageous to set a maximum absorbance in order to prevent the near-complete extinction of the probe beam depending on the path length of the beam through the sample gas.

These guidelines form a logical framework for 2 color thermometry but most likely are too restrictive for the case of N wavelengths. Also, they are based on the idea that the temperature will be inferred by fitting the measurements to fundamental spectroscopic parameters and this leads to difficulties such as defining the line strength or lower state energy for the case of blended spectra. For the case of measurements spanning broad wavelength ranges at high pressure where significant overlap and blending of features is prominent, more direction is needed in guiding decisions on wavelength selection for H2O thermometry.

3.2 SETUP

Of primary concern to the sensor designer is the accuracy and precision of the diagnostic. H_2O absorption based sensors for combustion applications usually are limited to the accuracy of the underlying spectral parameters used to simulate the spectrum. Steps can be taken to verify and validate these parameters such as measuring spectra under carefully controlled or highly known conditions and these experiments have and will continue to be performed

[18,19,31-34]. Often, though, the difficulty lies in building a test article capable of achieving the extremes in temperature and pressure encountered in practical combustors such as IC engines. In addition, even if these thermodynamic states are reached, there may not be a concomitant technique available for comparison to the optical absorption technique. For example, thermocouples are often limited by the maximum material temperatures and even high temperature variants of thermocouples may have large uncertainties at high temperatures due to uncertainty in the heat transfer correction.

On the other hand, the temperature precision can be optimized through smart design. As discussed previously, wavelength selection plays an important role in maximizing the sensitivity of the H_2O absorption sensor to temperature and it is not entirely obvious how to effectively choose wavelengths to guarantee optimal performance for all temperatures encountered.

To start, a highly simplified model of an ideal diatomic molecule (IDM) was constructed in order to provide a mathematically simple spectrum. By studying this model certain trends can be identified and possibly offer guidelines when considering real molecules such as H_2O.

3.3 IDEAL DIATOMIC MOLECULE (IDM) MODEL

The simplified model of the ideal diatomic can be specified as a Boltzmann distribution.

$$F_J = \frac{N_J}{N} = \frac{g_J e^{-\frac{E_J}{k_B T}}}{Q(T)} = \frac{(2J+1)\cdot e^{-\frac{BJ(J+1)}{k_B T}}}{\frac{B}{k_B T}} \tag{3.1}$$

This function specifies the fraction of the number of molecules in the J_{th} state (N_J) to the total number of molecules (N) where g_J is the degeneracy, E_J the energy of the J_{th} state, k_B is Boltzmann's constant, and Q(T) is the partition function at temperature T. In order to compare the results of studying this model to the actual H_2O spectrum, correspondence between wavelength and absorbance is needed. To do this, the rotational constant, B, is chosen to be very small such that the ratio B/k_B (often termed the characteristic rotational temperature Θ) is 0.01. This essentially makes the distribution continuous in J and is analogous to the H_2O absorption spectrum at elevated pressure where much blending of spectral lines occurs and ensures that many different Js (wavelengths) have significant population over the temperature ranges encountered in most practical combustion applications. For comparison of this model function with the H_2O spectrum, J will be considered to represent the optical frequency (wavelength) and the fractional population will be considered to represent absorption. This model contains a further simplification from the real diatomic spectrum in that all the transition probabilities are considered to be equal.

An example of this function plotted for two different temperatures can be seen in Figure 3.1. The effect of temperature is easily visible in this figure with more J states becoming populated with increasing temperature (i.e. increasing population in higher energy states). This is similar to the effect of increasing temperature in the H_2O spectrum with more wavelengths away from band center (in rovibrational spectroscopy) gaining absorption strength with temperature.

The aim of studying this simple diatomic model is to gain some insight into how to most effectively choose wavelengths when performing H_2O absorption thermometry. Of particular

concern is developing a strategy for choosing wavelengths to optimize the temperature precision when experimental noise is considered.

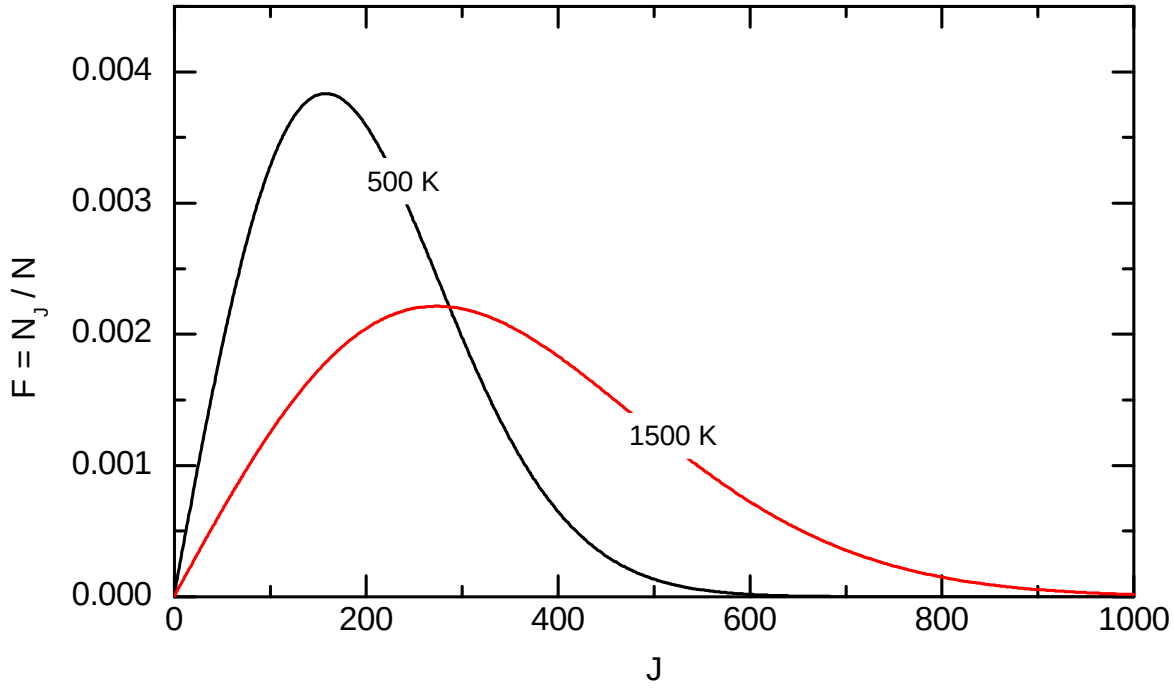

Figure 3.1 Two simulated "absorption" curves of the ideal diatomic model at temperatures of 500 and 1500 K. The absorption spectrum is simulated by using the fractional population in each energy level or "J state" and assuming the total number density, N, is constant at all temperatures. The effect of temperature is readily seen as an overall decrease in the peak absorbance value but a larger range of wavelengths having appreciable absorption.

3.3.1 Case 1: 2 wavelengths, known temperature

For the problem of choosing wavelengths, it is important to maximize the sensitivity dR/dT of the chosen line pair but a discussion of the influence of experimental noise on the measurement must also be included in the analysis.

For the ratio measurement of two absorbances, the ratio R can be defined as:

$$R \equiv \frac{\alpha_1}{\alpha_2} \qquad R \geq 1 \tag{3.2}$$

The uncertainty in R can be found by:

$$\Delta R^2 = \left(\frac{\partial R}{\partial \alpha_1} \Delta \alpha_1 \right)^2 + \left(\frac{\partial R}{\partial \alpha_2} \Delta \alpha_2 \right)^2 \tag{3.3}$$

This after some manipulation yields the relative uncertainty as:

$$\frac{\Delta R}{R} = \sqrt{\frac{\Delta \alpha_1^{\,2}}{\alpha_1} + \frac{\Delta \alpha_2^{\,2}}{\alpha_2}} \tag{3.4}$$

If the calibration function R(T) is known, then the uncertainty in temperature can be defined as:

$$\Delta T_{ratio} = \frac{\partial T}{\partial R} \Delta R = \frac{R}{\frac{\partial R}{\partial T}} \sqrt{\frac{\Delta \alpha_1^{\,2}}{\alpha_1} + \frac{\Delta \alpha_2^{\,2}}{\alpha_2}} \tag{3.5}$$

After some manipulation, this relation can be recast into the following form.

$$\Delta T_{ratio} = \frac{\sqrt{R^2 + \left(\frac{\Delta \alpha_1}{\Delta \alpha_2} \right)^2}}{\frac{\partial R}{\partial T} \left(\frac{\alpha_2}{\Delta \alpha_2} \right)} \tag{3.6}$$

This relation shows the precision in temperature not only depends on the sensitivity of the chosen line pair (dR/dT) but also the ratio of the absorbances and the SNR of the weaker of the two lines.

For the IDM, the ratio is the following function.

$$R(J_1, J_2, T) = \frac{2J_1 + 1}{2J_2 + 1} \cdot e^{\Theta(J_1 + J_2 + 1) \cdot \frac{J_2 - J_1}{T}} \tag{3.7}$$

Similarly, the derivative of the ratio R with respect to T can be found.

$$\frac{\partial R(J_1, J_2, T)}{\partial T} = -\frac{2J_1 + 1}{2J_2 + 1} \cdot \Theta \cdot (J_1 + J_2 + 1) \cdot \frac{J_2 - J_1}{T^2} \cdot e^{\frac{\Theta \cdot (J_1 + J_2 + 1)(J_2 - J_1)}{T}} \tag{3.8}$$

The aim is to find the best pair of Js that will minimize the function in equation 3.6. For this relatively simple case of 2 wavelengths at a known temperature, the analytic solution would prove to be quite cumbersome. Even in doing so, moving to the more interesting but difficult case of 2 wavelengths over an unknown temperature range this analytic solution would not provide any more insight. The other alternative is to find the best pair of wavelengths numerically through an optimization routine. This has the benefit of being relevant for all possible cases posed for the IDM and will also prove to be highly effective for the more practical problem of optimizing H_2O wavelength selection.

The function in equation 3.6 can be minimized rather easily using any of the standard non-linear optimization routines presented in most modern scientific computing packages (e.g. conjugate-gradient, quasi-Newton, Levenberg-Marquardt). However, in order to solve the more difficult problem of choosing wavelengths when considering a range of temperatures, a more robust algorithm is needed in order to overcome the possibilities of many local minima. Genetic algorithms offer the benefit of searching over large domains and are particularly well suited to optimizing stochastic functions.

For this work the differential evolution (DE) algorithm was used to minimize all objective functions proposed for finding optimum wavelengths for thermometry. DE finds the global

minimum of a multidimensional, multimodal (i.e. exhibiting more than one minimum) function with good probability. The crucial idea is a scheme for generating trial parameter vectors. DE adds the weighted difference between two population vectors to a third vector. This way no separate probability distribution has to be used making the algorithm completely self organizing. For more information about DE the interested reader is refered to the following sources [35-38].

To find the best 2 wavelengths for optimizing the precision of temperature measurements for the simple case of a single known temperature, the function in equation 3.6 is used as the objective function with the added constraint that J must lie in the domain (0,1000). To implement this inequality constraint, the objective function is modified by adding an additional case statement that checks the parameters chosen by the DE algorithm and applies a penalty if the constraint is not satisfied. Also, the noise terms are assumed to be fixed and the same for all wavelengths. This assumption is based on the fact that the minimum detectable absorbance (MDA) will be approximately constant across the spectrum.

The best wavelength pairs at 5 different temperatures are shown in Figure 3.2. The visible trend is the best wavelength pairs (represented as the vertical drop lines) moving to higher energy levels with increasing temperature. From this figure, it is not obvious as to why the particular wavelengths chosen are better than other choices but comparing the wavelengths from the DE to those obtained with a conjugate-gradient method give the same results. The conjugate-gradient method works well for this simple case since the objective function is smooth and exhibits a single global minimum.

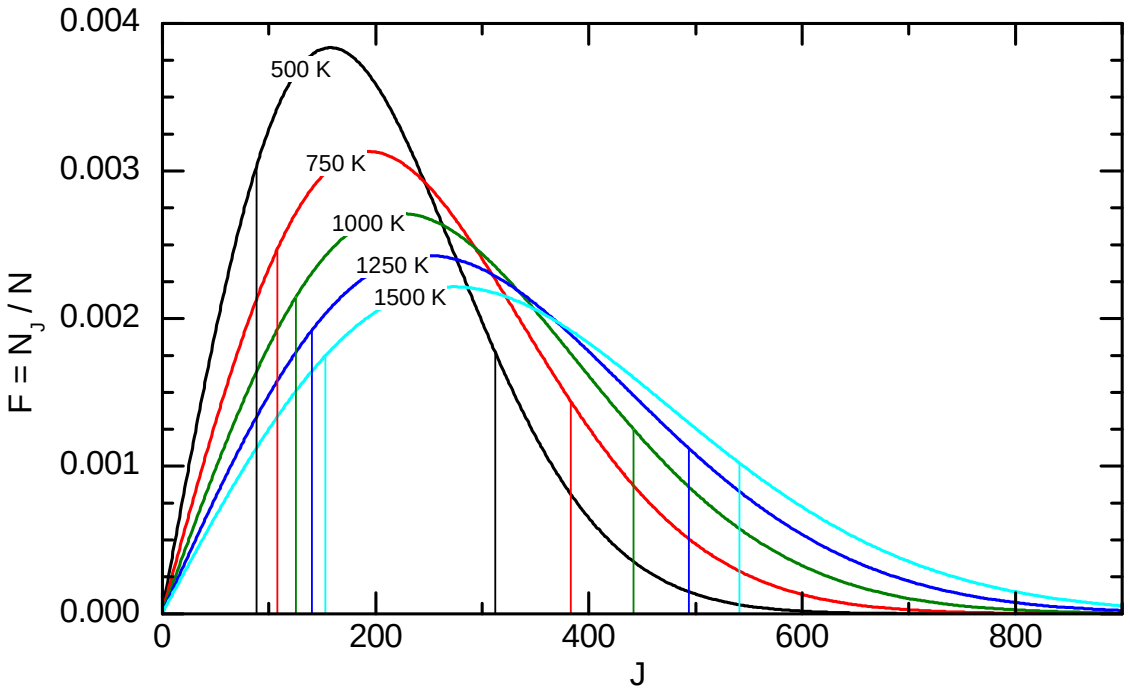

Figure 3.2 Showing the best two Js (wavelengths) that will maximize the precision of the temperature measurement for the prescribed temperature. The visible trend is the wavelengths of the best pair moving to higher energy levels with increasing temperature.

Once the best wavelength pairs at a specific temperature have been found, it is possible to calculate the performance over a range of temperatures. Figure 3.3 shows the performance curves for the wavelengths chosen at a single, specified temperature over a range of temperatures. It is easily seen that the performance is optimized at the temperature for which the wavelengths were chosen. It is also interesting to note that the performance is always a little better for a specific line pair at temperatures slightly lower than those used for the optimization. This is attributed to the SNR improving for the slightly cooler temperatures without sacrificing sensitivity (i.e. $d(dR/dT)/dT < d(SNR)/dT$ over a small dT).

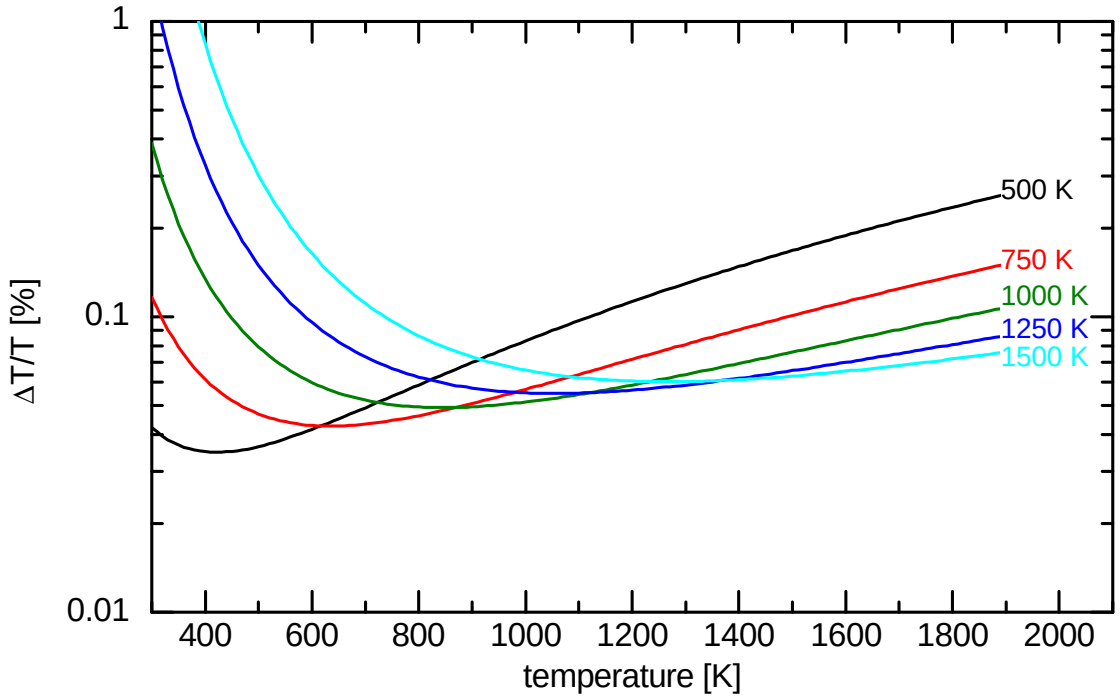

Figure 3.3 Temperature precision performance of the best line pairs chosen for a specific temperature using a fixed noise level of 1E-6. The curves show that the performance is optimized at the temperature considered for a particular line pair. What is also evident is the performance of a particular line pair is always a little better at slightly colder temperatures than the temperature used for optimizing.

It is possible to reformulate the objective function into a form that allows a better way of graphically depicting the choice for the best 2 wavelengths at a particular temperature. To do this, the derivative, dR/dT, can be rewritten in terms of absorbance.

$$\frac{dR}{dT} = \frac{\alpha_1'}{\alpha_2'} - \frac{\alpha_1 \alpha_2'}{\alpha_2^2} \qquad \alpha' \equiv \frac{d\alpha}{dT} \tag{3.9}$$

Upon substituting this into equation 3.6 and assuming the noise terms are equal leads to the following relation.

$$\Delta T_{ratio} = \frac{\Delta\alpha\sqrt{R^2+1}}{\left|\alpha_1^{'} - R\alpha_2^{'}\right|} \tag{3.10}$$

This equation shows that minimization of ΔT requires the chosen wavelengths to have the largest difference between their derivatives with respect to temperature in order to maximize the denominator. From this, the ratio of the absorbances should also be maximized to the degree that further increase in R doesn't penalize by making the numerator too large.

To visualize this, the spectra along with the derivative spectra are shown in Figure 3.4. From the derivative spectrum picture, it is easily seen that the best choice for wavelengths at a particular temperature are those that exhibit the largest change in absorbance with a change in temperature at the temperature considered (i.e., the peaks and valleys of the derivative spectrum). The final choice of the best 2 wavelengths do not converge exactly to the peak and valley of the derivative spectrum due to the ratio of the absorbance becoming the controlling term as the ratio differs further from 1.

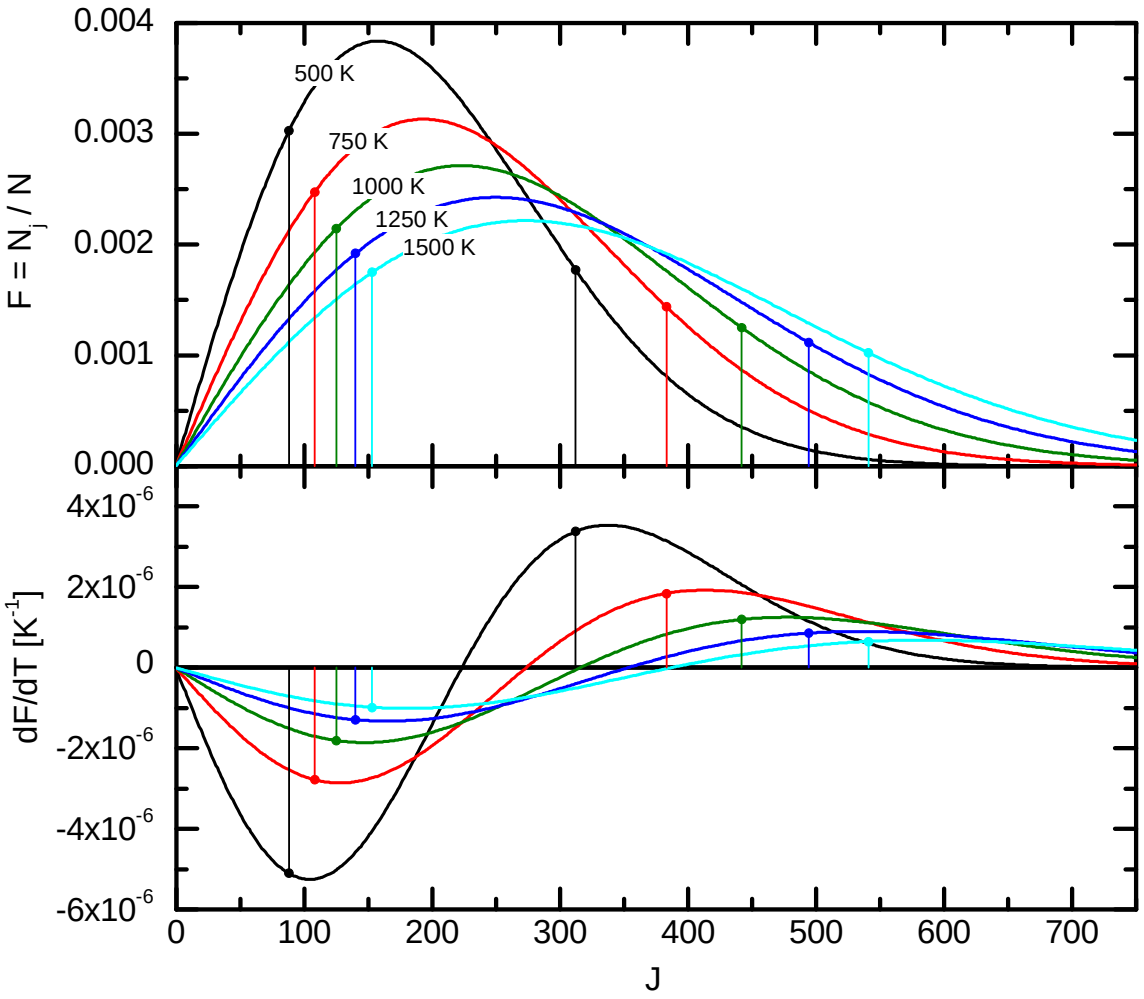

Figure 3.4 TOP PANEL: Spectra at various temperatures showing the best line pairs chosen for optimizing the temperature precision. BOTTOM PANEL: Derivative spectra showing the same chosen line pairs. The choices for the best line pairs at a specific temperature tend to fall near points where the largest change in absorbance with a change in temperature occurs.

Up to this point, the choice of the best 2 wavelengths for minimizing the uncertainty in temperature at a specific temperature has been decided by minimizing the function in equation 3.6 through the use of a non-linear optimization routine. This method works quite well and converges quickly owing to the relatively simple objective function. In addition, the

derivative of the spectrum with respect to temperature offers a way to quickly view wavelengths that will provide optimal sensitivity to temperature. However, neither of these methods lead to a direct view of how the lower state energy plays a role in wavelength selection.

Another way of viewing this problem is through the use of the ratio spectrum. For this IDM model, this leads to the following relation.

$$\frac{F(T)}{F(T_{ref})} = \frac{(2J+1)\cdot e^{-\frac{E}{k_B T}}\cdot\frac{\Theta}{T}}{(2J+1)\cdot e^{-\frac{E}{k_B T_{ref}}}\cdot\frac{\Theta}{T_{ref}}} = \frac{T_{ref}}{T}\cdot e^{E\left(\frac{1}{k_B T_{ref}}-\frac{1}{k_B T}\right)} \tag{3.11}$$

Taking the natural logarithm of this expression gives the following useful relation.

$$\ln\left(\frac{F(T)}{F(T_{ref})}\right) = \ln\left(\frac{T_{ref}}{T}\right) + E\left(\frac{1}{k_B T_{ref}} - \frac{1}{k_B T}\right) \tag{3.12}$$

From equation 3.12, one can anticipate that a graph of the natural log of the ratio spectrum versus lower state energy (E) is linear with the slope given by a simple function of temperature only.

$$slope = \frac{1}{k_B T_{ref}} - \frac{1}{k_B T} \tag{3.13}$$

This is confirmed in looking at Figure 3.5 below.

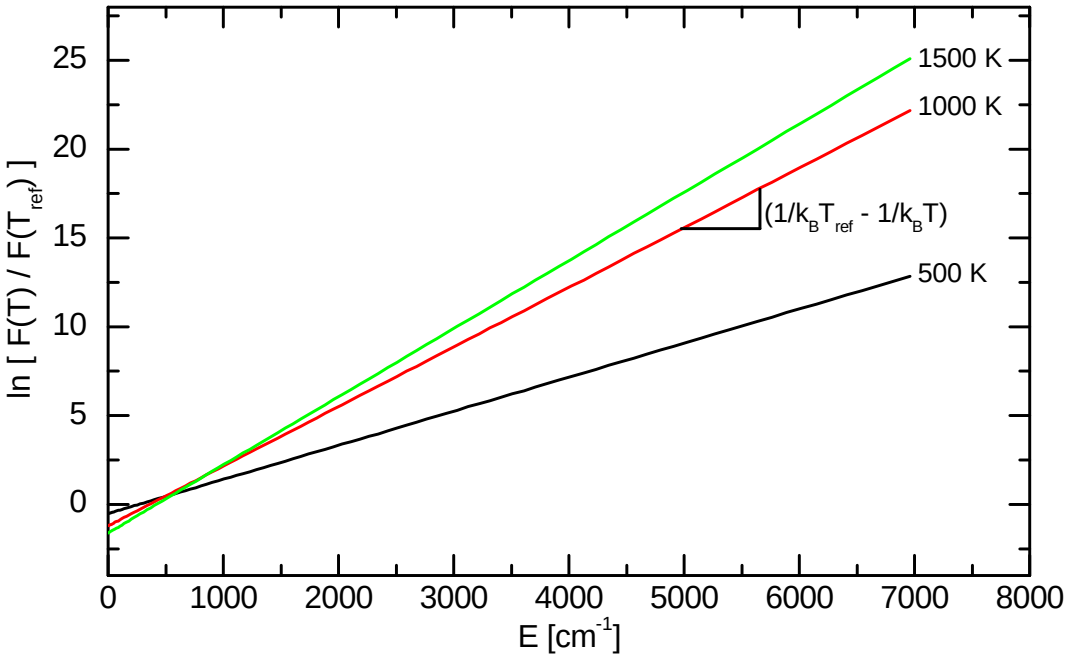

Figure 3.5 Linear relationship between the lower state energy E and the natural log of the ratio of spectra computed at T and a reference T. The slope is determined by a simple function of temperature only.

Another way then to define the uncertainty in temperature is by describing the uncertainty in measuring the slope of this linear function.

The slope for a measurement at 2 wavelengths can be defined as:

$$S = \frac{\ln(F_2(T)) - \ln(F_2(T_{ref})) - (F_1(T)) + (F_1(T_{ref}))}{E_2 - E_1} \tag{3.14}$$

The uncertainty in measuring the slope will only depend on the uncertainty in the measurement of F_1 and F_2.

$$\Delta S^2 = \left(\frac{\partial S}{\partial F_1}\Delta F_1\right)^2 + \left(\frac{\partial S}{\partial F_2}\Delta F_2\right)^2 \tag{3.15}$$

This leads to following relation for the uncertainty in S where F has been replaced by α for convenience in comparing to previous relations.

$$\Delta S = \frac{1}{|\Delta E|}\sqrt{\left(\frac{\Delta\alpha_1}{\alpha_1}\right)^2 + \left(\frac{\Delta\alpha_2}{\alpha_2}\right)^2} \quad where\, \Delta E = (E_2 - E_1) \tag{3.16}$$

From this the uncertainty in temperature can be defined as:

$$\Delta T_B = \frac{\partial T}{\partial S}\Delta S = \frac{k_B T^2}{|\Delta E|}\sqrt{\left(\frac{\Delta\alpha_1}{\alpha_1}\right)^2 + \left(\frac{\Delta\alpha_2}{\alpha_2}\right)^2} \tag{3.17}$$

The subscript B on the temperature uncertainty is there owing to the fact that this equation represents a Boltzmann limit in the uncertainty in temperature when considering experimental noise. This relation directly shows that the choice of 2 wavelengths for optimizing the uncertainty in temperature should be made by maximizing the difference in lower state energies while keeping the SNR of the two measurements at acceptable levels. Upon comparing the relation in 3.17 to the relation in 3.5 it is shown that temperature sensitivity for the ratiometric formulation is optimized for a particular line pair when

$$\frac{R}{\frac{\partial R}{\partial T}} = \frac{k_B T^2}{|\Delta E|} \tag{3.18}$$

This is exactly the same relation derived in equation 2.9 and it shows that the temperature sensitivity of a specific line pair provides a good starting point for choosing wavelengths when optimizing 2 color thermometry at a single temperature.

3.3.2 Case 2: 2 wavelengths, unknown temperature

The previous case of choosing 2 wavelengths at single, known temperature provided a good starting point for developing strategies for choosing wavelengths for more interesting and practical cases. For instance, the next logical progression would be deciding the best 2 wavelengths for optimizing thermometry at an unknown temperature within some expected range of temperatures to be encountered in an experiment.

In order to do this, the objective function for the single temperature case will have to be slightly modified to include the range of possible temperatures. Instead of directly minimizing the relation in equation 3.5, a possible new objective function to be minimized is the sum of the relative uncertainties over a specified range of temperatures.

$$\sum_{T} \frac{\Delta T_{ratio}}{T} = \sum_{T} \frac{R}{T \frac{\partial R}{\partial T}} \sqrt{\frac{\Delta \alpha_1^{\,2}}{\alpha_1} + \frac{\Delta \alpha_2^{\,2}}{\alpha_2}} \tag{3.19}$$

An example of the performance results obtained after minimization of this objective function is shown below in Figure 3.6. Also shown in this figure are the results from the single temperature case. It is interesting to note that the relative uncertainty for the line pair chosen over the temperature range (500-1500 K) performs similarly to the results for the single temperature case at the geometric mean of the temperature range considered.

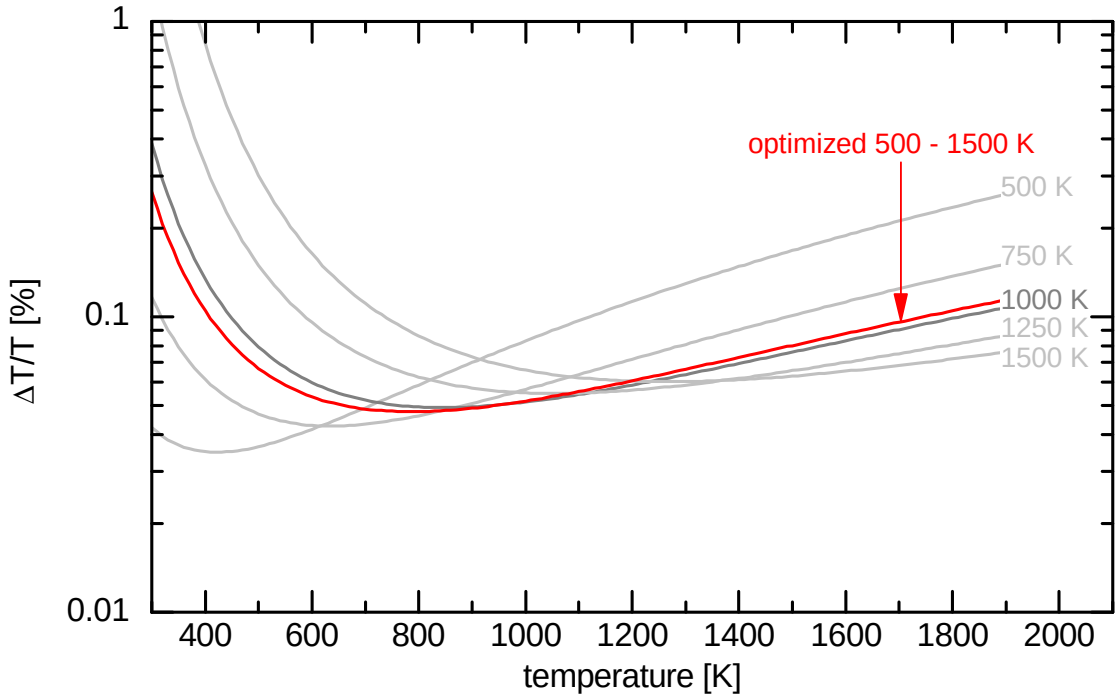

Figure 3.6 Relative uncertainty in temperature versus temperature for the 2 wavelength case. The result for the best line pair when considering the range of temperatures (500-1500 K) is shown along with the results obtained when considering a single temperature.

However, the actual wavelengths chosen for the temperature range case do not correspond to any choices found for a single temperature case. Put differently, the best two wavelengths found when optimizing the temperature precision over a range of temperatures cannot be found by optimizing the precision at one specific temperature. When considering a range of temperatures, it is best to choose the wavelengths based on the performance over this range. However, this effect becomes less pronounced as the temperature range considered is reduced. On the other hand, the difference in the wavelengths chosen for the wide range (500-1500 K) are not too different from the wavelengths chosen at 1000 K. This could

provide a method for quickly identifying possible candidates without having to consider the entire range.

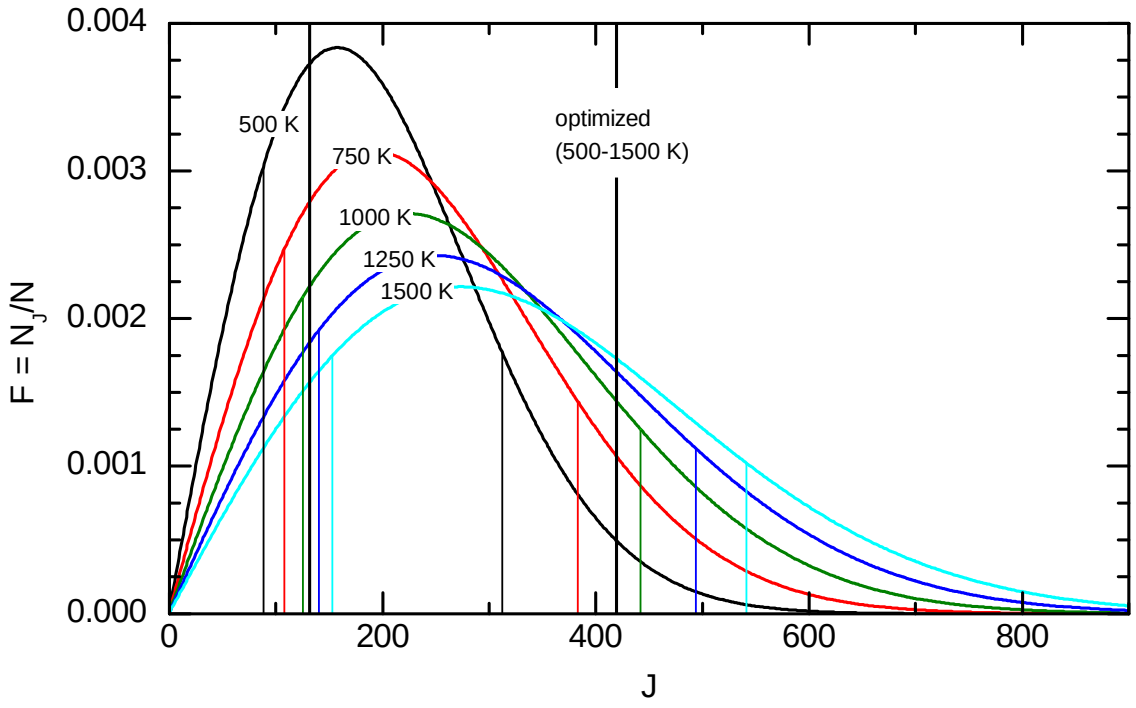

Figure 3.7 The line pair chosen to optimize the relative uncertainty over a range of temperatures is plotted along with the line pairs chosen for the single temperature cases. The choice of the best line pair does not correspond to the best pair at any single temperature.

The two cases considered up to this point have only provided a method for choosing two separate wavelengths for making temperature measurements. In practice, this amounts to using two fixed wavelength lasers aligned to the features of interest or using one laser capable of outputting two separate wavelengths multiplexed in time. However, using tunable lasers capable of covering a range of wavelengths it is possible to measure the spectrum at more than two discrete points. This is also true for a single laser capable of outputting N discrete wavelengths. It is therefore desirable to have a method of choosing wavelengths

when considering the N wavelength case and even more so, having a means to directly quantify the results in order to compare the 2 wavelength case to the N wavelength case.

3.3.3 Case 3: N wavelengths, known temperature

In order to solve the N wavelength selection problem, a new objective function needs to be specified that is capable of including the measurements at N wavelengths. The two color ratiometric technique of the previous sections does not have an obvious means of extending the analysis to N wavelengths. From previous work dealing with multiple color absorption measurements, the temperature is inferred through a spectral fitting routine similar to what was outline in section 2.4.2. One possible formulation of an objective function for N wavelengths is to repeatedly compute the temperature of a N wavelength spectrum with added Gaussian white noise and from which the standard deviation in the computed temperatures can be obtained. This type of an objective function is very close to what would be realized in an actual experiment.

In order to estimate the number of iterations needed to estimate the variance of the temperature results within 10% of the true value with 95% confidence the following relation is used based on the Student t test [39].

$$P\left\{\left|(\hat{\sigma})^2-\sigma^2\right| \le 1.96\sigma^2\sqrt{2/k}\right\}=0.95 \tag{3.20}$$

The requirement of at most 10% error in the variance estimate gives the following:

$$\frac{\left|(\hat{\sigma})^2-\sigma^2\right|}{\sigma^2}=0.1 \tag{3.21}$$

Which leads to setting:

$$1.96\sqrt{2/k} = 0.1$$
$$k \approx 800 \tag{3.22}$$

Therefore, the number of iterations needed to accurately estimate the standard deviation in temperature is approximately 800. The procedure then for finding the best wavelengths for the N wavelength case at a known temperature using the iterative least square fitting (iLS) objective function is then:

1. Compute the “measured” absorbance for N wavelengths at temperature T and a database N wavelengths at M temperatures surrounding T
2. Add a prescribed amount of Gaussian white noise to the computed spectrum
3. Find the best fit temperature of the measured spectrum by least square fitting to the database of spectra
4. Repeat k times and calculate the standard deviation of the inferred temperatures

Therefore, for each population generation of the DE optimization routine, roughly M*k calculations are needed for one calculation of the objective function. The results of optimizing this objective function for the single temperature case of 500 K for 2,3,4, and 10 wavelengths are shown below in Figure 3.8 and Figure 3.9.

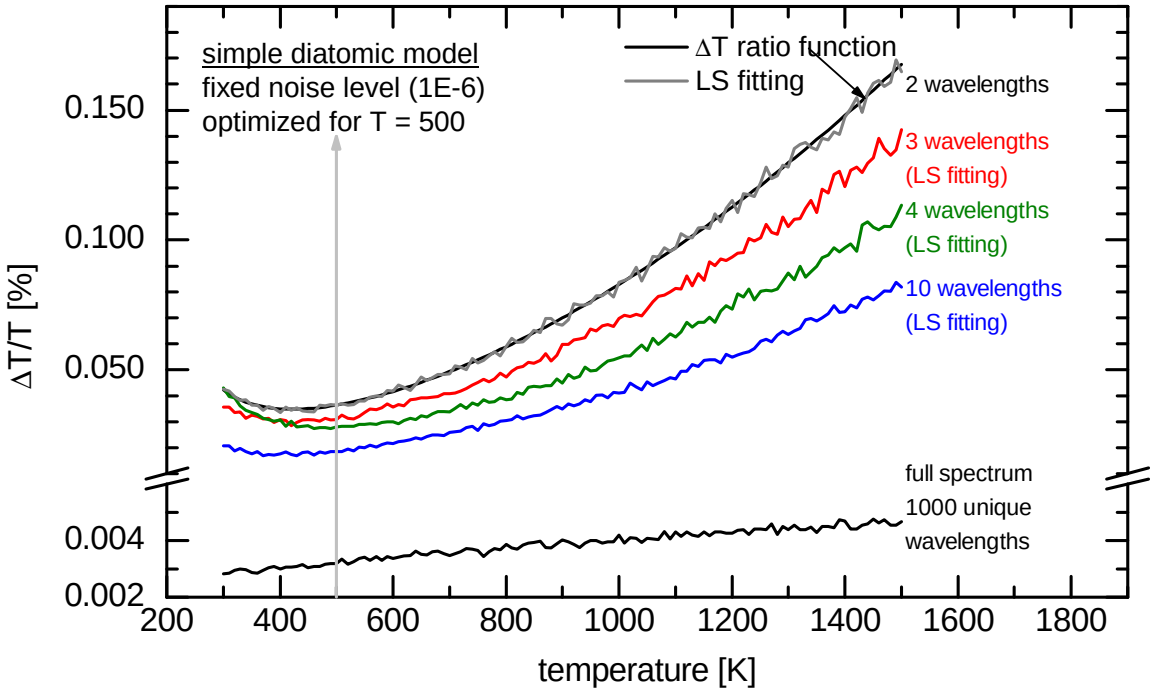

Figure 3.8 Relative uncertainty performance results for the N wavelength case when optimizing at a single temperature (500 K). The 2 wavelength case is also shown with the results obtained both through fitting and through the ratio function derived earlier and good agreement is found between the two. At fixed performance (i.e. same noise level assumed for all number of wavelengths) adding wavelengths improves the fidelity of the measurement.

For fixed noise level for all wavelength count cases considered, the general trend of adding wavelengths is to improve the fidelity of the measurement. As a check, it was verified that the ΔT_{ratio} function used in the 2 wavelength case and spectral fitting gave the same results when considering the two wavelength case.

In looking at the actual wavelengths chosen in Figure 3.9, the visible trend is the additional wavelengths should be located near the optimum pair selected in the 2 wavelength case. This makes sense for the single, known temperature case in that these two points on the spectrum

offer the best sensitivity to temperature. The only other logical choices would be closer to the peak for perhaps increased SNR but in looking at the derivative spectrum this would cause those choices to have less sensitivity with temperature and as was shown earlier, the differences in the lower state energy would be decreased again leading to less sensitivity in temperature.

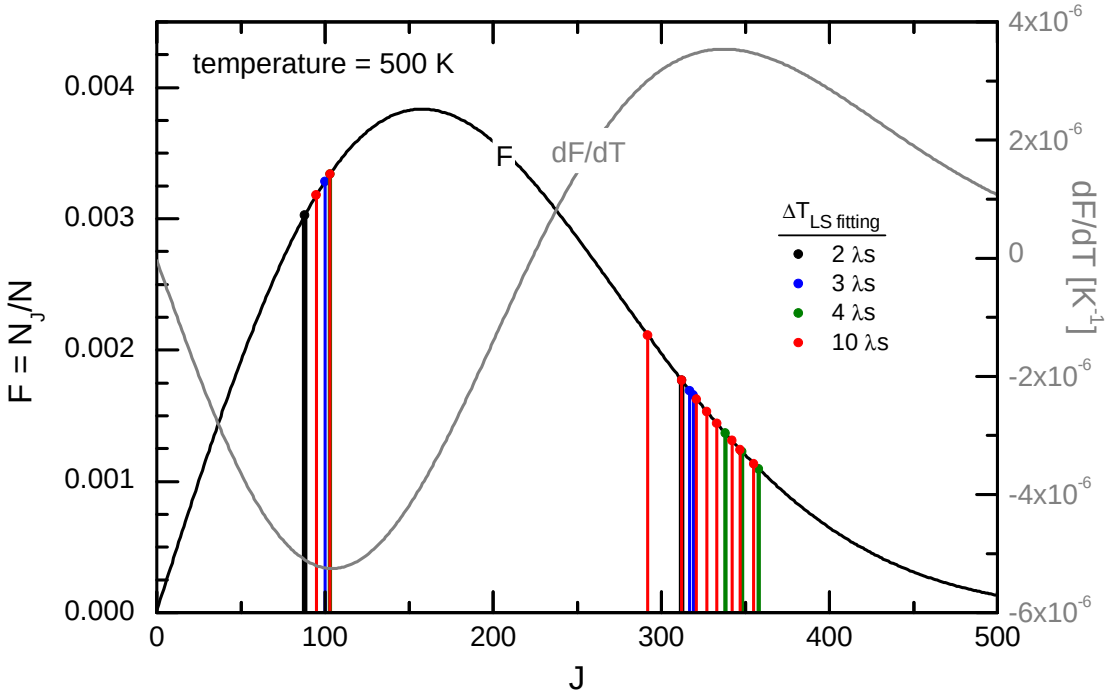

Figure 3.9 Final wavelength choices when optimizing 2,3,4 and 10 wavelengths at 500 K. For the IDM model, adding more wavelengths tends to putting more wavelengths near the choices found in the 2 wavelength case. The wavelengths found in the 2 wavelength are the critical wavelengths.

It is unclear if the wavelengths selected through this objective function are actually the best choices. The choice of optimizing an objective function that was based on estimating the variance to within 10% leads to an unclear estimate of the global optimum. Also, the method of estimating the variance through iteration is costly in computation time (M*k computations

for this N wavelength objective function versus one computation for the 2 wavelength case). Therefore a better objective function is desired.

Building on the idea presented in deriving the Boltzmann limit for temperature uncertainty for the two wavelength case given in section 3.3.1, a new expression for the temperature precision for N wavelengths can be developed. As it was shown, the uncertainty in temperature can be derived by estimating the uncertainty in measuring the slope of the graph of $\ln(\alpha / \alpha_{ref})$ versus E" (see Figure 3.5). To extend this analysis from 2 to N wavelengths, the slope can be calculated using least squares regression. It should be stated that the idea of using the Boltzmann plot ($\ln(\alpha / \alpha_{ref})$ vs. E") is not new. References of this idea can be traced back to at least Herzberg in his book on the spectra of diatomic molecules [40].

The least square solution can be found by minimizing the sum of the square of the residuals between the measured points and the best fit line.

$$R^2 = \sum_i \left[\ln(\alpha / \alpha_{ref})_i - (b + sE_i) \right]^2 \tag{3.23}$$

Taking the partial derivative of this equation with respect to m and s leads to the following equations that can be used to find the best m and s that will minimize R^2.

$$\begin{aligned} \frac{\partial R^2}{\partial b} &= -2\sum_i (\ln(\alpha / \alpha_{ref})_i - b - sE_i) = 0 \\ \frac{\partial R^2}{\partial m} &= -2\sum_i (\ln(\alpha / \alpha_{ref})_i - b - sE_i)E_i = 0 \end{aligned} \tag{3.24}$$

Upon solving these two equations for m and s leads to the following relation for the slope s.

$$s = \frac{\overline{E}\,\overline{\ln(\alpha/\alpha_{ref})} - N\,\overline{E\ln(\alpha/\alpha_{ref})}}{\overline{E}^2 - N\,\overline{E^2}} \qquad where\ \bar{x} = \sum_i^N x_i \tag{3.25}$$

The variance in measuring the slope can be defined as:

$$\Delta s^2 = \sum_i \left(\frac{\partial s}{\partial \alpha_i} \Delta \alpha_i \right)^2 \tag{3.26}$$

with the partial derivatives given by:

$$\frac{\partial s}{\partial \alpha_i} = \frac{1}{\alpha_i} \left(\frac{\overline{E} - NE_i}{\overline{E}^2 - N\overline{E^2}} \right) \tag{3.27}$$

Finally, the unweighted least squares (uwLS) uncertainty in temperature can be given by:

$$\Delta T_{uwLS} = \frac{\partial T}{\partial s} \Delta s = \frac{k_B T^2}{\left| \overline{E}^2 - N\overline{E^2} \right|} \sqrt{\sum_i \left(\frac{\Delta \alpha_i}{\alpha_i} \right)^2 \left(\overline{E} - NE_i \right)^2} \tag{3.28}$$

The absolute value in the denominator of this expression is there as a reminder that this term was factored out of the square root.

In comparing this expression to the 2 color Boltzmann expression given in equation 3.17 a few key similarities are evident. For one, the $k_B T^2$ term is still present and in fact is a factor that will always be present for a system that follows Boltzmann statistics. Also, when 2 wavelengths are considered, this expression becomes identically equal to the expression in equation 3.17 therefore making this relation a more general expression to use when selecting any number of wavelengths.

The usefulness of this expression becomes more evident when used as the objective function for selecting the best wavelengths. Instead of the M*k calculations needed for one evaluation of the least square fitting objective function used above, a single calculation can be performed to give the value of the objective function for a single set of parameters in the DE genetic algorithm.

Aydin et.al. used a similar idea in measuring electron temperatures in laser induced plasmas [41]. In this work, they first systematically identified a collection of isolated spectral emission lines when considering the FE I and FE II electronic bands. Upon making a set of measurements, spectral lines with the highest average deviations from the Boltzmann plot regression function are slowly discarded until a threshold value for the coefficient of determination is exceeded. This is essentially a wavelength selection procedure *Ex Post Facto*. The novelty of the proposed method in this work is using the Boltzmann plot idea for selecting wavelengths up front when experimental noise is considered in order to optimize the thermometry results.

The previous example of finding the best wavelengths at a known, single temperature was repeated with the new ΔT_{uwLS} objective function. These results can be seen below in Figures Figure 3.10 and Figure 3.11. The performance curves for the two methods are identical for the 2 wavelength case in that both methods chose the same 2 colors found using the ΔT_{ratio} function earlier. However, for 3 wavelengths and more, the performance of the ΔT_{uwLS} is better. This is attributed to the fact that the uwLS function only gave 2 unique colors for each number of wavelengths considered. This is due to the fact that for a known temperature, there are 2 unique wavelengths that will optimize the precision of the temperature measurement.

Repeating the measurement of one or both of the wavelengths is in essence averaging the measured values and increasing the SNR of the 2 critical wavelengths.

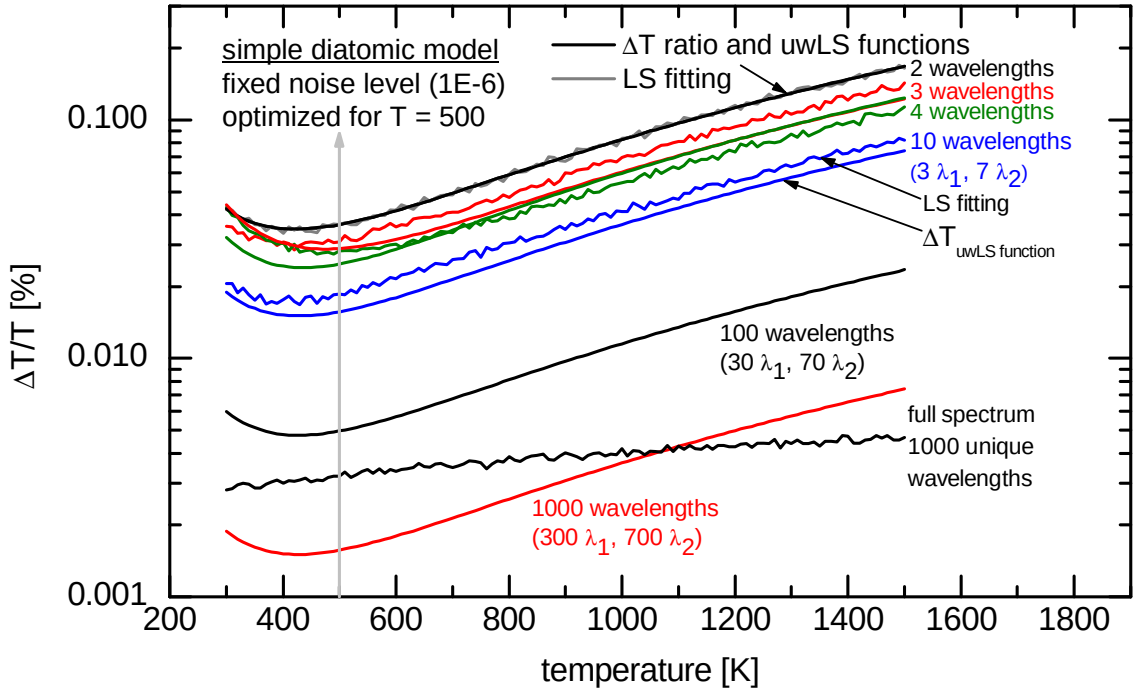

Figure 3.10 Comparison of the results of the N wavelength, single temperature case using the iLS objective function and the ΔT_{uwLS} objective function. For 2 wavelengths, these two objective functions give the same results and are both equal to the results given using the ΔT_{ratio} function. However, as N is increased from 2, the two methods diverge with the ΔT_{uwLS} function leading to a selection of wavelengths with better performance.

In looking at the actual wavelengths given by the uwLS function, the trend that is visible is that as N is increased the optimal wavelengths tend to converge to the peaks on the derivative spectrum and the splitting ratio tends to a 30-70 split with 30% of the N wavelengths used for the stronger line near J of 100 and 70% of the N wavelengths located near 330.

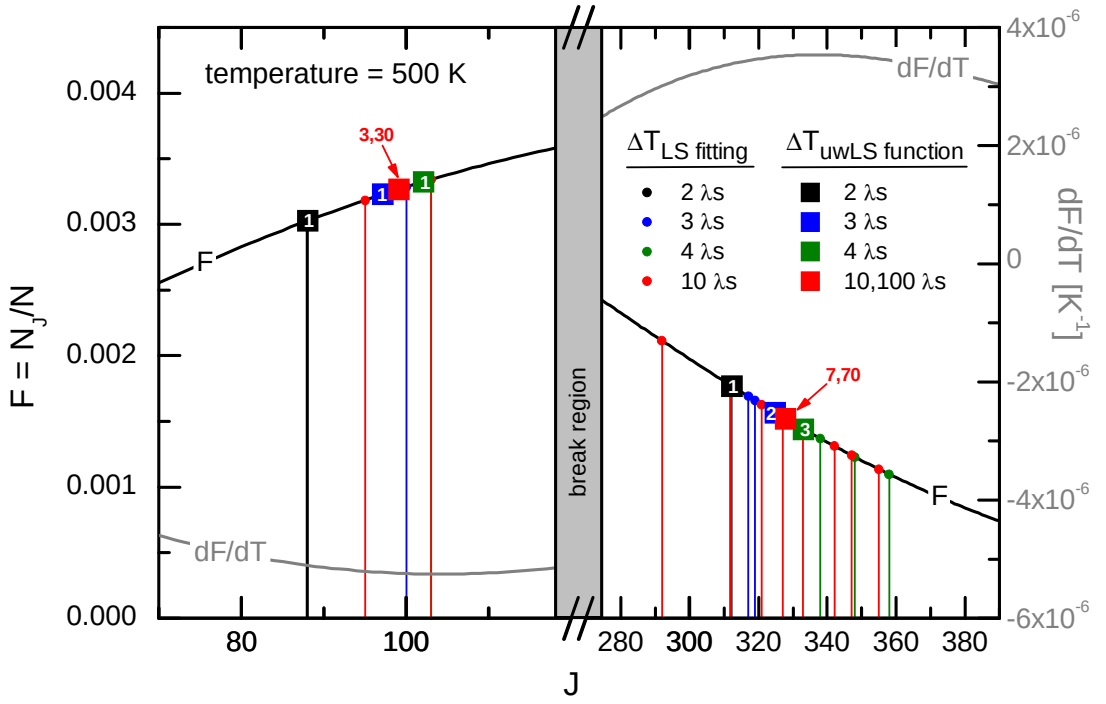

Figure 3.11 This figure shows the best wavelengths chosen using the ΔT_{uwLS} function and also shows the previous results obtained through the least squares fitting function. For each number of wavelengths considered, the ΔT_{uwLS} function gave just 2 independent wavelengths. For instance, the 3 wavelength case shown in blue squares is actually 2 unique colors (1 near 100 and 2 near 320).

This case study of N wavelengths at a known temperature has shown that there are 2 unique colors for optimizing the temperature precision and the choice of the two depends on the timing characteristics of the laser used. For instance, if 2 separate lasers are used and the splitting ratio of time spent measuring each one is 50/50; the results found when considering 2 wavelengths should be used. Otherwise, if the lasers can be timed such that 30% of the allowed measurement time is used for λ_1 and 70% for λ_2 then the results of the 10 and 100 wavelength case should be used. This, of course, assumes that the noise performance at each

of the two colors is the same and if not, then the actual noise characteristics should be included in the optimization routine.

3.3.4 Case 4: N wavelengths, unknown temperature

The previous section only considered the best wavelengths when optimizing for a single temperature. In practice, the temperature is usually unknown and depending on the device under test, may vary considerably. The more interesting case would be selecting wavelengths when considering a range of temperatures.

Before specifying the objective function to be used to find the best wavelengths over a range of temperatures, the performance of the uwLS function should be tested when using the entire spectrum (i.e. measuring at all the possible wavelengths in order to cover the entire range of lower state energies) and compared to the results obtained by directly fitting the spectrum through either least squares or minimizing the sum of the square errors (SSE).

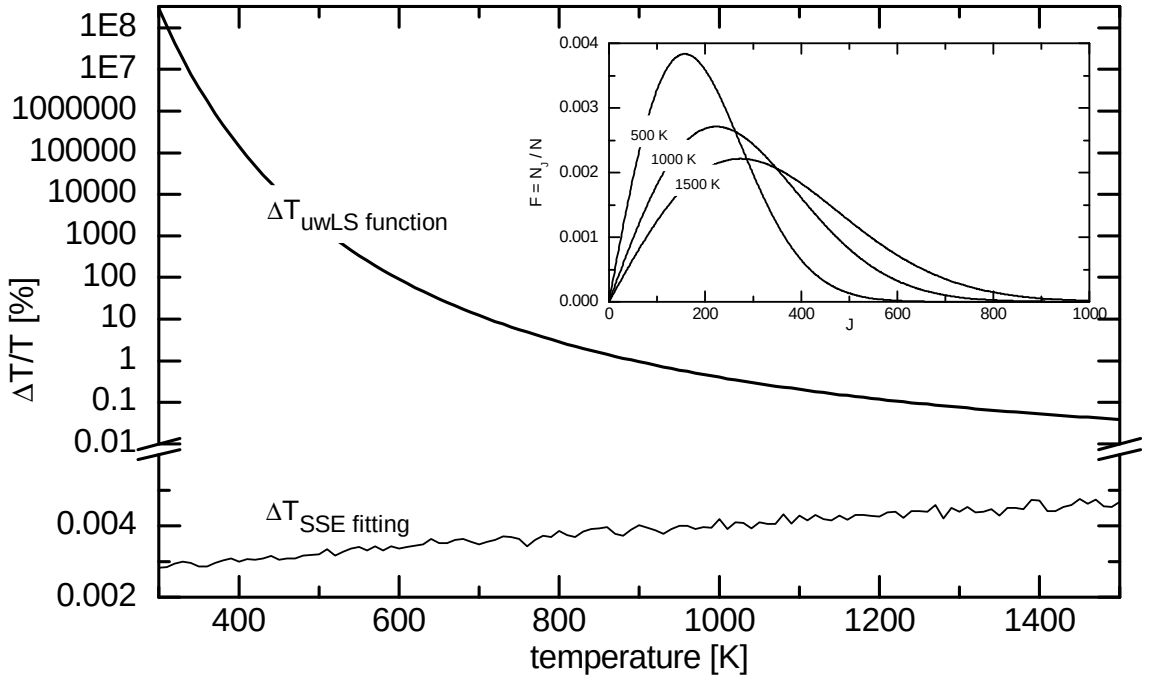

Figure 3.12 Results of the uwLS function and SSE fitting showing the large discrepancies between the two when calculating the relative uncertainty for the entire spectrum (1000 wavelengths spaced at increments of 1).

As can be seen in Figure 3.12, the ΔT_{uwLS} function blows up at low temperatures and is still quite different than the SSE fitting results at high temperatures. This is attributed to the fact that the uwLS function is unfairly biased by the large number of wavelengths exhibiting nearly zero absorbance. This is especially true at the colder temperatures where approximately 50% of the wavelengths are zero plus noise. When inferring the temperature through least squares fitting by comparing the measured spectrum to a database of spectra at different temperatures, the fitting is inherently weighted by the magnitude of the absorbance values. This is due to the fact that the zero absorbance points are all localized to a single region on the plot of the measured absorbance versus reference absorbance and so the bulk

effect is an ensemble average over these zero points thus reducing their effect on the fidelity of the fit. This effect can be seen in Figure 3.13 near the (0,0) point where the zero absorbance points all lie approximately in a vertical plane at x = 0 due to noise occurring only in the measured spectrum (y dimension).

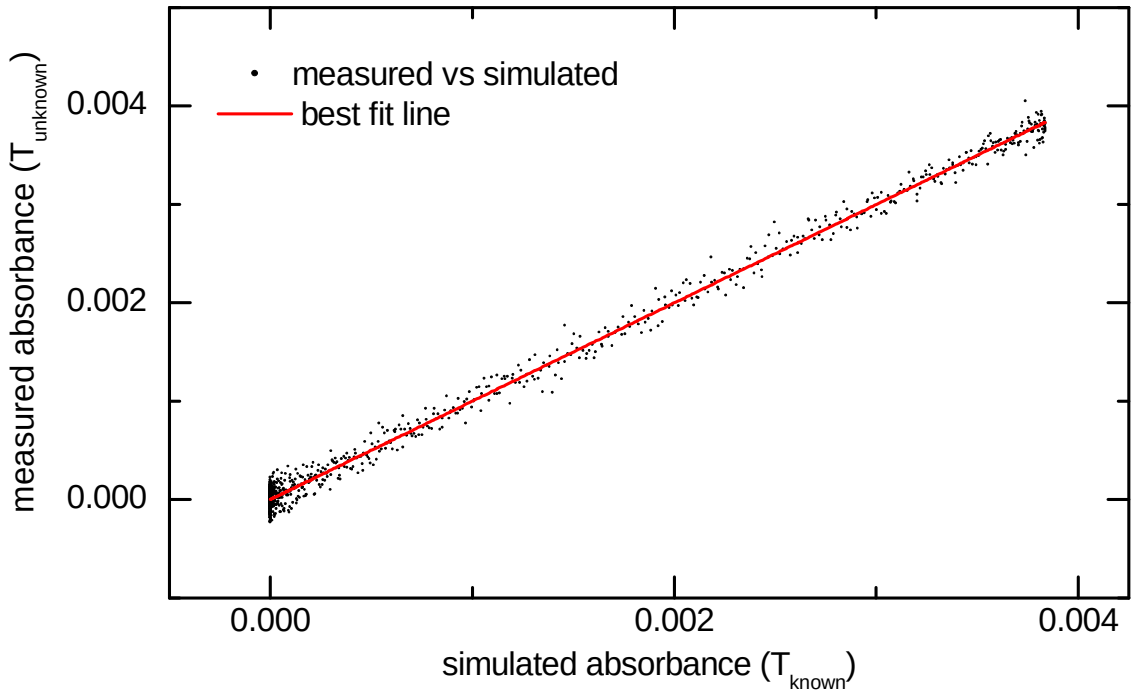

Figure 3.13 Example of the least square fitting method to infer temperature. The measured absorbance at some unknown temperature is plotted against a simulated spectrum at a known temperature and the best fit line is computed from this scatter plot. Note that the points in the spectrum that have very low absorbance (near (0,0) point) all fall in a single vertical plane and hence the fit is inherently weighted by the magnitude of the absorbance.

In order to construct a better estimate of the temperature uncertainty, the least square residual equation shown in equation 3.23 can be modified to include weighting of the regression. The new least squares residual equation now looks like this:

$$R^2 = \sum_i w_i \left[\ln(\alpha / \alpha_{ref})_i - \left(b + sE_i\right) \right]^2 \tag{3.29}$$

A weighting factor, w_i, has been added to more accurately reproduce the method of inferring temperature through spectral fitting.

Carrying out the analysis in the same fashion as before, leads to the following weighted least squares (wLS) function for the temperature uncertainty.

$$\Delta T_{wLS} = \frac{\partial T}{\partial s}\Delta s = \frac{k_B T^2}{\left|\overline{wE}^2 - \overline{w}\,\overline{wE^2}\right|} \sqrt{\sum_i \left(\frac{w_i \Delta \alpha_i}{\alpha_i} \right)^2 \left(\overline{wE} - \overline{w}E_i \right)^2} \tag{3.30}$$

The appropriate choice for the weighting factors should be based on the magnitude of the absorbance and these weights should be positive. In order to meet these requirements a possible formulation for the weighing factors is:

$$w_i = \frac{\alpha_i^2}{\sum_i \alpha_i^2} \tag{3.31}$$

Reapplying this wLS function to the full spectrum data and comparing the relative temperature uncertainty results to those obtained through spectral fitting yields much better agreement and this can be seen in Figure 3.14.

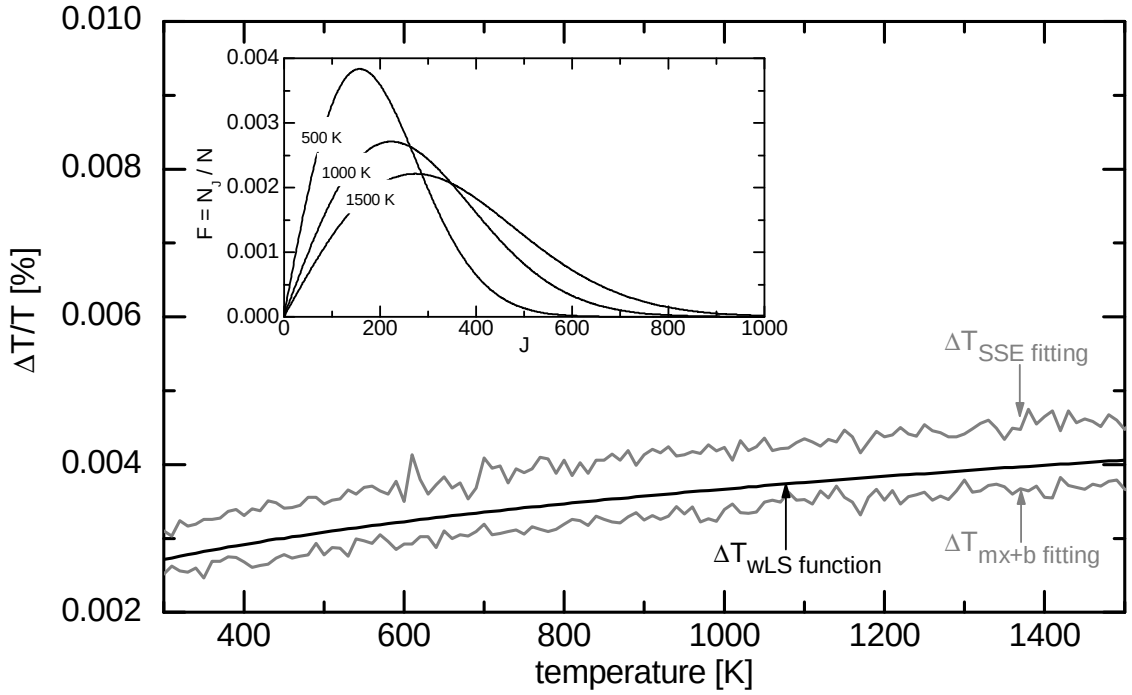

Figure 3.14 Comparison of the results of the wLS function versus SSE and mx+b spectral fitting shows much better agreement as compared to the uwLS function when calculating the relative uncertainty for the entire spectrum (1000 wavelengths spaced at increments of 1).

The wLS function for the temperature uncertainty follows the same trend as two different methods of spectral fitting. The observed difference between the SSE method and mx+b method is attributed to the same effect that caused the uwLS function to misbehave when considering many wavelengths with very low (~0) absorbance. The SSE method just considers the errors due to noise between the measurement and the simulation and can be unfairly biased when many points with low SNR are included. The least square solutions when spectral fitting (whether fitting to y=mx or y=mx+b) have an inherent built in weighting mechanism in that points with low absorbance (low SNR) are essentially averaged in the fit and through iteration to infer temperature have an equal effect at all temperatures.

From a practical standpoint, the 2 parameter least square solution (mx+b) should be considered first since it will be less sensitive to baseline errors which are almost always present when measuring an absorption spectrum. However, if a reduced wavelength count system is being used, the baseline is reliably measured, and the wavelengths have a SNR greater than 1, the SSE and both the 1-parameter and 2-parameter least square solution give equally reliable results. This is also true for the uwLS and wLS functions for predicting the temperature precision of a measurement and therefore the results for the N wavelength, known temperature case above using the uwLS function are still the correct results.

There is one caveat for the spectral fitting methods if the absorber mole fraction is unknown. The SSE method as described would need to be modified by including some form of normalization to account for bias from the measured and simulated absorbances being of different magnitudes. For instance, the error between the measured and simulated spectra would be dominated by a global difference in absorption strength and not posses a minimum in the SSE versus temperature curve. In practice, either of the least square solutions is recommended first.

Now that a final and more appropriate function for estimating the precision of a temperature measurement has been formulated, the case of N wavelengths at some unknown temperature can be considered. The objective function to be minimized for this case is similar to the 2 wavelength case at an unknown temperature.

$$\sum_T \frac{\Delta T_{wLS}}{T} = \sum_T \frac{k_B T}{\left| \overline{wE}^2 - \overline{w}\,\overline{wE^2} \right|} \sqrt{\sum_i \left(\frac{w_i \Delta \alpha_i}{\alpha_i} \right)^2 \left(\overline{wE} - \overline{w}E_i \right)^2} \tag{3.32}$$

Similar to before, the objective function is chosen as the sum of the relative uncertainty over a range of temperatures. Applying this objective function to the DE optimization scheme yields the results shown in Figure 3.15

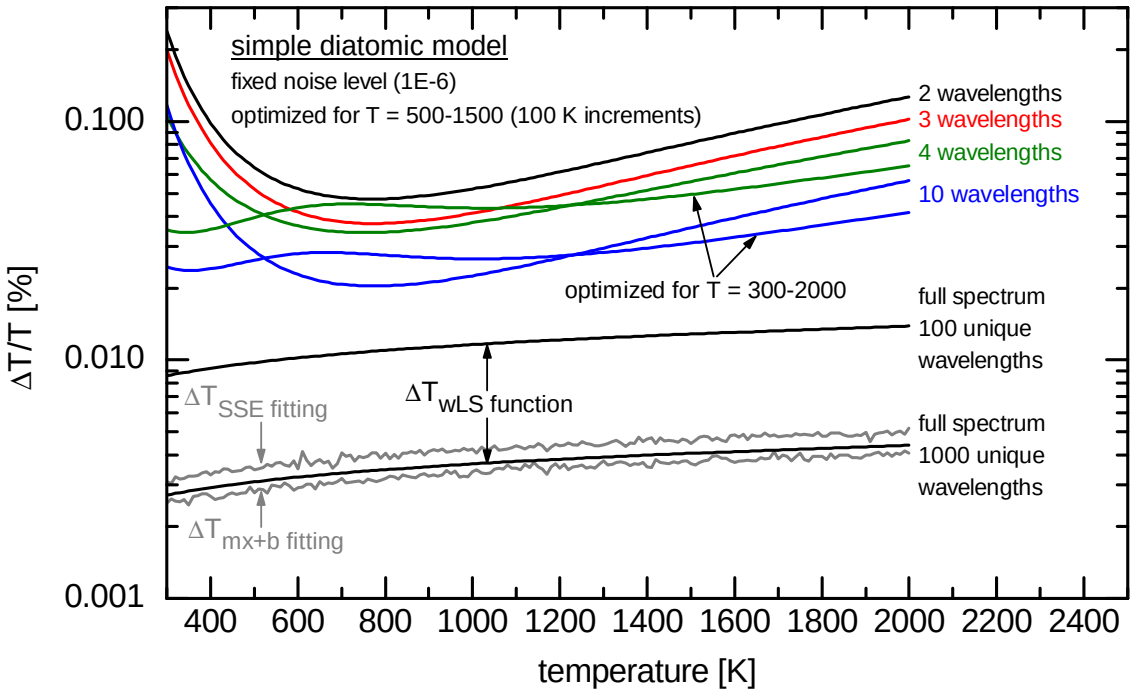

Figure 3.15 Temperature precision results of the N wavelengths, unknown temperature case for the IDM model. Again, it is evident that adding more wavelengths results in better performance across the entire temperature range considered when adding wavelengths has no adverse effect on the measurement (i.e. the noise is constant regardless of the size of N).

Similar to the 2 wavelength case, adding more wavelengths improves the performance at all temperatures considered when the wavelengths can be added without penalty. Also, similar to the case of N wavelengths at a known T, considering more than 2 wavelengths still results in only 2 unique wavelengths. This is due to the overall smooth shape of the spectrum. A real

spectrum would consist of many discrete features that may result in picking unique wavelengths when considering a range of temperatures.

For the IDM, an inequality constraint can be added to the optimization that forces the solution to N unique wavelengths, albeit N unique wavelengths that optimizes the temperature precision. If the constraint is added that the Js selected must differ by at least 10 and the noise is assumed to scale with square root of the number of wavelengths (simulating the performance at a fixed measurement time versus fixed noise) the following results are obtained shown in Figure 3.16.

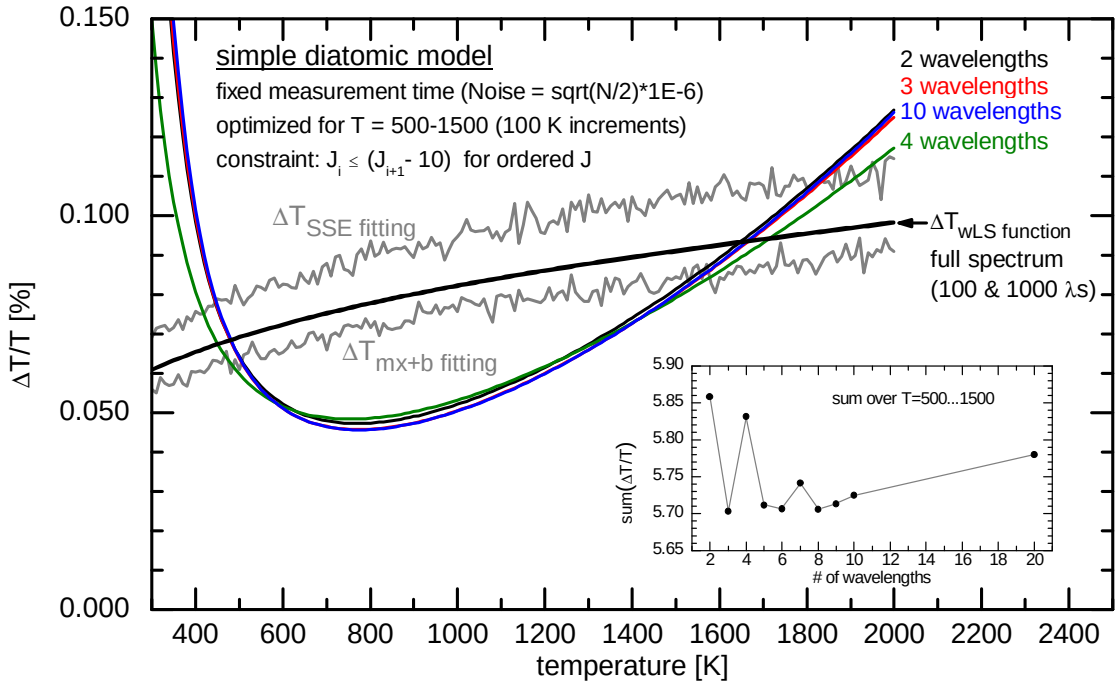

Figure 3.16 Temperature precision results obtained when considering N wavelengths over a range of temperatures and including the constraint that the wavelengths must be unique and the measurement time is fixed. This figure shows that the performance can be improved by smartly using the allowed measurement time focusing only on the critical wavelengths.

The four cases considered so far have only considered the wavelength selection problem for the ideal diatomic model (the Boltzmann distribution). Although this model is representative of the global temperature information in a real molecular spectrum, it lacks the discrete nature of what a real spectrum would look like. With that said, important results have been found that may be useful for attempting the wavelength selection problem for the H_2O spectrum and that is the focus of the next section.

3.4 H2O SPECTRUM

In order to apply the wavelength selection ideas from the IDM model to the H_2O spectrum a similar basis for the water spectrum is needed. That is, a linear relationship is needed between the natural log of the ratio spectrum and some description of the lower state energies. The BT2 and HITRAN databases include values for the lower state energies but when considering the actual spectrum, significant blending of transitions occur due to various broadening mechanisms. For practical combustion applications, the dominant broadening mechanism is typically collisional broadening which mainly depends on the pressure of the gas and at high pressures (P > 1 bar) distinguishable features are actually comprised of many individual transitions.

Working directly with the spectrum instead of the more fundamental parameters such as line intensities and lower state energies is attractive since the spectrum is an effective data compression tool. For instance, over the range 7220-7550 cm^{-1} there are approximately 25,000 transitions in the BT2 database that meet the requirements of line strength greater than 1E-28 [cm/molecule] and whose ratio of intensity to maximum intensity in the range considered is greater than 1E-5. Without this threshold, the number of transitions in this

relatively narrow spectral range is many orders of magnitude greater. Contrast this to a spectrum over the same spectral range at atmospheric pressure, which would require at most 4000 points to adequately resolve the lineshapes and the merits of using the spectrum are quickly realized. The situation is improved even further when dealing with spectra at elevated pressures which require even less points to adequately represent the spectrum.

Another reason, and probably the most important one, for working directly with the spectrum is that it is usually the actual physical quantity that is measured in an experiment. Fundamental properties of the species being probed can be inferred from a measurement of its spectrum. Therefore, for wavelength selection for H_2O absorption thermometry it would be useful to have a method to choose wavelengths based only the absorption spectrum and for this method to be quantitative.

In order to apply the ideas from the Boltzmann distribution developed earlier to the water spectrum, a method of interpreting the dependence of the absorption to temperature is required. Figure 3.17 below shows the line strength versus wavelength at three temperatures for the 3 most prominent vibrational bands in this spectral range. The effect of increasing temperature is similar to the IDM in that more lines become appreciable populated and the peak absorbance of the band moves toward lines having higher lower state energies. What is different, though, is that there is more than one vibrational band that has rotational transitions in this spectral range. Therefore, there is not a one to one correspondence with wavelength and energy as there was in the IDM. For instance, in looking more closely at the bottom panel of Figure 3.17, there are regions (e.g. 7300 cm^{-1}) where lines from the ground state of $\nu_1+\nu_3$ band have similar absorbance to lines from the first hot band of the $\nu_1+\nu_3$ band. The

effect of these two closely located highly different lower state energy lines on the spectrum would not be captured in a wavelength selection routine based only on the line strengths.

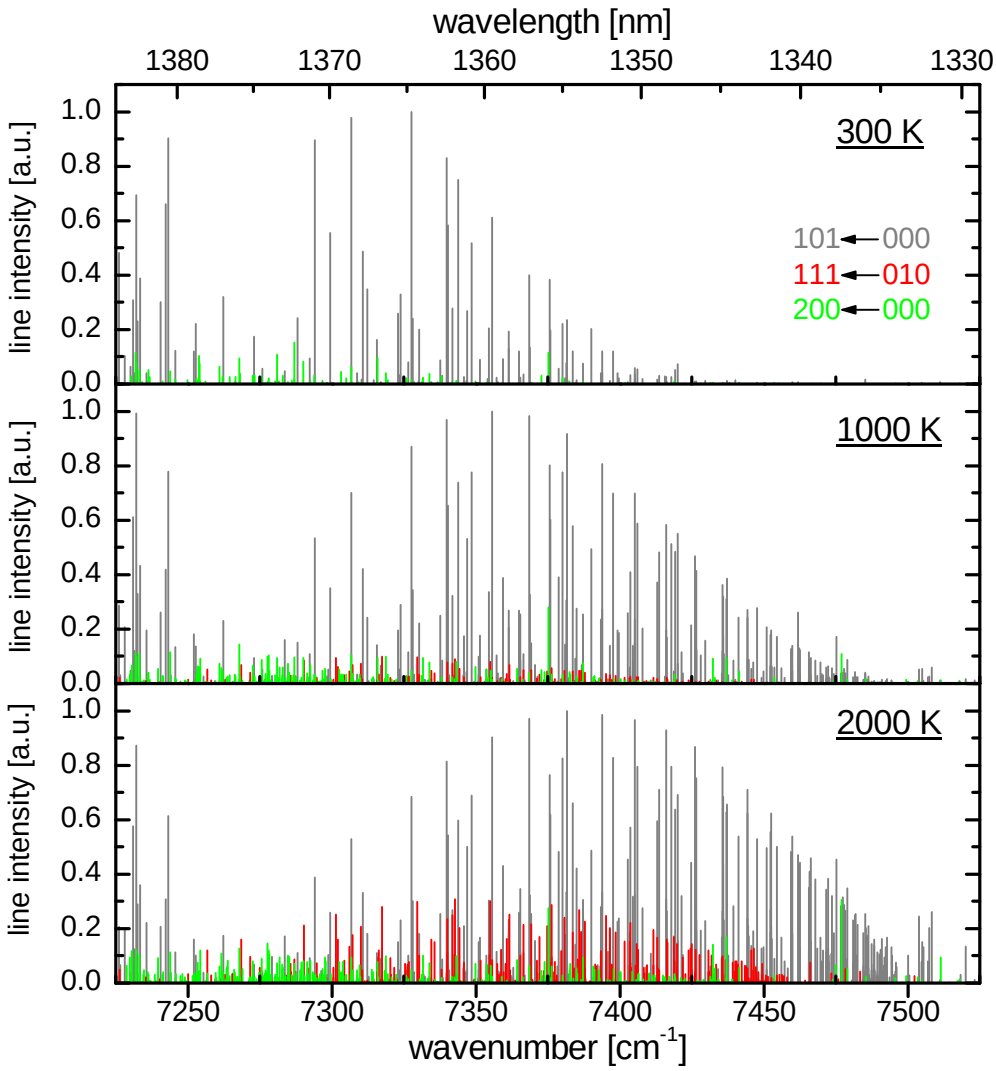

Figure 3.17 The intensities of rotational transitions for the three strongest vibrational bands of water in the 7225-7525 cm^{-1} range for three different temperatures. The redistribution of the intensities as a function of temperature is readily seen and is determined by the Boltzmann distribution.

The spectral absorption coefficient can be derived based on Einstein's theory of radiation [40].

$$k_\nu(T) = \frac{h\nu}{c} n_1 B_{12} \left(1 - e^{-\frac{h\nu}{k_B T}} \right) \phi(\nu) \tag{3.33}$$

Where n_1 is the number density of molecules in the ground state, B_{12} is the Einstein coefficient for stimulated absorption, and $\phi(\nu)$ is the line shape function. If the ratio of this equation is taken at T and T_{ref} the result is the following expression:

$$R_{T,T_{ref}} = \frac{k_\nu(T)}{k_\nu(T_{ref})} \approx \frac{\phi(\nu,T)}{\phi(\nu,T_{ref})} \frac{n_1(T)}{n_1(T_{ref})} \tag{3.34}$$

The stimulated emission terms $\left(1 - e^{-\frac{h\nu}{k_B T}} \right)$ have been neglected given the wavelengths and temperatures for most combustion applications would result in this ratio being very near one.

If the lineshape function is taken to be a Voigt profile, the temperature dependence can be approximated by the following:

$$\begin{aligned} \phi(\nu) &= \phi_D(\nu) V(a,w) \\ \phi_D(\nu) &\sim \frac{1}{\sqrt{T}} \\ \phi(\nu) &\sim \frac{1}{\sqrt{T}} \end{aligned} \tag{3.35}$$

Furthermore, the ratio of the number densities in the lower energy states can be described by the Boltzmann distribution leading to the following expression for the ratio of the absorption coefficients.

$$R_{T,T_{ref}} = \sqrt{\frac{T_{ref}}{T}} \frac{Q(T_{ref})}{Q(T)} \frac{e^{-\frac{E''}{k_B T}}}{e^{-\frac{E''}{k_B T_{ref}}}} \tag{3.36}$$

This ratio is valid for the case of single, isolate transitions. However, the more interesting situation to consider would be when there are many transitions contributing to make a single, blended feature. One way to consider this case is to reconsider equation 2.4.

The sum of the lineshape weighted line strengths can be considered "aggregate" line strength,

$$\alpha_\nu = k_\nu L = N \cdot L \cdot S_a \tag{3.37}$$

The ratio of two spectra can then be expressed as:

$$R_{T,T_{ref}} = \sqrt{\frac{T_{ref}}{T}} \frac{Q(T_{ref})}{Q(T)} e^{-\frac{E''_a}{k_B}\left(\frac{1}{T}-\frac{1}{T_{ref}}\right)} \tag{3.38}$$

The important thing to note in this expression is the lower state energy in the Boltzmann exponential, E"$_a$, has been termed the "aggregate" lower state energy. It is in effect, a weighted sum of all the lower state energies that contribute to the absorption at a particular wavelength. This is the key idea for interpreting the temperature dependence of the spectrum directly. It should also be pointed out that the idea of an aggregate lower state energy is a property of the spectrum. That is, it depends on the conditions of the spectrum (i.e. temperature) and is not a fixed property similar to the lower state energy levels of the actual individual transitions. Furthermore, it is recommended to use a reference temperature close to the actual temperature to minimize the effect of the lineshape function on the resulting ratio.

For this reason, this method is not a technique for inferring temperature in an experiment but this constraint does not affect its use as a tool for aiding in wavelength selection.

From the above equations, the aggregate lower state energy can be defined as:

$$E_a^{"} = \frac{k_B \ln\left(R_{T,T_{ref}} \sqrt{\frac{T}{T_{ref}}} \frac{Q(T)}{Q(T_{ref})} \right)}{\left(\frac{1}{T_{ref}} - \frac{1}{T} \right)} \tag{3.39}$$

Similarly to the IDM, taking the natural logarithm of the ratio spectrum yields the following linear relationship between the ratio and the aggregate lower state energy.

$$\ln\left(R_{T,T_{ref}} \right) = \ln\left(\sqrt{\frac{T_{ref}}{T}} \frac{Q(T_{ref})}{Q(T)} \right) + E_a^{"} \left(\frac{1}{k_B T_{ref}} - \frac{1}{k_B T} \right) \tag{3.40}$$

Figure 3.18 plots the ratio spectrum using simulated H_2O absorption spectra versus an aggregate lower state energy for three different temperatures. The temperature dependence of the slope of these lines is the same as in the IDM model and based on this the same ideas used for selecting wavelengths to optimize the temperature precision in the IDM model can be applied to the H_2O spectrum.

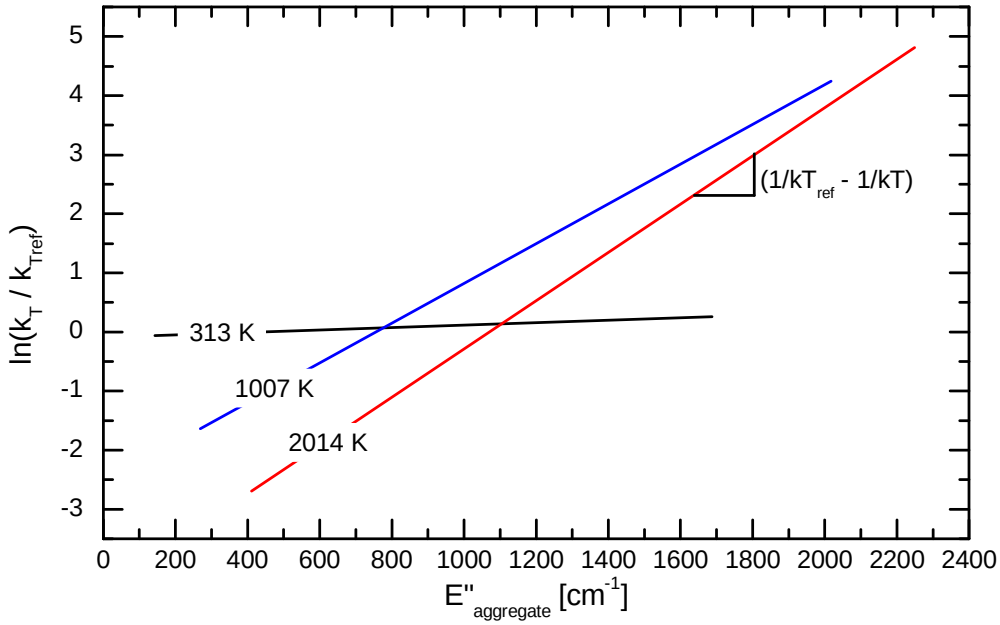

Figure 3.18 The water spectrum shows the same linear relationship as the IDM when plotting the natural log of the ratio of the spectrum to a spectrum at a reference temperature versus an aggregate lower state energy. The slope of these curves has the same simple dependence on temperature as the curves in the IDM.

3.4.1 Case 1: N wavelengths, known temperature

Similar to the cases presented in the IDM model, the wavelength selection procedure is to search for a global minimum of an objective using the differential evolution (DE) genetic algorithm. Since the physics of the H_2O spectrum are similar to those in the Boltzmann model (owing to the fact that the populations of H_2O molecules are distributed according to the Boltzmann distribution) the same objective function based on the weighted least squares regression can be used to solve the H_2O wavelength selection problem. Therefore, the objective function for the single, known temperature H_2O case is:

$$\frac{\Delta T_{wLS}}{T} = \frac{k_B T}{\left|\overline{wE_a^{"2}} - \overline{w}\;\overline{wE_a^{"2}}\right|}\sqrt{\sum_i \left(\frac{w_i \Delta\alpha_i}{\alpha_i}\right)^2 \left(\overline{wE_a^{"}} - \overline{wE_{ai}^{"}}\right)^2} \tag{3.41}$$

The results of optimizing this objective function for 2,3,4 and 10 wavelengths at two different temperatures is shown below in Figure 3.19 and Figure 3.20. The 2 and 3 wavelength cases resulted in 2 and 3 unique wavelengths to be found. However, for this single temperature case, 4 or more wavelengths resulted in duplication. In order to find 4 or more unique wavelengths the following inequality statement was added to the optimization routine.

$$\nu_i \leq (\nu_{i+1} - 2) \quad for\ ordered\ \nu \tag{3.42}$$

The choice of 2 cm^{-1} as the distancing factor was based on the Lorentzian width used to simulate the spectrum. For the spectra considered, the Lorentzian component of the Voigt function was set to 1 cm^{-1} so the choice of 2 as the distancing factor was used to ensure unique features would be selected. When choosing wavelengths for an actual application the choice of the distancing factor can be arbitrarily set based on the lasers available. For instance, one possible choice for the distancing factor would be to set it to the spectral resolution of the instrument used to measure the spectrum.

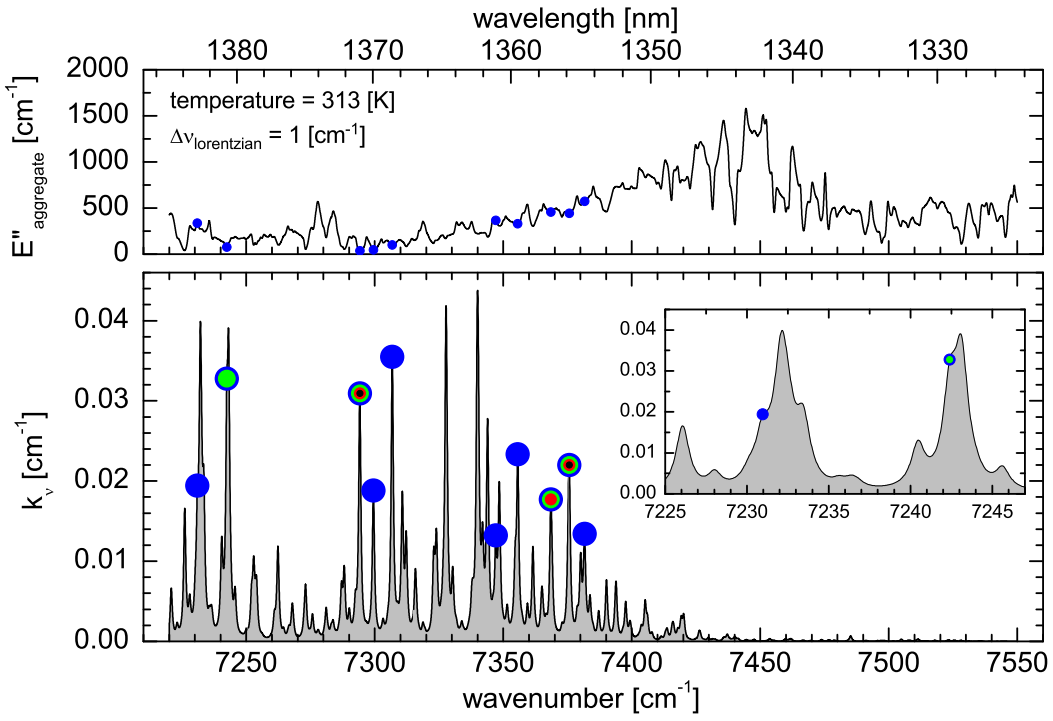

Figure 3.19 BOTTOM PANEL: Overlaid on the spectrum is the best wavelength choices for 2, 3, 4, and 10 wavelengths at a temperature of 313 K with these choices represented by the sized and colored points (2 – black, smallest….10 – blue, largest). TOP PANEL: The aggregate lower state energy for this spectrum showing the best 10 wavelengths.

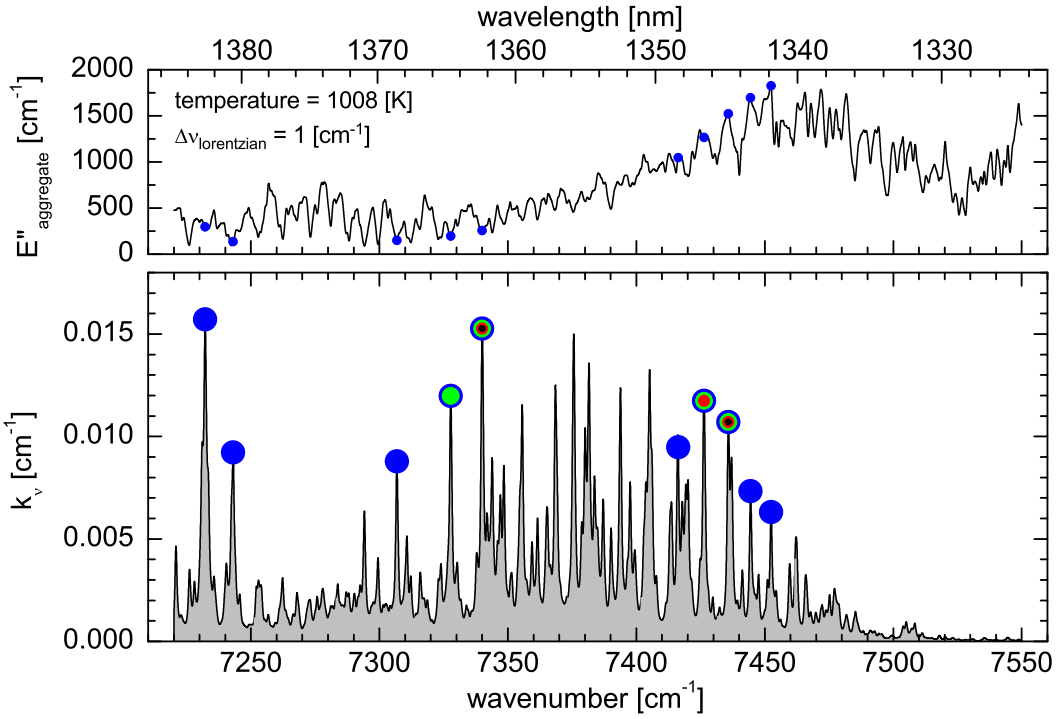

Figure 3.20 BOTTOM PANEL: Overlaid on the spectrum is the best wavelength choices for 2, 3, 4, and 10 wavelengths at a temperature of 1008 K with these choices represented by the sized and colored points (2 – black, smallest….10 – blue, largest). TOP PANEL: The aggregate lower state energy for this spectrum showing the best 10 wavelengths.

In these figures the best 2 wavelengths are represented by the smallest circles (black) and the best 10 are represented by the largest circles (blue). Interestingly, the results for both temperatures have the same trend that the best 3 wavelengths includes the best 2 and the best 4 wavelengths includes the best 3 and so forth. Also, if an average energy of the spectrum is computed as k_BT, the region around this value on the aggregate lower state energy curve is absent of any optimal wavelength choices. The k_BT point roughly corresponds to the energy at which the Boltzmann distribution is maximized. As was seen in the ideal diatomic model (Boltzmann distribution) the peak value of the Boltzmann distribution is not the optimal

place for locating wavelengths in that the temperature sensitivity is not as good as locations off of the peak.

Before moving on to the more interesting case of N wavelengths at an unknown temperature it is important to test the accuracy of the ΔT_{wLS} function against the performance using a spectral fitting method. In Figure 3.21, the performance of the wLS function along with least squares spectral fitting method is plotted for the best 10 wavelengths chosen above for the T=1007 K case and for considering the entire spectrum. As can be seen, the results of the wLS function show very good agreement (factor of 2 at worst case) to those obtained through spectral fitting. A possible source of discrepancy between the two is believed to be due to the coarseness of the temperatures used in spectral fitting. The temperatures in the database used for the fitting were separated by 5% (in order to reduce the computational time of the fitting procedure) yet the worse case temperature precision in the figure is ~ 4%. A more highly discretized database should be tested to see if the two methods can show even better agreement. With that said, the trends are very similar and this leads to a high level of confidence that the wavelengths selected by optimizing the wLS function are the optimal.

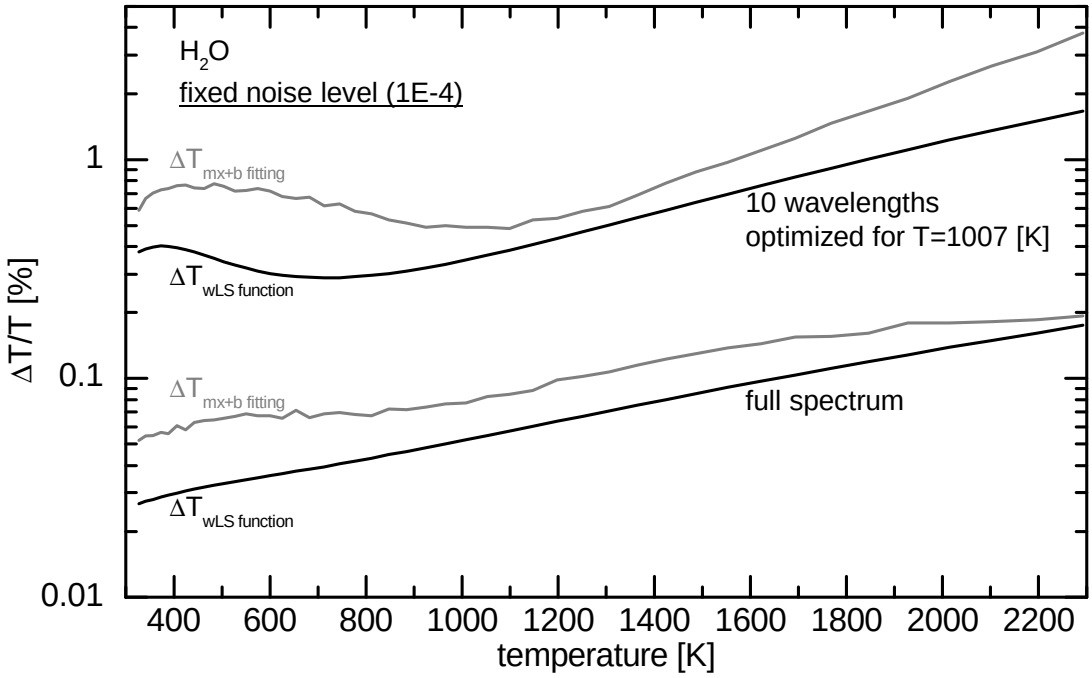

Figure 3.21 Temperature precision results from the ΔT_{wLS} function and from least square spectral fitting using the 10 best wavelengths chosen for optimizing at 1007 K and using the entire spectrum. At worse case, the two techniques differ only by a factor of 2 but more importantly the trends are nearly identical leading to confidence in the wavelengths selected using the ΔT_{wLS} function.

3.4.2 Case 2: N wavelengths, unknown temperature

Of all the cases presented in this thesis, this particular case is of most interest for designing temperature sensors based on absorption spectroscopy. For most practical applications, the ideal sensor would provide good sensitivity over the entire range of temperatures encountered. The actual range will be application specific and the proper design can reflect this by using an estimate based on prior knowledge or experience. In order to motivate the ideas of this section, two examples are considered.

Example 1: Wide temperature range

The objective function used for finding the best wavelengths for the H_2O spectrum case is similar in form to the one used in the IDM model in that the sum of the relative uncertainties for the range of temperatures considered is used.

$$\sum_T \frac{\Delta T_{wLS}}{T} = \sum_T \frac{k_B T}{\left| \overline{wE_a''^2} - \overline{w}\,\overline{wE_a''^2} \right|} \sqrt{\sum_i \left(\frac{w_i \Delta \alpha_i}{\alpha_i} \right)^2 \left(\overline{wE_a''} - \overline{wE_{ai}''} \right)^2} \tag{3.43}$$

The results of optimizing this objective function for 2,3,4 and 10 wavelengths over the temperature range of 313-1768 K is shown below in Figure 3.22. In this figure, the best 2 wavelengths are again represented as small black circles, best 3 larger red circles, best 4 even larger green circles, and the best 10 are represented with the largest blue circles. The results for optimizing over a range of temperatures is different from the single temperature case in that the best set of 3 do not include both of the best 2 and the best 4 do not include all of the best 3 and so forth. In fact, the best 10 includes all of the best 2, 3, and 4 except for one of the best 3 wavelengths. This behavior was not expected and reinforces the idea that optimizing wavelengths for a range of temperatures can not be done by only considering a single temperature but rather the entire range must be included in the analysis.

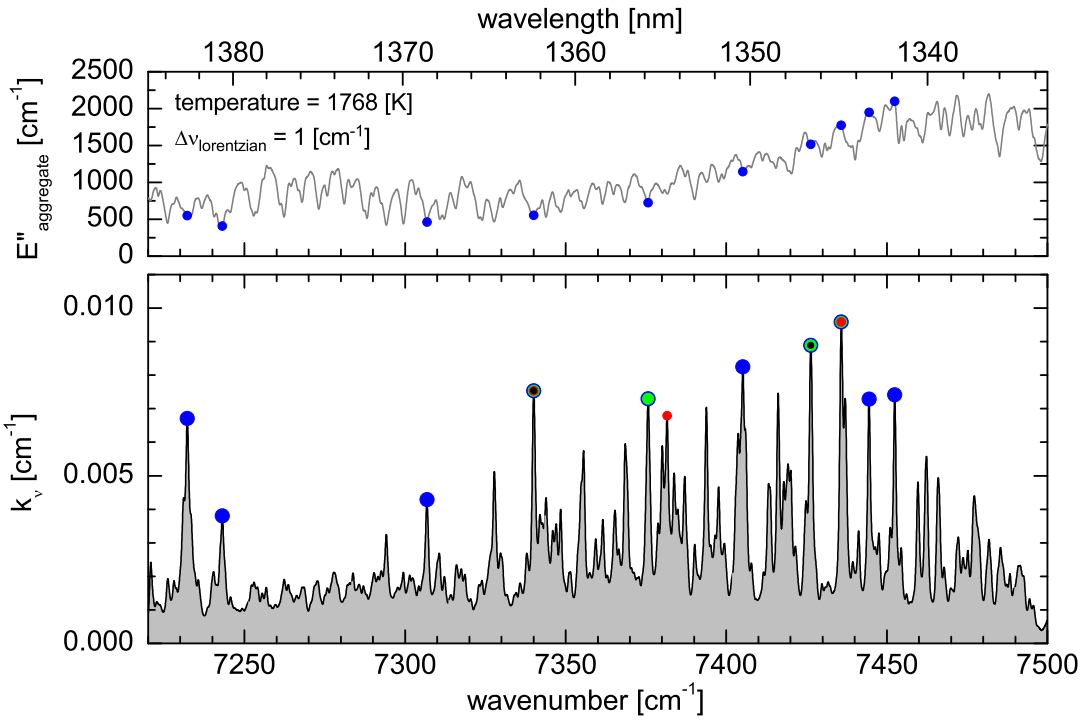

Figure 3.22 BOTTOM PANEL: Overlaid on the spectrum at 1768 K is the best wavelength choices for 2, 3, 4, and 10 wavelengths optimized over the temperature range of 313 – 1768 K with these choices represented by the sized and colored points (2 – black, smallest….10 – blue, largest). TOP PANEL: The aggregate lower state energy for this spectrum showing the best 10 wavelengths.

The other interesting observation is that the best choices for 2, 3, 4, and 10 wavelengths no longer exhibit the behavior of tending to points to maximize the difference in lower state energies but rather try to cover a distribution of lower state energies. For instance, for the 3 wavelength case at a single, known temperature, two of the wavelengths optimized to features that were close in lower state energy and much higher than the other wavelength. However, in the figure above, the third wavelength optimizes to a point approximately midway between the energies of the best 2. This is reinforced even more when considering the 4 and 10 wavelength selections.

In order to quantify these wavelength selections, the performance of these choices along with an optimization at 25 wavelengths and the entire spectrum is plotted below in Figure 3.23. At a fixed noise level, the temperature uncertainty is reduced with increasing number of wavelengths. However, in practice, adding more wavelengths usually comes at the expense of increased noise when keeping the overall measurement time fixed.

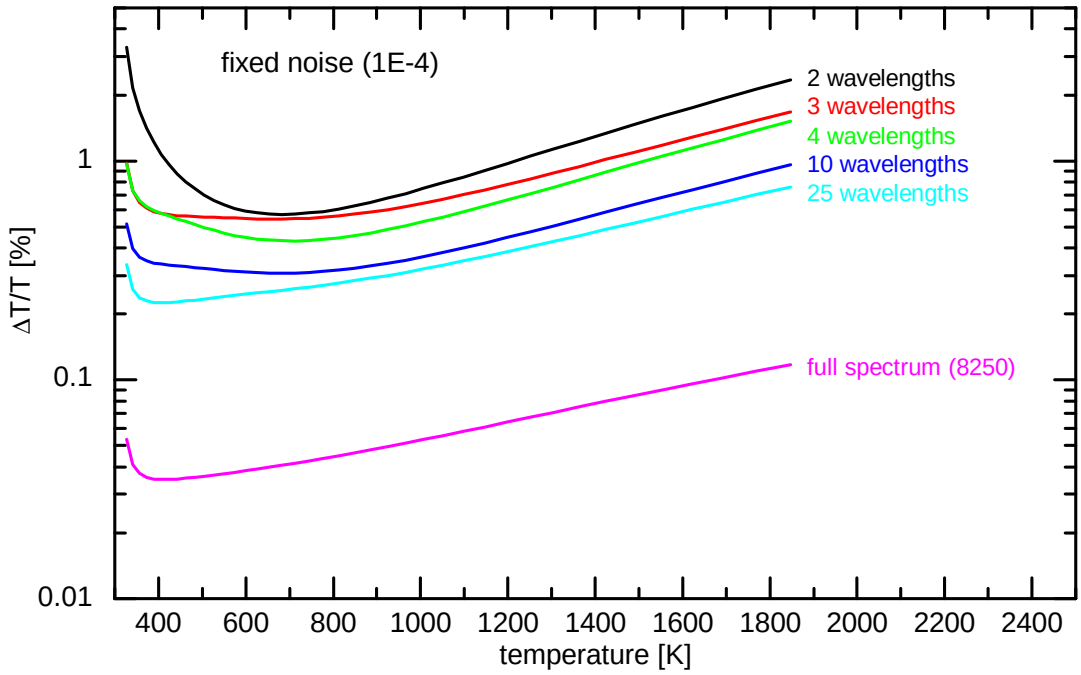

Figure 3.23 Relative uncertainty of best 2, 3, 4, 10, and 25 wavelengths for the H_2O spectrum when considering a wide range of temperatures. Also shown are the results when using the entire spectrum. For a fixed noise level, the performance improves with increasing number of wavelengths.

Figure 3.24 shows the temperature precision obtained when the measurement time is fixed thus increasing the noise with increasing wavelengths. For this case, increasing the number of wavelengths does not have the global trend of improving the performance. In fact, it would appear that there are an optimal number of wavelengths and this is indeed confirmed if

the sum of the errors across the temperature range is computed and this can be seen in Figure 3.25

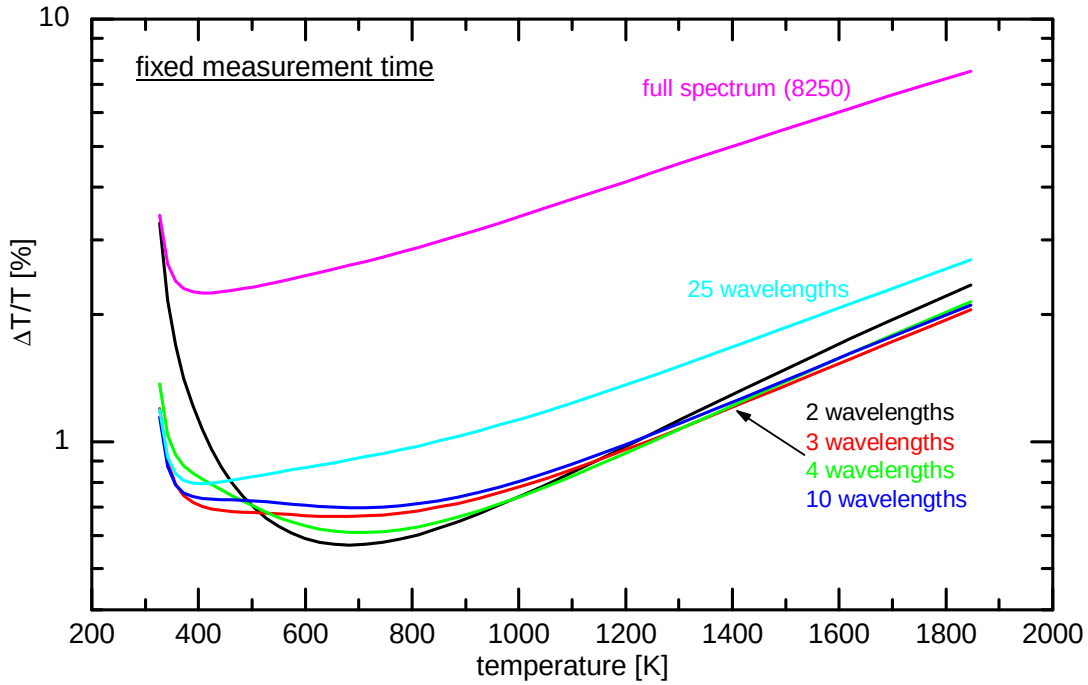

Figure 3.24 The relative uncertainties of the same wavelengths shown above but considering a fixed measurement time where wavelengths are added at the expense of increased noise in the measurement.

Below in Figure 3.25 are the results from the summing the errors across the range of temperatures considered for both the fixed noise and fixed measurement time cases. For the fixed noise case, the result of adding wavelengths is a steady decrease in the total error. That is, adding wavelengths without any additional cost to the noise in the measurement will provide better results. This is consistent with standard signal averaging concepts. On the other hand, considering a fixed measurement time where the cost of adding wavelengths is an increase in the measurement noise (i.e. spending less time per wavelength) there is an

optimal number of wavelengths and for the particular temperature range and spectral conditions considered; that optimum lies at 3 wavelengths.

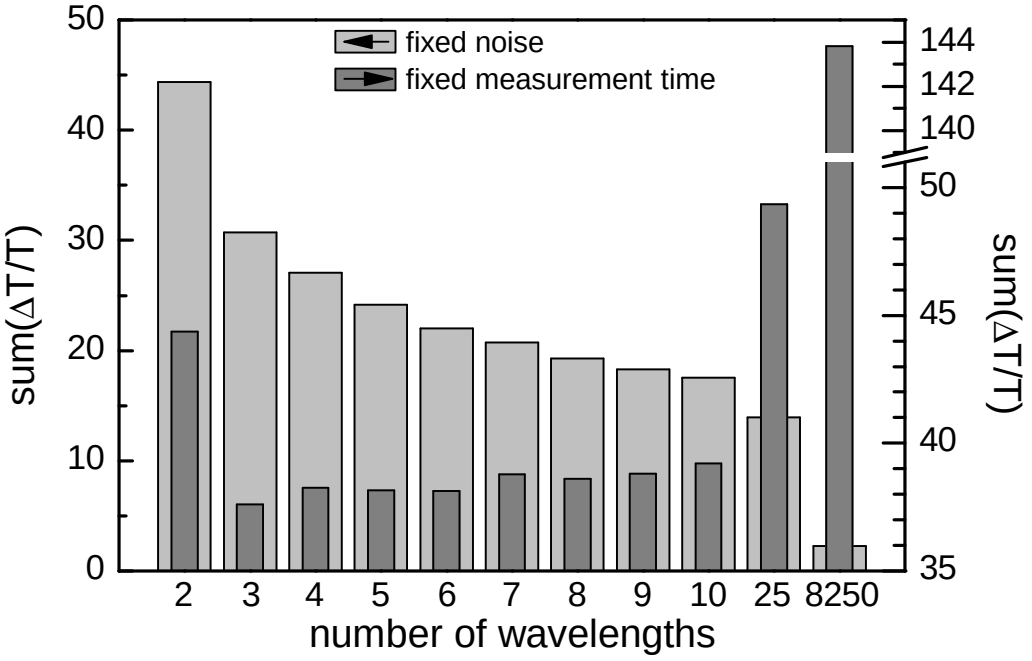

Figure 3.25 Comparison of the results obtained when considering either fixed noise or fixed measurement time. For the fixed measurement time case, the noise was assumed to scale with the square root of the number of wavelengths. In both cases, the noise for 2 wavelengths was set to the same level as a point for comparison. For a fixed measurement time, there are an optimum number of wavelengths, and for the conditions considered here that optimum lies at 3. However, the penalty when considering the whole spectrum versus the 3 optimal wavelengths is only a factor of ~4 which could be important when other noise sources such as baseline uncertainties are considered.

The important points from the above case can be summarized as:

- When choosing wavelengths when considering a range of temperatures that the sensor should be optimized for, it is important to choose the wavelengths based on the performance over the entire range and not just picking wavelengths at some arbitrary temperature within the range
- The choices for higher wavelength counts might not include the choices made for lower wavelength counts.
- When considering a fixed measurement time, there may be an optimal number of wavelengths to sample in order to optimize performance. This depends on the temperature range considered and may also depend on the pressure.

Example 2: Two widely separated discrete temperatures

Another interesting example to consider would be optimizing performance through wavelength selection for the case where two widely separated temperatures are to be measured with a single sensor. For example, measuring the temperature in shock tubes requires an accurate measurement of temperature immediately before and after a reflected shock wave but perhaps the highly transient period during the shock is of marginal value or difficult to measure with a line-of-sight technique due to beamsteering effects.

For this case, two temperatures were considered and for making comparison with the wide temperature range case, the temperatures where chosen to match the endpoint temperatures of the previous example. The objective function for this example is the same as the one used in the previous example with the goal being minimizing the sum of the relative errors at the

two temperatures considered. The result of this example for 2, 3, and 4 wavelengths is shown below in Figure 3.26. Similar to the wide temperature range example, the best 3 wavelengths do not correspond to either of the best 2. In fact, the dispersion in wavelengths chosen for this example is much larger than the continuous temperature range example. However, the trend that the optimal wavelengths cover a distribution of lower state energies is still the same and the two examples yielded the same choices when considering the 2 wavelength case.

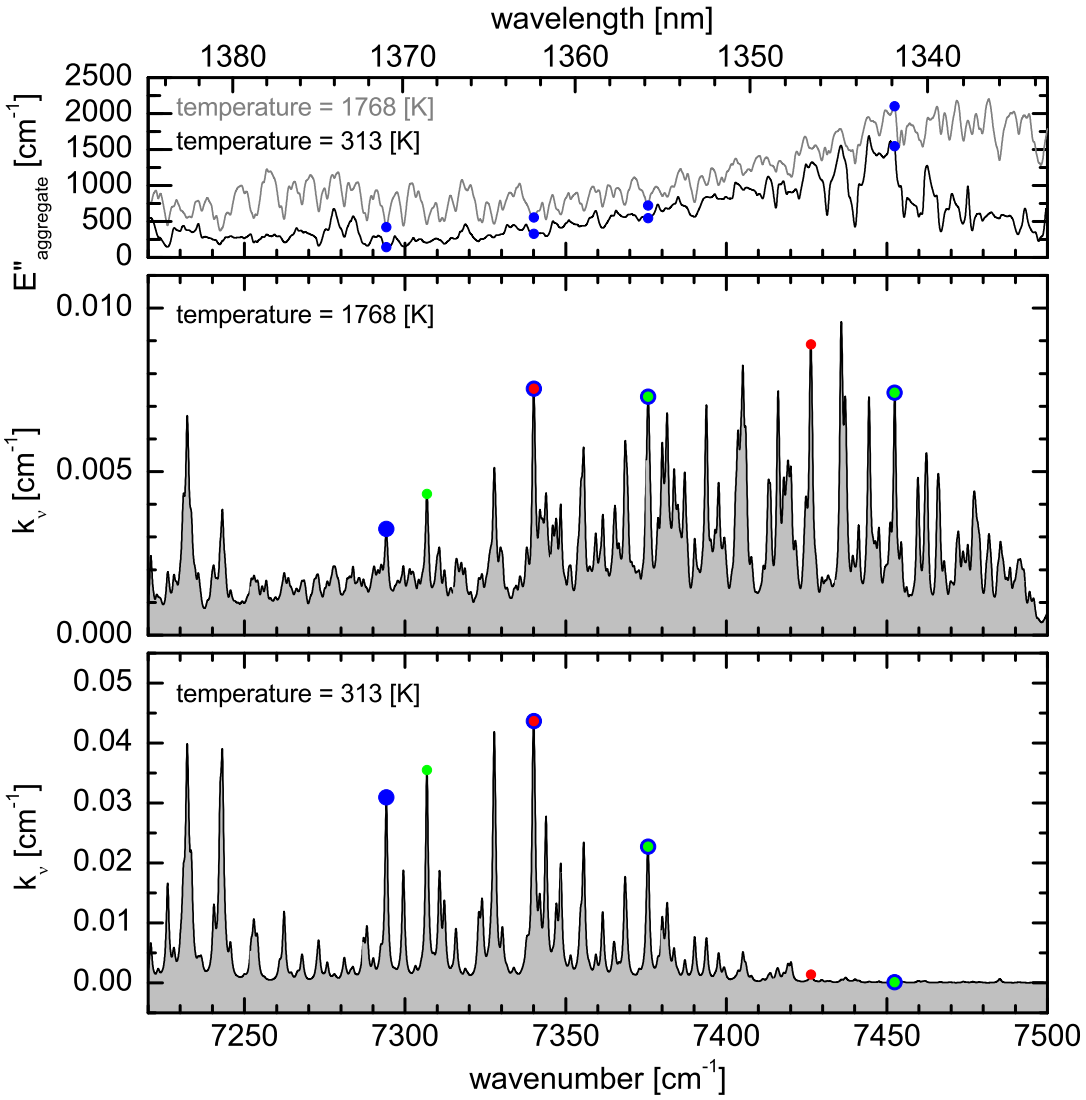

Figure 3.26 BOTTOM and MIDDLE PANELS: Overlaid on the spectra at 313 K and 1768 K are the best wavelength choices for 2, 3, and 4 wavelengths optimized for these two temperatures only. The best wavelength choices are represented by the sized and colored points (2 – red, smallest….4 – blue, largest). TOP PANEL: The aggregate lower state energies for the different temperature spectra.

In looking at the performance results of this 2 temperature example versus the wide temperature range example, it is shown that the performance at the temperatures considered for the 2 temperature example is improved versus the wide temperature range example at the

expense of decreased performance at the intermediate temperatures. Also, the best 2 wavelengths selected in both examples were the same. There appears to be some correlation for the 2 wavelength case in choosing the wavelengths based on the extremes of the temperatures considered.

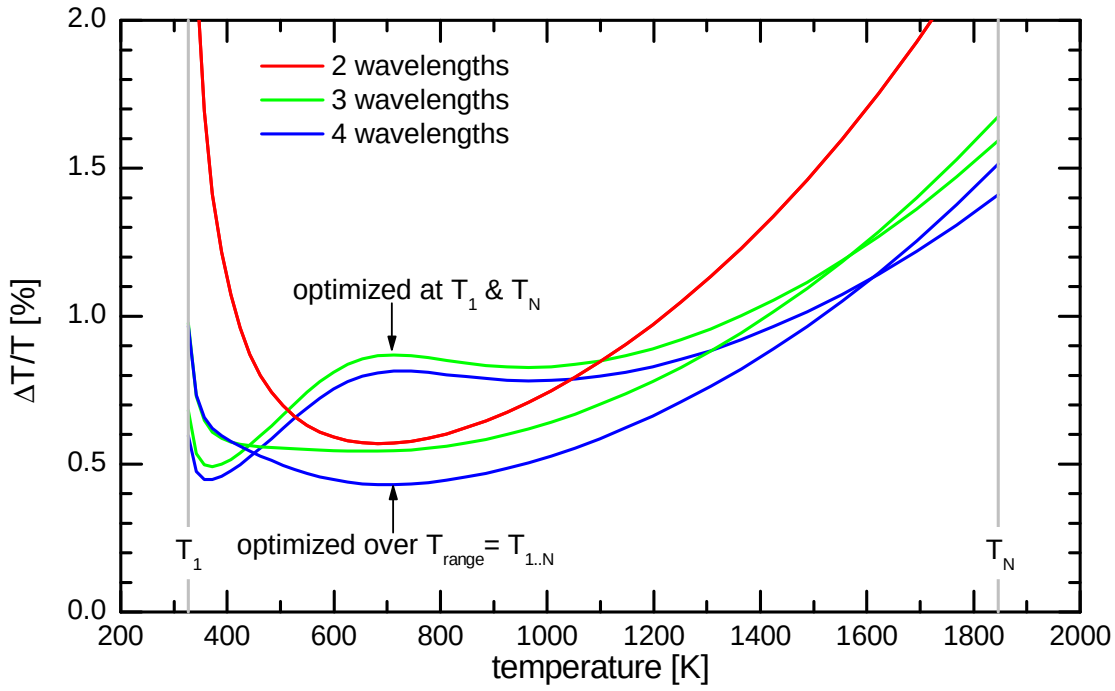

Figure 3.27 Comparing the temperature precision results of the wide temperature range and the two widely separated temperatures examples. The effect of not including the intermediate temperatures is easily visible in the 2 temperature case with a decrease in the precision at intermediate temperatures. However, the two temperature case does improve the performance at the temperatures considered versus the wide temperature range optimization.

Up to this point, the techniques employed for wavelength selection only considered the temperature dependence in the spectrum and the effects of random measurement noise. In practice, there will be other factors to consider when designing an absorption based

thermometry sensor. For instance, the baseline of the spectrum is usually an unknown function and can vary during the course of an experiment due to effects such as beamsteering, window fouling, time varying wavelength dependencies of components of the light source, light delivery components, and/or light gathering and detecting components. Certain practical techniques can employed to aid in the success of the absorption sensor.

3.5 PRACTICAL TECHNIQUES FOR WAVELENGTH SELECTION

Gas thermometry by molecular absorption spectroscopy is common [19,30,42-44]. In its simplest form, two colors (e.g., two fixed-wavelength lasers) are used, each spectrally aligned to an absorption feature of the same molecule. The features are chosen so that the ratio of the two resulting absorbance values is temperature sensitive [16].

This fashion of thermometry is improved by interrogating additional wavelengths. For instance, a third, fixed-wavelength laser is spectrally offset from each of the original wavelengths and aligned to an absorption minimum; the goal is usually to track absorbance biases due to factors other than the target absorber [5,21,45]. More spectrally offset fixed-wavelength lasers can be added, aligned to other absorption features (e.g., 9 and 19 wavelengths have been used for H_2O absorption thermometry [10,20]. These spectrally offset wavelengths improve the thermometry in many ways, such as:

- there is a simple advantage of more data, so that the overall signal-to-noise ratio is improved, consistent with standard signal averaging concepts

- wavelength-dependent effects including interfering absorbers, beamsteering, etalons, and window fouling may be more clearly revealed, ultimately reducing the sensitivity of the measurement to these effects

- as temperature changes, the wavelengths exhibiting the best combination of absorption strength and temperature sensitivity change; therefore by monitoring many wavelengths, one can be sure to maintain access to the best available features (those ultimately offering the best signal-to-noise ratio and temperature sensitivity)

- gas temperature distribution monitoring becomes possible because of the nonlinear dependence of the measured absorbance values on temperature [6]

Considering again the simple two-wavelength strategy, wavelengths can also be added directly adjacent to each of the two original wavelengths. Commonly, each of two lasers is tuned over a small spectral region including the target absorption feature. The goal is generally to monitor the spectral shape of each of the absorption features; ensuing spectral fitting can provide advantages such as:

- immunity to spectral offsets as in the three-wavelength approach

- pattern recognition: the target absorption feature can be distinguished from other interferences by monitoring its spectrum

- additional information can be obtained such as the gas pressure from the spectral width of the absorption feature(s)

The tuned laser approach essentially becomes a many-wavelength measurement (e.g., if each of 2 tuning lasers produces spectra that ultimately can be represented by 50 data points, the entire approach is considered a 100-wavelength approach).

Thus the two-wavelength approach can be improved in many ways by adding more wavelengths; this is true if the additional wavelengths are offset and true if they are directly adjacent to the original wavelengths. In the limit of adding wavelengths, one measures the entire available spectrum of the absorber at high spectral resolution. If done without including other drawbacks, this approach does provide good performance over a wide range of temperatures and pressures while maintaining the best immunity to systematic and bias errors. However, for the purpose of gas thermometry by absorption spectroscopy, a reduced, experimentally tractable approach using lower wavelength counts can perform even better when only considering precision errors as was shown previously.

3.5.1 Ratio spectrum

In the case of thermometry in engines where the temperature can vary between 300-2500 K, it is important to monitor features from a wide range of lower state energies to permit maximum temperature sensitivity at all temperatures of interest. Nominally, this amounts to monitoring an entire R, Q, or P branch – for this reason this approach is coined ‘full rotational coverage’ in molecular spectroscopy. As was shown in section 3.4.2, covering the entire branch is not necessary for optimal temperature sensitivity but the penalty in acquiring more points for fixed measurement duration may be tolerable given the added immunity to other adverse effects such as baseline errors. Shown below in Figure 3.28 and Figure 3.29 are plots of lower state energy versus wavenumber of transitions in the R branch of the $\nu_1+\nu_3$

water absorption band with the relative intensity of the transition represented by a color mapping. The data was based on values from the BT2 database and used the H_2O partition function of Vidler and Tennyson [23,46]. The left figure shows results at 500 K and the right figure is plotted for 2500 K. Immediately visible is the effect of increasing temperature on populating more energy levels and shifting the maximum intensity line to higher energy. If the required maximum temperature measurement was 500 K it is clear that monitoring frequencies above 7425 cm^{-1} would not give any more useful information and would ultimately decrease the overall noise performance of the measurement by adding unnecessary wavelengths, resulting in a higher sensor bandwidth for a fixed measurement period. However, in the engine thermometry situation, it is imperative to measure out to 7500 cm^{-1} to capture all the necessary temperature information for temperatures up to 2500 K. Scanning further than 7500 cm^{-1} in this case is unnecessary since the new transitions would not probe any lower state energies higher than previously sampled resulting in no new information and decreasing the overall SNR at fixed performance.

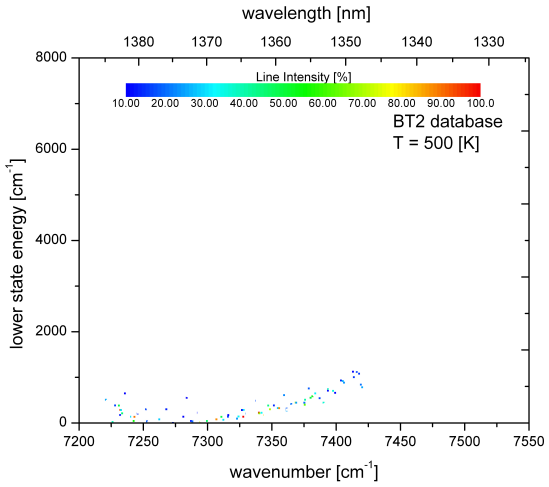

Figure 3.28 Lower state energy versus wavenumber of the transitions in the R branch of the $\nu_1+\nu_3$ H_2O absorption band. The relative intensities of each line are also depicted by the color mapping of each point.

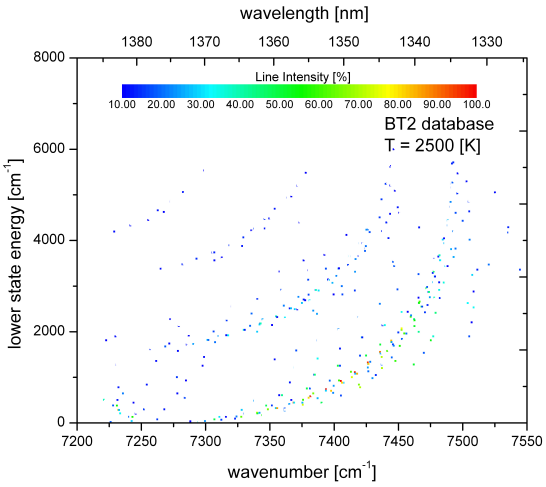

Figure 3.29 At high temperatures, more lines at higher lower state energies have appreciable absorption strength and to maintain temperature sensitivity it is imperative to cover the entire rotational envelope

When dealing with the spectrum directly, a simple representation of the lower state energies is through the use of the ratio spectrum. Diving a spectrum at temperature T by a spectrum at T_{ref} quickly show the regions of the spectrum that have differing aggregate lower state energies. For quickly selecting optimal wavelengths, selections should be made in order to maximize the difference in lower state energies while maintaining good SNR of the features chosen.

3.5.2 Difference spectrum

The ratio spectrum gives a picture of the differing lower state energies in the absorption spectrum (which are important to consider when selecting wavelengths for a range of

temperatures), but the optimal wavelengths for thermometry will also depend on the temperature sensitivity of features. A simple method of viewing the temperature sensitivity is through the difference spectrum. The difference spectrum is the simple subtraction of two spectra at different temperatures (T_{T1}-T_{T2}) where T_1 is slightly hotter than the temperature of interest and T_2 is slightly cooler. The difference spectrum is an approximation of the derivate of the spectrum with respect to temperature.

The difference spectra were calculated by subtracting a spectrum at a slightly colder temperature from one at a slightly higher temperature. An example of this difference spectrum at an average temperature of 1650 K is shown below in Figure 3.30. To maximize sensitivity at this particular temperature, the recipe would be to choose a color with the greatest positive value and one with the largest negative value. For a further discussion of wavelength selection based on this picture, the reader is referred to section 4.2.1.

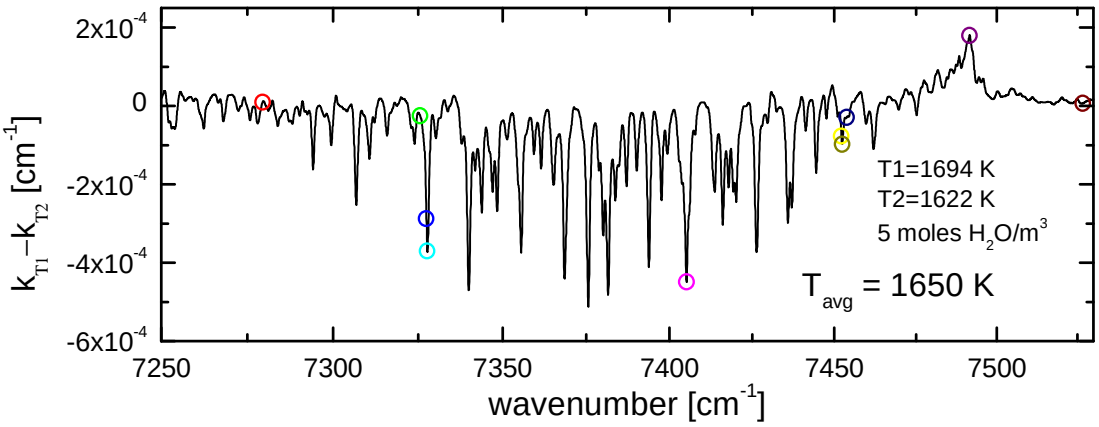

Figure 3.30 The difference between 2 spectra at 1694 K (T1) and 1622 K (T2). In this figure downward pointing features represent cold lines and upward represent hot. The circles represent wavelength choices for the application highlighted in section 4.2.1.

However, the overall accuracy of the system is not just limited by the choice of energy levels probed; it also requires precise knowledge or measurement of the lineshapes of the features of interest. Under conditions seen in the engine, the lineshape function can be described by a Voigt function with the Lorentzian (pressure) component dominating the Gaussian (Doppler) width. The overall width of each line is a function of temperature, pressure, and the collisional partners of the molecule being probed. Prescribing the broadening coefficients for each transition is a daunting task and much work has gone into measuring and modeling these parameters [18,34,47-49]. In a manner similar to choosing wavelengths for temperature sensitivity using difference spectra over a range of temperatures, wavelengths can be chosen for measuring the linewidths by varying the difference spectra over the range of widths estimated to be encountered in the experiment while holding temperature constant.

The following is a summary of the important points of the two previous sections:

- measure only enough features to sample from a wide range of lower-state energies (ratio spectrum)
- monitoring two branches (e.g., both R and P) is not much more valuable than monitoring one, because the information is essentially duplicated (ratio spectra are similar)
- it is most important to measure the ‘edges’ of the branch (i.e., features with the lowest available lower-state energies which are often near band center and features with the highest available lower-state energies which are often furthest from band center); however, in practice, the ‘edges’ shift spectrally as experimental conditions change due to the change in strength of the composite features, so it is usually advantageous to measure the ‘middle’ of the branch as well especially when considering a range of temperatures

- while it is attractive to monitor the ‘far edges’ of the branch, where features are very temperature sensitive, there is no merit in doing so if strengths will not be sufficient under the expected experimental conditions
- this highlights another advantage of measuring in the R branch where the high lower state energy lines (high J states) tend to overlap in the bandhead effectively summing the absorption intensity of the normally weak lines making it possible to measure highly temperature sensitive features
- it can be advantageous to include features originating from excited vibrational states (hot bands) provided their strengths are sufficient and this can reduce the required spectral coverage particularly in low pressure environments

This discussion provides a useful roadmap for designing sensors for maximizing temperature sensitivity when considering multiple different sources of noise and other interferences. However, only discrete wavelengths have been considered. The actual features will have some lineshape and this may or may not be well known. In order to still perform thermometry when the lineshape function is unknown, a continuous scan of the wavelength may be needed.

3.5.3 Continuous wavelength scan

Imagine starting at the limit of very low spectral resolution, for example scanning the R-branch of a molecule but resolving only the overall rotational envelope. As the spectral resolution is increased, features may appear (particularly if the gas pressure is low and the molecule is small). A spectral resolution at least sufficient to reveal these primary features is recommended, essentially because it will allow for spectral fitting in the final temperature

determination process [28]. Improving the spectral resolution from this point, the observed absorbance signal levels in the neighborhoods of these primary features may increase (if the pressure is low enough) due to reduced instrumental broadening. It is recommended to take advantage of these signal increases if possible. However, increasing the spectral resolution beyond this point generally appears to have diminishing returns. Although more spectral detail can often be observed, these details usually do not dramatically improve thermometry. This is because the many lower-state energies can already be sampled in the primary features; the additional temperature information that can be extracted from the details often does not warrant the requisite experimental complexity.

In the case of H_2O absorption thermometry, this 'full rotational coverage' approach is often used. Following the above two guidelines, H_2O spectra are typically measured that can be represented by 500 discrete wavelengths in a range that spans from approximately 1330 nm to 1380 nm. The span of ~ 50 nm encompasses most of the R-branch. Under typical combustion conditions of 30 bar, 1800 K, there are approximately 20 major temperature-sensitive features in this range, with lower-state energies spanning 0 – 4000 cm^{-1}. A resolution of only ~ 1 nm (~ 5 cm^{-1}) is needed to distinguish adjacent features. However, typically ~ 0.1 nm (~ 0.5 cm^{-1}) is used to reduce instrumental broadening and therefore increase signal (absorbance) values; this is particularly helpful when the gas pressure is low (< 5 bar).

The added benefit of scanning the entire spectrum with high spectral resolution is the ability to do digital smoothing of the measured spectra to artificially broaden the lineshapes to a known value. Heavy smoothing by convolution of the data with a broad Gaussian maintains

the temperature information but can reduce the uncertainty in knowing each lines broadening parameters; effectively making the measurement broadening insensitive. Figure 3.31 shows an example of this. Five spectra were simulated at 1500 K with each transition randomly assigned a Lorentzian width in the range 0.2-2 cm^{-1}. These spectra were then smoothed with a Gaussian filter that varied from no filtering to 15 cm^{-1} FWHM and fit to simulations smoothed to the same values. Major variation in the temperature results occur at low filtering widths and this variation didn't appear to have a repeatable pattern. At a FWHM value of about 6 cm^{-1} and above all curves begin to converge to the correct answer. An example of one of these spectra with the random broadening is given in Figure 3.32 with the large changes in absorption due to broadening variation easily visible.

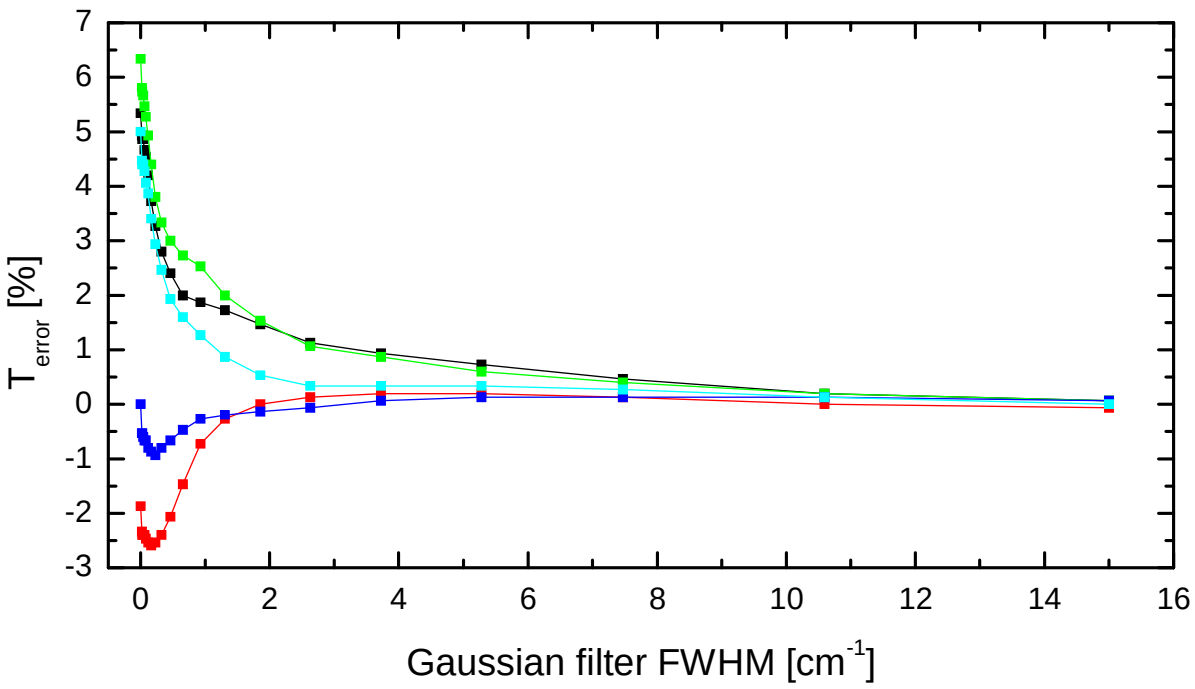

Figure 3.31 Temperature fitting results versus smoothing for 5 different spectra prescribed with random broadening in the range 0.2-2 cm^{-1} and simulated at 1500 K. By measuring the whole spectrum, it is still possible to infer accurate temperatures when the spectral line broadening characteristics are unknown.

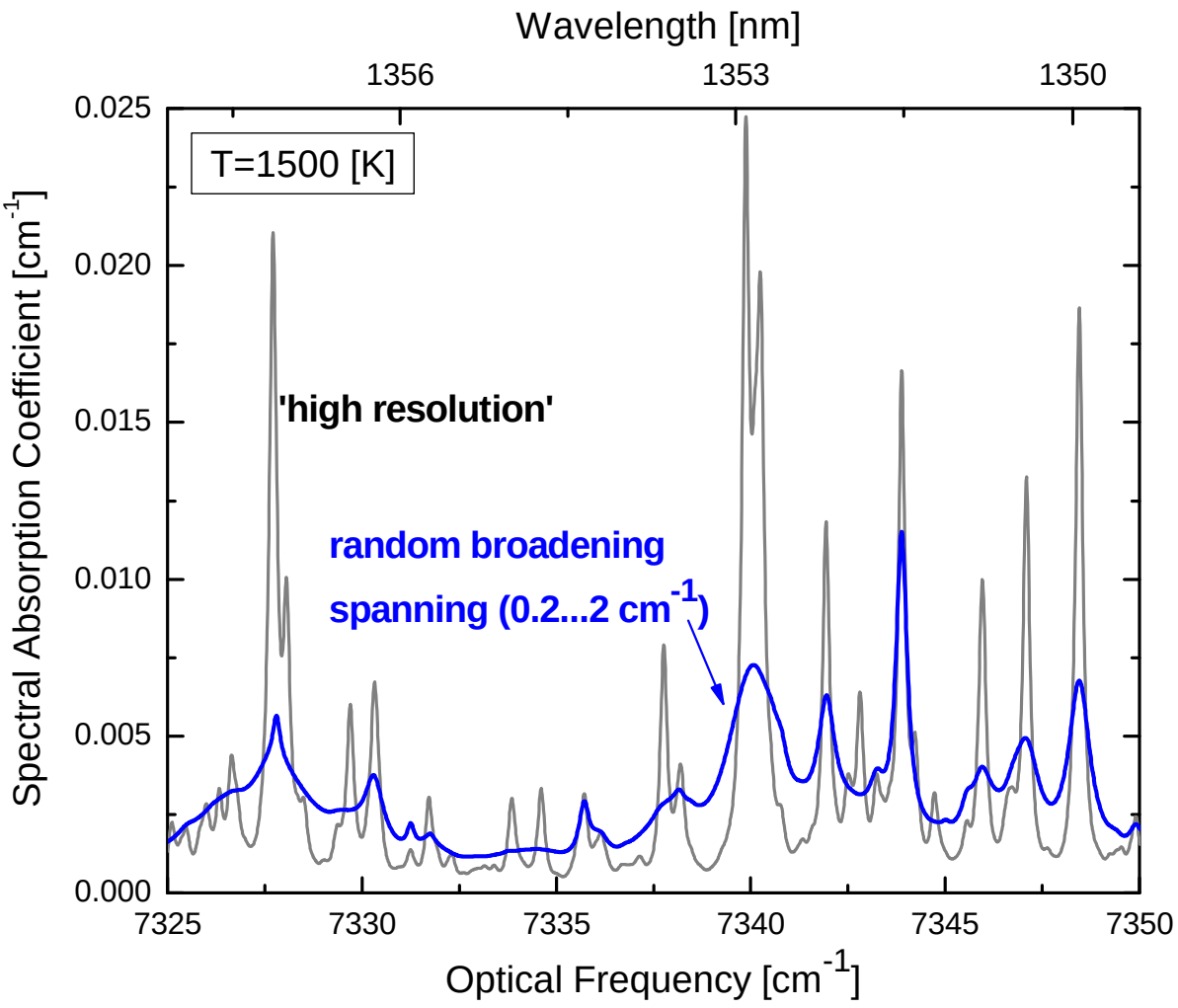

Figure 3.32 Spectra showing the difference between constant, low (0.2 cm^{-1}) broadening and one with variable, random broadening in the range 0.2-2 cm^{-1}. Even with the large difference in the lineshape function, the temperature information is retained when measuring the whole spectrum. The width of a scan required is dependent on the uncertainty in broadening and shown in this figure is a subset of the whole spectrum considered for inferring the temperature.

CHAPTER 4. APPLICATIONS

This chapter highlights measurements made in practical combustors. All three applications share the common theme of using H_2O absorption for performing simultaneous temperature and mole fraction measurements. However, each measurement campaign has its own flavor and highlights measurements made under differing conditions and using different laser sources. For instance, the first application in an internal combustion engine utilizes a fast, broad wavelength scanning laser capable of producing spectra at 100 kHz. The second application gives an example of measuring temperature using a laser that outputs discrete wavelengths chosen to align with features in order to optimize H_2O absorption thermometry. Both of these first two cases consider a gas path that is assumed uniform in temperature and species concentration and both highlight measurements in the R branch of the $\nu_1+\nu_3$ band of H_2O. The difference between the two is the internal combustion engine example uses a continuous wavelength scan and the gas turbine gives an example of using discrete wavelengths. The final application highlights an example of a measurement in the plume of a rocket motor. The flow field for this measurement can not be assumed to be uniform in temperature or H_2O concentration so a simple method of 1D axis-symmetric tomography is presented.

4.1 HCCI ENGINE

Optical studies of combustion in homogeneous charge compression ignition (HCCI) internal combustion (IC) engines have been vast and varied. Many different techniques have been

applied for measuring in-cylinder gas properties with temperature being a heavily sought after parameter owing to the fundamental role it plays in governing the chemical kinetics.

Many optical diagnostics currently used for in-cylinder measurements in internal combustion (IC) engine research, such as planar laser-induced fluorescence (PLIF), laser-induced incandescence (LII), and coherent anti-stokes Raman spectroscopy (CARS), can provide instantaneous two-dimensional images of in-cylinder properties but do not provide a continuous, crank-angle-resolved record of these quantities and thus can be susceptible to cycle-to-cycle variation [50-52]. Concomitant diagnostics such as exhaust gas analysis provide continuous, time-resolved gas composition and temperature of the combustion products but are decoupled from the instantaneous in-cylinder dynamics. Laser based line-of-sight absorption sensors offer promise of highly accurate, non-intrusive measurements of crank angle resolved in-cylinder temperature and gas composition. Coupled with spatially resolved techniques such as PLIF or multi-beam absorption strategies, these sensors can provide valuable insight into the combustion process and aid in advancing complex engine simulation codes.

Line-of-sight techniques, such as absorption spectroscopy, can be well suited for HCCI studies since the gas properties can be assumed uniform across the diameter of the cylinder making highly quantitative measurements possible. Three previous sensors based on line-of-sight absorption of water vapor to measure time-resolved, in-cylinder temperature for internal combustion engine applications have been developed. Mattison et.al. reported the development of a wavelength-multiplexed (WM), direct absorption sensor to monitor peak absorption of carefully chosen lines to maximize temperature sensitivity over the range of

temperatures imposed in the engine [21]. The sensor fiber couples individual laser diodes for providing the multiple colors and a grating is used for demuxing the separate colors onto multiple detectors. While this is a logical strategy for employing multi-color thermometry, adding more colors can be cumbersome and the spectral separation of additional wavelengths is limited by the resolution of the dumuxing grating.

Riecker et.al. employed an alternative system utilizing wavelength-modulation spectroscopy with 2f detection (WMS-2f) [43]. This technique increases the sensitivity enabling short path measurements, but has limitations compared to standard direct absorption spectroscopy. The system relies on expensive, complex electronics to generate the laser modulation and for demodulation of the output signal. By using the 1f signal to normalize the 2f signal, they have shown it is possible to account for laser fluctuations reducing the noise of the measurement but due to the frequency multiplexing of the individual laser sources, this approach is restricted to the simultaneous use of a limited number of laser wavelengths, thus reducing the temperature-sensing range to pre-combustion regimes.

Finally, Kranendonk et.al. reported the development of a wavelength-agile system based on the Fourier Domain Mode Locked (FDML) laser that was capable of tuning over the 1330-1380 nm range at a repetition rate of 200 kHz [4,53]. That sensor was similar to the WM sensor in that it directly measured the absorption but did so by means of a widely spanning wavelength sweep. Those results showed the ability to measure temperature at a RMS precision of 3% at 1500 K at a measurement bandwidth of 200 kHz.

The sensor described in this work using the FDML laser is able to provide temperature and H_2O mole fraction results at 100 kHz bandwidth over the entire power cycle (-90 to 90 CA

deg aTDC) for engine speeds ranging from 600–3000 rpm while achieving a RMS error in temperature of 0.25% at 1970 K.

4.1.1 Sensor theory

Absorption spectroscopy is an attractive technique for in-cylinder thermometry studies owing to its high signal-to-noise ratios allowing for measurement rates capable of resolving gas properties at sub crank angle resolution. It also is an absolute measurement technique eliminating the need for reference samples or calibration of the sensor to the particular application. The choice of H_2O vapor as the interrogation species is logical because it is a product of hydrocarbon combustion while also being present before the chemical reaction allowing for continuous measurements to be performed over the entire operating cycle of the engine. H_2O also has the added benefit of having absorption transitions within the telecommunication wavelength range where commercially developed light sources and components can simplify the task of building custom lasers.

In this particular study, the R branch of the $\nu_1+\nu_3$ vibrational band of water was chosen as the primary spectral target (~7300-7500 cm^{-1}). Along with the fundamental and hot bands of this combination band, the $2\nu_1$ overtone band also has appreciable absorption strength in this spectral range especially at elevated temperatures. The combination of rich spectral content spanning many different lower state energy levels makes this particular spectral range attractive for high speed gas thermometry (i.e. the wavelength requirements of the laser are reduced as compared to those needed for measuring the neighboring P branch where the line spacing increases as the wavelength deviates further from the band center).

4.1.2 Noise considerations

When measuring high bandwidth spectra, all possible noise sources must be carefully considered and addressed in order to achieve the best possible results. In addition to the usual sources such as laser intensity noise, shot noise, detector and digitizer noise, an often unconsidered noise, known as thermal beating noise or polychromatic beating noise, is extremely important in multi-mode operation of FDML lasers. If not managed carefully, this noise can severely limit the overall precision of the sensor.

At the output of the detector, thermal beating noise looks just like laser intensity noise although the physics are different. Thus the same strategies used for laser intensity noise are used to combat thermal beating noise, namely referencing. Here a very high-fidelity form of referencing is chosen, pulse delay referencing.

One possible means of reducing or even eliminating this noise is to use a perfectly single mode source. The FDML can be operated in a single mode fashion but in practice this mode of operation is limited in spectral coverage and overall stability of the source [53]. Another strategy is to use precise referencing of the light source in order to minimize the effects of thermal beating noise through the use of a ratiometric measurement [54,55].

The fundamental equation governing experimental absorption spectroscopy is the Beer-Lambert law which states that the fractional transmission of light through an absorbing medium can be exponentially related to the absorbance.

$$\frac{I}{Io} = e^{-k_{\nu}L} \tag{5.1}$$

Using this relationship to obtain the spectral absorbance coefficient, k_v, naturally leads to measuring the transmitted intensity, I, and the reference intensity Io and taking a ratio. If the measurement of I and Io is performed in way such that the polychromatic beating noise is sampled identically, then this noise will cancel thus motivating the use of pulse delay referencing.

4.1.3 Experimental arrangement

An overview of the experimental arrangement can be viewed in Figure 4.1. To facilitate the broad, fast wavelength scans, the FDML laser was used in this work and was described in detail elsewhere [4,53,56]. The laser was setup to provide wavelength scans from 1333 – 1377 nm, enforced by the electronics driving the fiber Fabry-Perot tunable filter (FFP-TF). To control and monitor the wavelength sweep, two fiber Bragg gratings were used as markers to indicate both endpoints of the sweep.

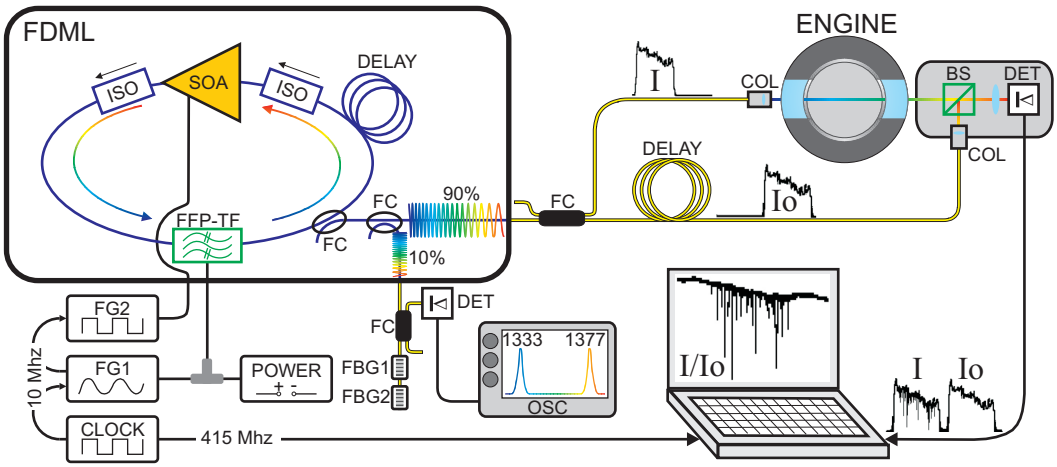

Figure 4.1 The experimental arrangement. Shown at the top left is a schematic of the Fourier Domain Mode Locked (FDML) laser used in this work. The cavity consists of a semiconductor optical amplifier (SOA), two optical isolators (ISO), a fiber delay (DELAY), a fiber Fabry-Perot tunable filter (FFP-TF), and a fiber output coupler (FC). In addition the timing and control electronics (FG1, FG2, and CLOCK) are shown along with the wavelength control scheme based on two fiber Bragg gratings (FBG1) and (FBG2). The light coupled out of laser towards the test article (ENGINE) is split into two legs (I) and (Io) with the Io leg time delayed by use of a delay fiber (DELAY). Upon exiting the engine, the I leg is incident on the detector (DET) immediately followed by the Io leg incident on the same detector by means of a beam splitting cube (BS) with the output voltage of the detector recorded as a function of time.

In order to minimize the experimental noise, a special detection scheme was used that permits low noise measurements of multi-mode light sources used in high speed measurements. The output light of the FDML is first split via a fiber coupler with one leg (I) sent to the engine and the other leg (Io) sent through a long length of fiber that acts as a time delay. The delay fiber is sized such that a single sweep of the FDML is delayed by exactly half the period of the laser scan time. This delayed sweep is then recombined onto the same detector as the engine sweep. In the end, the same pulse of light is measured twice on the same detector: one pulse that has acquired absorption information upon transmission through

the engine, the other reference pulse which has only been delayed. Upon taking the ratio of these two signals, I/Io, the common mode noise of the two beams cancel almost entirely permitting low (nearly shot noised limited) measurements of the absorbance.

The performance of this cancellation technique is typically limited by timing precision. Therefore a master clock is used to synchronize the laser to the data acquisition system. For this work, a Stanford Research Systems CG635 with an oven controlled crystal oscillator was used as the master timebase. This master clock was phase lock looped to the function generators driving the laser and also used as the digital edges for the data acquisition's analog to digital converter. The sample rate of the ADC was chosen as an integer multiple of the laser sweep frequency so that consecutive laser sweeps would be sampled at the same points in time thus making post processing simpler for multiple laser scans.

The engine used in these tests was a Honda single cylinder test engine designed with two large windows for optical access. The engine was run in HCCI mode with n-heptane as the fuel. HCCI is an engine operating mode in which an approximately homogeneous fuel and air mixture is compressed with the combustion controlled entirely by the chemical kinetics. Since there are no propagating flame fronts in this operating mode (the combustion is ubiquitous) and the mixtures are otherwise homogeneous in concentration and temperature; line-of-sight (LOS) techniques, such as absorption spectroscopy, are well suited for inferring the gas properties.

An important design parameter of the system was the ability to capture and record data over many consecutive cycles of the engine. More specifically, the data acquisition system was to be able to capture at a minimum, 100 consecutive engine cycles consisting of data from -90

to +90 crank angle degrees aTDC for engine speeds over the range of 600 to 3000 rpm. The FDML's repetition rate in this experiment was 99.92 kHz so a sample rate of the order of 100s of MS/s is necessary to resolve the spectral features at early and late engine cycle conditions (e.g. low pressure). To accomplish the long record lengths and fast sampling rate, a PC data acquisition board (Gage CompuScope 12400) was used. Through the use of an external clock, this board allowed sample rates of up to 420 MS/s when using a single channel over an analog bandwidth of 200 MHz. The actual sample rate used was 415.56292 MS/s corresponding to an integer multiple of 4201 times the laser repetition rate. This board was also equipped with a high memory option (2 GBytes) which enabled the entire measurement to be stored onboard allowing for the slower transfer to hard disk to occur after the measurement was completed. Along with the high-speed optical data, the engine crank angle encoder and in-cylinder pressure was acquired on the same PC with a National Instruments 6132 analog input board. This two-channel DAQ board was clocked with the sync pulse of the function generator driving the laser thus guaranteeing the samples to be acquired with each scan of the laser at 98.2 kHz.

4.1.4 Results

For each laser scan, 4 data points were produced with this system: gas temperature, H_2O mole fraction, gas pressure, and crank angle timing. The pressure was obtained by converting the voltage output of a piezoelectric transducer to pressure by means of a known calibration. The crank angle encoder had ¼ crank angle resolution, allowing each spectrum to be given an accurate crank angle position through linear interpolation. For an engine running at 600

rev/min, the 99.92 kHz laser repetition rate corresponded to approximately 28 lasers scans per crank angle.

The temperature and H_2O mole fraction were inferred through means similar to a previously described recipe [28] with a few key differences. Instead of using the HITRAN [22] or HITEMP [24] database for the spectral simulation parameters for water, the BT2 [23] spectral line list was used. Also, to overcome variations in the baseline of absorbance spectra, an automatic baseline correction routine was used instead of differentiation [28].

Results for a single cycle can be seen in Figure 4.2. Plotted in this figure is the pressure, temperature, and H_2O mole fraction versus crank angle. The temperature results gave a precision of 5 K or 0.25% near top dead center where the temperature and pressure conditions were at a maximum resulting in the best precision to date for engine thermometry in an IC engine.

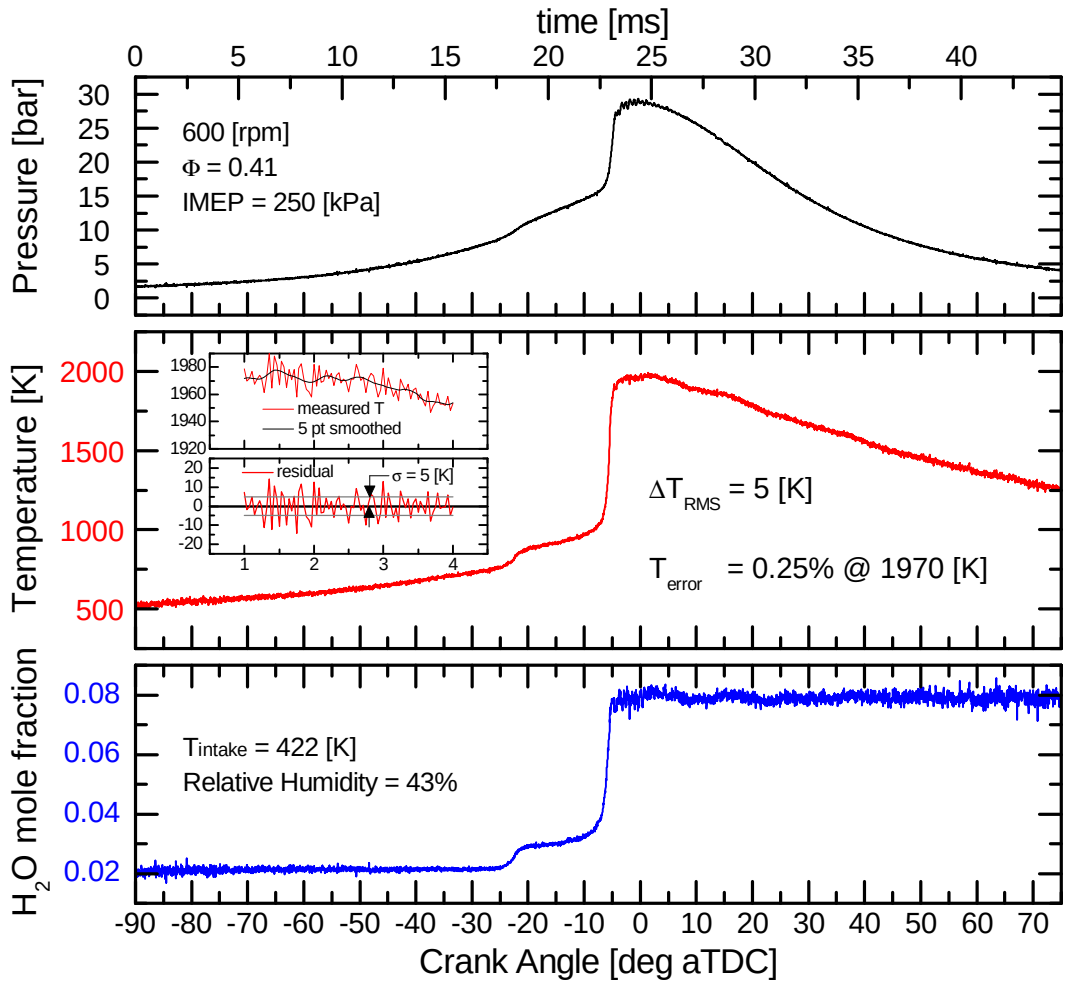

Figure 4.2 Temperature and H_2O mole fraction of a single cycle of the engine inferred from the measured spectra at 100 kHz (10 us per data point, ~ 28 points per crank angle degree) showing a 5 K RMS error in temperature near top dead center (0.25% precision error at a temperature of 1970 K). Also shown is the pressure measured using a piezoelectric transducer

In the top panel of Figure 4.3 TOP PANEL: Measured spectrum at 1.036 CA deg aTDC and the best fit simulated spectrum at the inferred temperature of 2237 K using the constant broadening assumption. BOTTOM PANEL: Residual (measured – simulated) of the two spectra showing the preferentially downward peaks at lower wavenumber and upward peaks at higher wavenumber resulting from the constant collisional broadening assumption. When

variable collisional broadening is assumed, preferential features are less evident, indicating a better fit., a single measured spectrum recorded at 1 deg aTDC is compared to a simulated spectrum and good agreement is obtained. This simulated spectrum is based on the inferred “variable” broadening of the blended spectral features. In the bottom panel of this figure, the residual between the two spectra are plotted and the slight variations become more evident. Two different residuals plotted; one based on a constant collisional broadening assumption for the H_2O spectrum and another utilizing a variable broadening method used within the spectral fitting routine. Marked improvement (reduced discrepancies in the residual) is visible for the variable broadening case and this corresponds to improved temperature and mole fraction results.

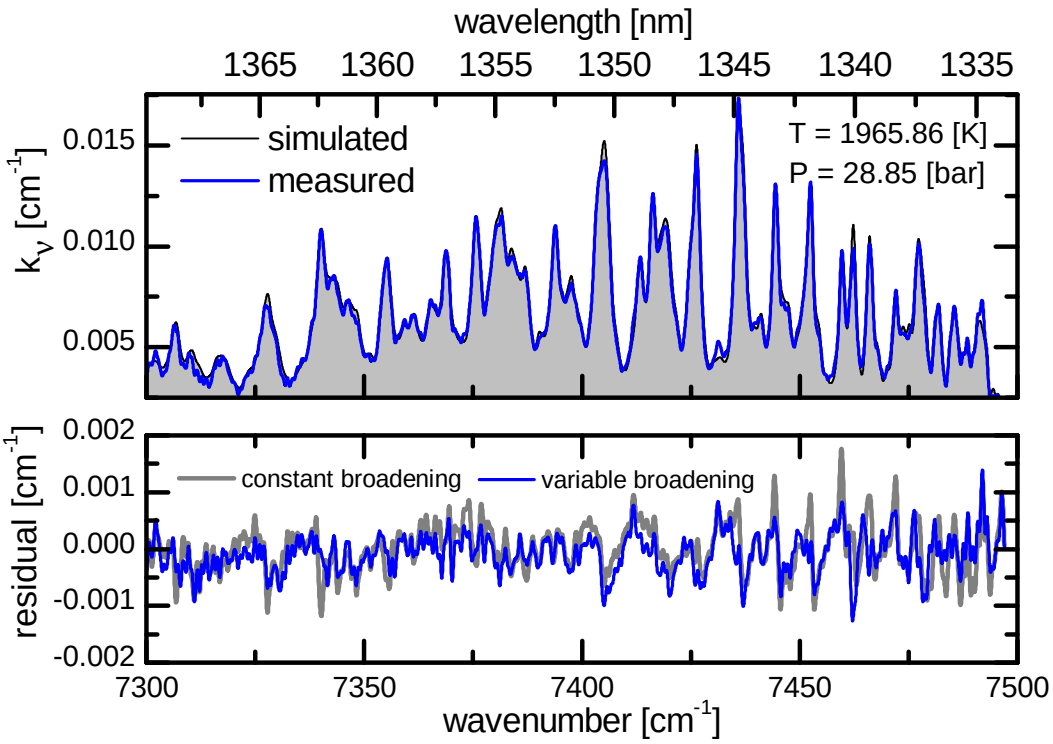

Figure 4.3 TOP PANEL: Measured spectrum at 1.036 CA deg aTDC and the best fit simulated spectrum at the inferred temperature of 2237 K using the constant broadening assumption. BOTTOM PANEL: Residual (measured – simulated) of the two spectra showing the preferentially downward peaks at lower wavenumber and upward peaks at higher wavenumber resulting from the constant collisional broadening assumption. When variable collisional broadening is assumed, preferential features are less evident, indicating a better fit.

The BT2 database does not include line shape parameters for simulating the water spectrum. At conditions typical of an IC engine, pressure broadening dominates the spectral line widths and the effect is not constant across the broad wavelength scan obtained with a scanning laser such as the FDML; especially at high temperature and pressure. Applying the fitting routine used in this study with the constant broadening assumption results in a best fit simulation that has visible errors evident by the preferential downward peaks in the residual at lower wavenumber and upward peaks at high wavenumber. To overcome this limitation, a more

advanced fitting routine is used that allows for variable collisional line widths to be used in the fitting. Instead of fitting to a database of spectra that only varies in temperature, a database is constructed that consists of spectra at different line widths. The simulation is carried out by specifying the line width and then simulating spectra over a prescribed temperature vector and then repeating for N different line widths. Once this larger database is constructed, the actual fitting routine is as follows:

1. Guess a broadening and find the best fit spectra based on the minimum MSE to find an initial temperature
2. At this initial temperature, repeat the fit over all the broadening values in the database to find the best fit constant broadening value
3. Apply a wavelength warping scheme between the experimental spectrum and a simulation at the current best fit temperature and constant broadening to account for minor database line position errors and/or experimental wavelength errors
4. Divide the spectrum into discrete zones and fit each zone at the current temperature to a best fit broadening value
5. Perform a final least squares fit between the measured spectrum and simulated spectra with the simulated spectra consisting of the zones of best fit broadening coefficients to find the final best fit temperature and mole fraction

The result of applying this more advanced fitting routine is the ability to capture non uniform line widths in the measured spectrum and thus more accurate values for temperature and H_2O mole fraction. The first indicator of the improvement through the use of this routine is the residual between the measured and simulated spectrum no longer contains a visible pattern but better represents the inherent noise in the measured spectrum. Also, the temperature and

mole fraction results have a significant difference, especially at elevated temperatures and pressures, as can be seen in Figure 4.4 with the most significant difference being visible in the resulting mole fractions. The mole fraction for the constant broadening case shows significant slope in the pre and post combustion states. This variation is difficult to explain physically and is most likely not representative of the actual mole fraction of the gas mixture.

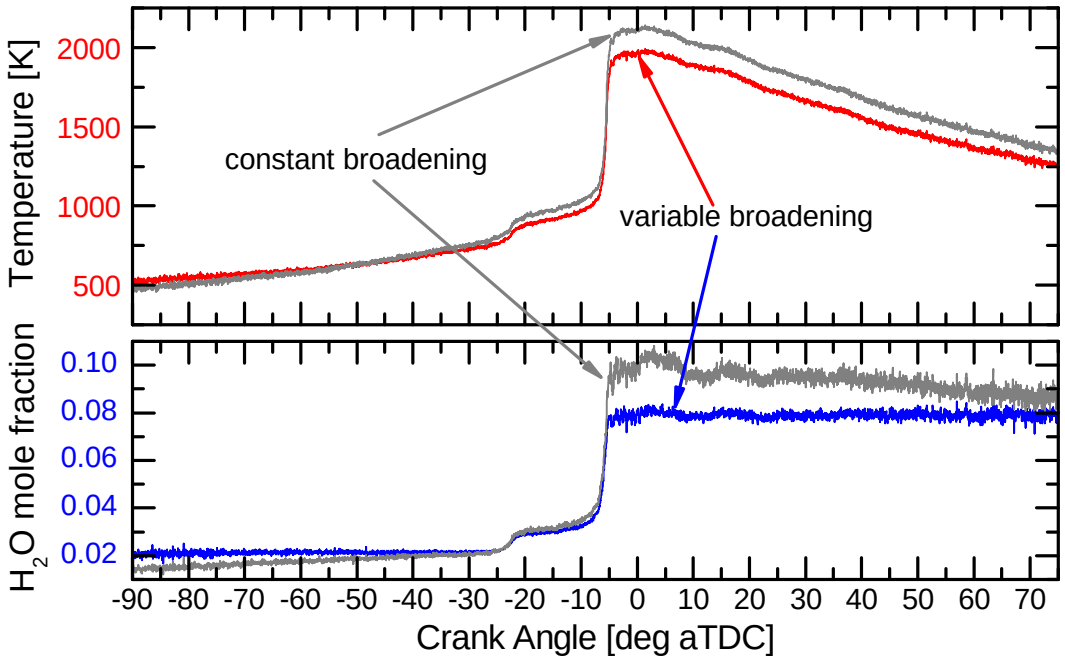

Figure 4.4 Difference in temperature and H2O mole fraction results when fitting to simulations using constant and variable broadening. The variable broadening scheme led to better agreement based on the mean square error of the difference between the measured spectrum and the simulated spectrum at the best fit temperature. Furthermore, the otherwise unexplainable slopes in the H_2O mole fraction curve for the constant broadening case pre and post combustion is not present when including variable broadening.

Even further confidence is gained when comparing the results of this sensor against a computational fluid dynamics (CFD) simulation using the KIVA code utilizing the PRF mechanism as shown in Figure 4.5[57,58]. The temperature result from the simulation was averaged along the line of sight path the laser traversed and good agreement is found between the two.

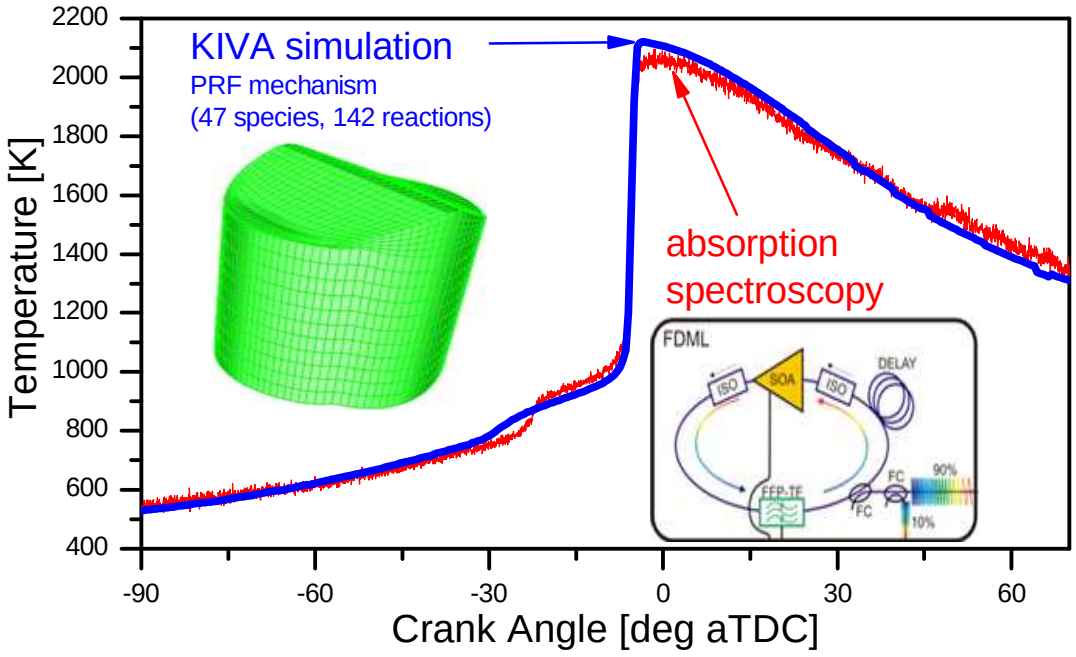

Figure 4.5 Comparison of temperature results between the absorption spectroscopy experiment and simulation based on the KIVA CFD code. The fully 3D results of the simulation were averaged along the same path the laser beam traversed and good agreement is found between the two.

4.1.5 Discussion

The present thermometry capabilities presented here are 100 kHz temperature rates at 0.25 % precision near top dead center. Other H_2O based absorption measurements have been performed in IC engines but have been limited in cycle crank angle coverage or speed. For example, Kranendonk et.al. performed a similar measurement in a HCCI engine while also

using the FDML laser as the light source [4]. For that measurement, the RMS precision of a single cycle measurement was approximately 3% near TDC in the high pressure, high concentration region, and significantly worse before -30 CAD because of low H2O content. In that experiment, pulse delay referencing was not used nor was the acquisition timing linked to the laser control electronics so consecutive triggering was used for the acquisition. This limited the overall measurement rate to a single spectra or temperature for every 0.25 crank angle or 14.4 kHz.

Kranendonk et.al. also applied the FDML to an HCCI engine under motoring conditions and for this experiment applied the pulse delay referencing strategy [53]. Due to limitations in the optical engine used, firing operation was not possible for this work. Despite the low noise in individual spectra, calculated single-shot temperatures were plagued by problems associated with trigger jitter. A consecutive triggering acquisition was again used in this work. There was at least one sample of jitter associated with the triggering and at the sample rate of 100 MS/s (10 ns per sample), this corresponds to a jitter of ~0.1 nm in the wavelength axis. As temperatures inferred from the water spectrum are sensitive to the accuracy of the wavelength axis, this jitter created a significant jitter in the temperature results by only obtaining ~5 % RMS precision for single laser scans or ~1% when averaging scans over one crank angle.

4.1.6 Conclusions

The measurement presented here represents the current state of the art in high speed engine thermometry using optical absorption techniques. A temperature precision of 0.25 % RMS has been reported near TDC in the high temperature and pressure conditions of an HCCI

engine. Through the use of a fast, broadly tunable FDML laser, many consecutive engine cycles were captured and available for studying the transient nature of the engine. Phenomena such as engine cycle-to-cycle variations are readily available for study and possibly more important is the potential for complex CFD model validation. Perhaps the more interesting application of this and similar laser sources is expanding the usefulness of this line-of-sight technique to non-uniform flow fields through tomographic inversions [11].

4.2 GAS TURBINE COMBUSTOR

Two time-division multiplexed (TDM) sources based on fiber Bragg gratings were applied to monitor gas temperature, H_2O mole fraction, and CH_4 mole fraction using line-of-sight absorption spectroscopy in a practical high-pressure gas turbine combustor test article. Collectively, the two sources cycle through 14 wavelengths in the 1329 -1667 nm range every 33 μs. Although it is based on absorption spectroscopy, this sensing technology is fundamentally different from typical diode laser-based absorption sensors and has many advantages. Specifically, the TDM lasers allow efficient, flexible acquisition of discrete-wavelength information over a wide spectral range at very high speeds (typically 30 kHz) and thereby provide a multiplicity of precise data at high speeds. For the present gas turbine application, the TDM source wavelengths were chosen using simulated temperature-difference spectra in manner similar to that outlined in section 3.5.2. This approach is used to efficiently select TDM wavelengths that are near the optimum values for precise temperature and species concentration measurements. The application of TDM lasers for other measurements in high-pressure, turbulent reacting flows and for 2D tomographic reconstruction of the temperature and species concentration fields is also forecast.

Tunable diode-laser-based absorption spectroscopy is the most widely used method for measuring gas-phase temperature and species concentrations in reacting flows [59]. Although path-averaged in nature, such absorption measurements can in principle capture combustor instabilities and large-scale transients such as ignition and global extinction provided that a high-speed tunable laser source is available. Traditionally, high-speed multispectral sensing in combustion has been performed using tunable diode lasers, for example two scanning diode lasers [60,61] or five tunable diode lasers operated at fixed wavelength [62] for measuring combustion parameters such as temperature, species concentration, and soot volume fraction. It can be summarized that in the past, the sensor development process even in telecommunications bands, depended on the cost and availability of laser sources; typical sensor design decisions were not based on obtaining the most desirable spectral information, but rather on optimizing sensor performance using available wavelengths.

A hyperspectral source, like the TDM source, is a source that rapidly sweeps or cycles through many wavelengths. Typical spectral acquisition rates for such sources are in the range of 1-100 spectral resolution elements / μs. Although traditional semiconductor sources, most notably vertical-cavity surface-emitting lasers (VCSELs), can be hyperspectral in nature, many new sources have recently been developed, including fiber [53,56,63-65] and free-space [66,67] designs. Hyperspectral sources allow one to rapidly record spectral information using only a single-element photoreceiver such as a photodiode. Hyperspectral sources can often be easily tailored to operate over a wide range of target wavelengths to achieve a given measurement goal. These sources are allowing researchers to custom-build light sources to specifically address a particular problem instead of designing sensors based on the availability of light sources in the marketplace.

Currently available hyperspectral sources can be characterized as shown in Table 4.1. ‘Continuous-spectral’ refers to sources such as swept-wavelength lasers that can be used to acquire contiguous spectral information, composed of numerous adjacent spectral resolution elements. Typically sources in the continuous-spectral class span a broad wavelength range (>100 cm^{-1}). Examples include femtosecond-laser comb-Fourier transform spectroscopy [67,68], continuous-wave comb-Fourier transform spectroscopy [69] and Fourier-domain mode-locked (FDML) lasers [53,56].

Table 4.1 Classification matrix for modern hyperspectral sources.

<table>
<tr><th></th><th colspan="2">frequency domain</th><th>time domain</th></tr>
<tr><td rowspan="2">continuous-spectral</td><td rowspan="2">comb</td><td>fs</td><td rowspan="2">FDML</td></tr>
<tr><td>CW</td></tr>
<tr><td>discrete-spectral</td><td colspan="2">FDM</td><td>TDM</td></tr>
</table>

Although its name might imply otherwise, the FDML source falls in the ‘time domain’ column because it is simply a swept-wavelength laser (spectra are encoded in time as the laser sweeps). The comb sources fall in the ‘frequency domain’ column because the spectra are encoded in frequency (final spectral results are obtained by Fourier-transforming the measured signals). ‘Discrete-spectral’ refers to sources that acquire nonadjacent spectral resolution elements. Typically these sources are composed of multiplexed monochromatic lasers, each aligned to a molecular feature such as an absorption maximum. Examples include frequency-division multiplexed lasers [64] and the time-division multiplexed (TDM) laser used in this work.

For this application, the main objectives were to (1) measure the time it takes gases within a high-pressure combustor to experience a significant temperature rise following a fuel valve opening command and (2) to measure H_2O and CH_4 concentrations along with gas temperatures to enhance the understanding of the overall performance of the combustor. These requirements dictate that the sensor system must have ~ 100 µs time response in addition to the ability to perform over the 500-2500 K temperature range and the 3-30 bar pressure range.

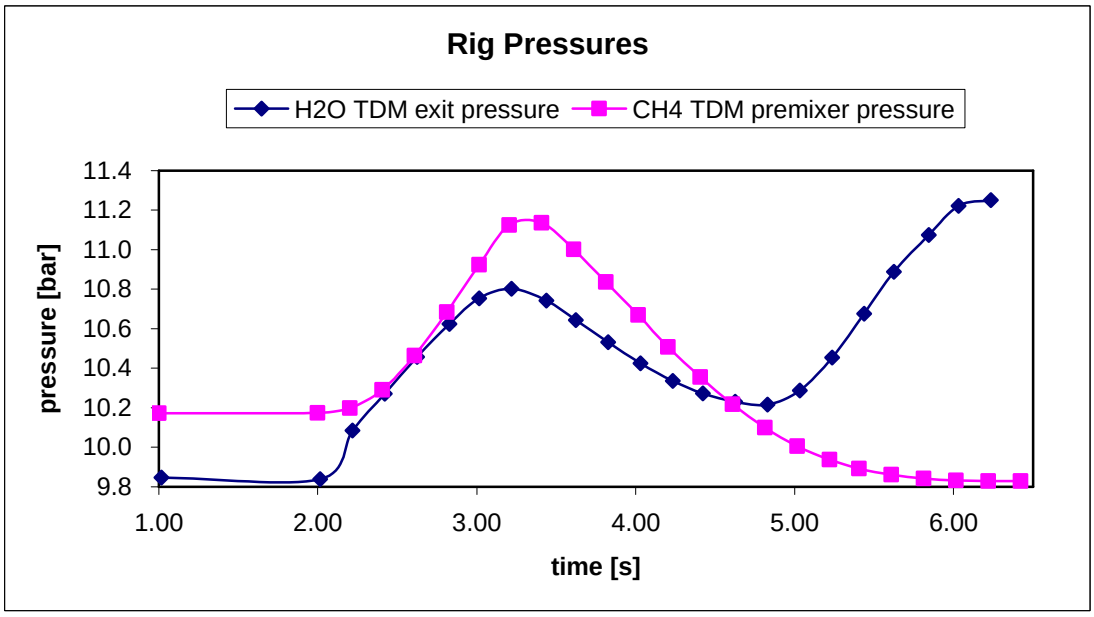

Figure 4.6 Measured pressures in the combustor test rig near the H_2O and CH_4 beam paths

For the measurements in the high-pressure combustor, the TDM laser system based on time-division multiplexing (TDM) was chosen because of the following reasons:

a) simple design due to the less stringent requirements on the laser linewidth at high-pressure, typically 3 GHz or less [70]

b) many discrete wavelengths can be incorporated within the gain bandwidth of the optical amplifier thus allowing sensitive thermometry over a broad temperature range along with access to multiple species.

c) straightforward signal detection at numerous wavelengths with only a single detector, since each wavelength is monitored at a unique time.

The TDM laser used in this work could be distributed to many laser beam paths to enable two-dimensional tomographic reconstruction of gas properties. This TDM source is ideally suited for high-speed tomography since each line-of-sight efficiently provides absorption data at multiple wavelengths, thereby increasing the number of known data points for tomographic reconstruction of gas properties. In tomography, the number of unknown variables (for example, temperatures and H_2O concentrations at numerous grid points) one can extract typically depend on the amount of available information [11,12]. This work represents the first application of the recently-developed TDM source in a practical environment: a high-pressure gas turbine combustor test article. The source was successful in this environment, but because of the constraints associated with the test (few combustor tests with limited time to troubleshoot), the results do not match the quality of recent in-cylinder thermometry work using swept-wavelength sources [53,71,72]. However, it is important to note that fundamentally, TDM approaches outperform swept-wavelength approaches owing to dedication of increased integration time on the most important spectral features.

4.2.1 Spectral selection and management

H_2O wavelength selection for thermometry

The recently-developed TDM laser allows access to essentially arbitrary wavelengths throughout a ~300 cm^{-1} bandwidth [70]. For example, the TDM source can multiplex many wavelengths (up to 100 or perhaps 1000) in a single laser cavity, thereby dramatically enhancing the prospect of simultaneous detection of multiple species with one sensor system. The source can also be easily reconfigured or tailored to the particular measurement of interest. This flexibility in spectral output allows selection of wavelengths based on particular need. For the current work, wavelengths are chosen to provide good temperature sensitivity over a wide range of temperatures (nominally 500-2500K) and pressures (nominally 3-30 bar). In low-pressure H_2O absorption spectroscopy, one generally attempts to achieve high temperature sensitivity by monitoring the absorption resulting from transitions with various lower-state energies. At high pressure where spectral overlap between adjacent transitions is common, the 'feature-aggregate' lower-state energies can be considered to utilize line-selection strategies common in low-pressure spectroscopy. A similar analysis is used here to guide the wavelength selection for this work with an emphasis on temperature difference spectra as shown in Figure 4.7. These spectra are generated by simply subtracting the spectral absorption coefficient, k_ν, at T_2 from k_ν at T_1. Portions of the difference spectrum that are positive are collectively called "hot" features since the absorption is stronger at higher temperatures; conversely, portions that exhibit negative values are denoted as "cold" features. The difference spectra roughly approximate the derivative of the spectrum with

respect to temperature, $\frac{\partial k_\nu}{\partial T}$, which is an important parameter for choosing wavelengths to maximize temperature sensitivity.

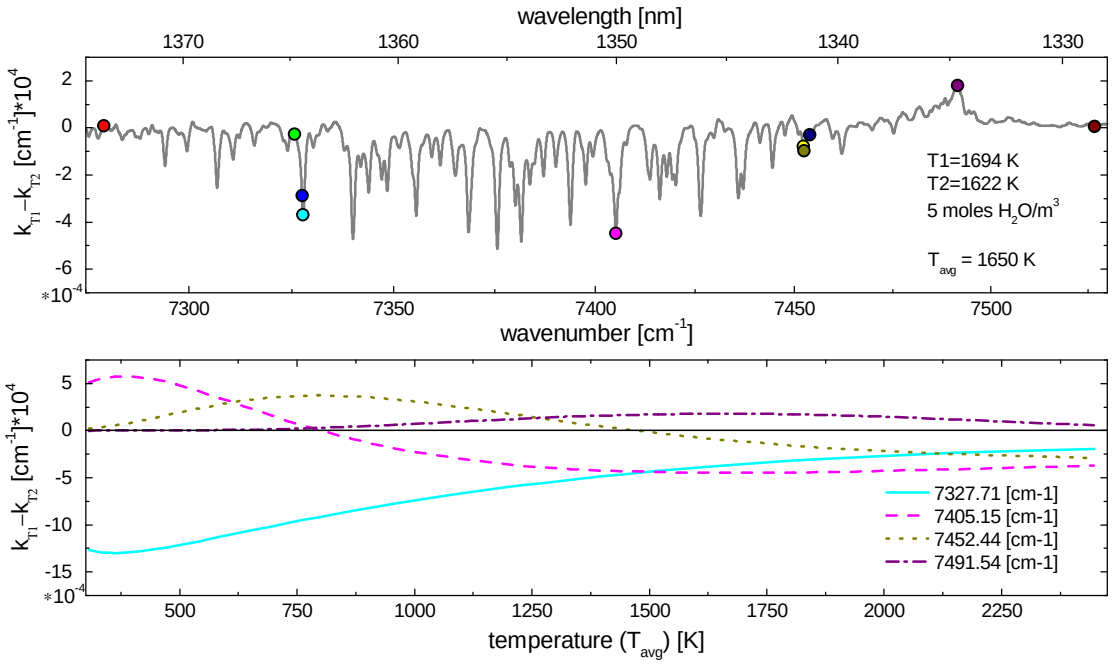

Figure 4.7 TOP PANEL: Sample difference spectrum used to guide wavelength selection for H2O absorption thermometry. Peaks represent features that exhibit increased absorption with increasing temperature, and valleys represent features that exhibit decreasing absorption with increasing temperature. Circles represent the design wavelengths for the H2O TDM source described herein. BOTTOM PANEL: values of difference spectra at four of the design wavelengths showing sensitivity versus temperature.

The top panel of Figure 4.7 shows the difference in absorbance for 1622K and 1694K. In order to achieve good temperature accuracy between 1622K and 1694K it would be natural to focus on the features at 7491 cm^{-1} (largest positive value) and 7405 cm^{-1} (largest negative value). Inclusion of these two channels in the TDM suite ensures that temperature-sensitive features are being measured at 1650 K, leading to the good temperature precision. In an

application where the temperature does not change appreciably from 1650 K, selection of these two wavelengths would be sufficient for precise temperature measurements under ideal conditions. However, in practical environments it is usually necessary to add one or more baseline monitoring wavelengths. These baseline wavelengths account for transmission losses from other than absorption by the target species; possible sources include beam steering, window fouling, unknown broadband absorbers, etc. In this work, two baseline wavelengths are used (one at each extreme of the measured spectral range) to allow correction of baseline effects with up to a linear dependence on optical frequency.

Aside from baseline correction, more wavelengths are also needed for precise measurements of test articles in which the gas conditions span large temperature ranges. The bottom panel in Figure 4.7 shows the value of the difference spectra at four wavelengths across a wide temperature range. These four temperature sensitive features (TSFs) were chosen to optimize the maximum difference in the difference spectrum at any two wavelengths for the wide range of temperatures considered. For example, at temperatures below 500 K the feature at 7327 cm^{-1} has the largest negative value and the feature at 7405 cm^{-1} has the largest positive value thus making this pair the best choice for maximizing sensitivity to temperature in this temperature range. As the temperature is increased, other wavelengths become important for satisfying this criterion of maximum difference. At temperatures above ~1300 K, there is only one feature in the wavelength range of interest that exhibits a positive value in the difference spectrum plot. This feature near 7491 cm^{-1} is at the band head of the R branch of the $\nu_1+\nu_3$ vibrational band where a large collection of lines with high lower state energies exist. Under conditions where collisional broadening dominates (pressures of ~1 bar and

greater), the collective nature of these narrowly spaced lines results in a feature that has appreciable absorption and makes it an excellent candidate as a choice for the “hot” feature at elevated temperatures. Thus, the 7491 cm^{-1} feature is almost always desirable, except, for example, in test articles that do not exceed ~ 800 K.

Along with these four TSFs and the previously mentioned baseline monitoring wavelengths, four other wavelengths were chosen to provide information related to the broadening of the spectral features. Similar to the temperature difference approach, broadening difference spectra were generated allowing the selection of wavelengths that would optimize the sensitivity to changes in the spectral width mainly due to changes in pressure. In order to fit the linewidth of a spectral feature, at least two points on that spectral feature are required. To reduce the number of additional broadening wavelengths required, these wavelengths were selected near previously chosen TSF wavelengths. To account for variability in the broadening across the spectrum, broadening wavelengths were chosen at two different TSFs. By measuring broadening wavelengths at two different TSFs, a linear relationship to predict the variation of broadening coefficients across the spectrum can be used. An approximately linear relationship between broadening coefficient and wavenumber has been previously observed in piston engine measurements in this spectral range [72]. Finally, to accommodate a wide range of pressures, two broadening wavelengths were added near each TSF with one close to the TSF wavelength for low pressure conditions and another further from line center for high pressure measurements. The 10 final wavelength selections for H_2O sensing are outlined below in Table 4.2.

Table 4.2 Wavelengths used in the H2O TDM laser system. Design and actual / measured wavelengths differ because of imperfect temperature control of the fiber Bragg gratings. Overall, ten wavelengths were chosen: 4 for monitoring peak absorbance of temperature-sensitive features, 4 for monitoring feature broadening (2 are best when the broadening is high and 2 are best when the broadening is low), and 2 for tracking baseline changes.

Design Wavelength [nm]	Measured[a] Wavelength [nm]	Description
1328.604	1328.593	bandhead baseline
1334.839	1334.826	high temperature temperature sensitive feature (TSF)
1341.587	1341.574	hi broadening on medium temperature TSF
1341.842	1341.825	medium temperature TSF
1341.884	1342.112	low broadening on medium temperature
1350.410	1350.397	dual temperature TSF
1364.682	1364.445	cold TSF
1364.724	1364.663	low broadening on cold TSF
1365.076	1365.038	high broadening on cold TSF
1373.749	1373.727	bandcenter baseline

[a]Wavelengths measured with an Agilent 86142B spectrum analyzer calibrated in this spectral range to the BT2 H_2O spectral database[23]

CH_4 wavelength selection

The $2\nu_3$ absorption band of CH_4 around 1666 nm is an attractive spectral region for sensing given its close proximity to standard telecommunications wavelengths. Figure 4.8 shows a simulated CH_4 absorption spectrum for representative conditions in this gas-turbine combustor test. The four wavelengths chosen for the fuel TDM measurement is shown in Figure 4.8. These wavelengths along with a description of their purpose can be found in Table 4.3. These wavelengths were again chosen by difference spectra to maximize sensitivity to both temperature and line broadening.

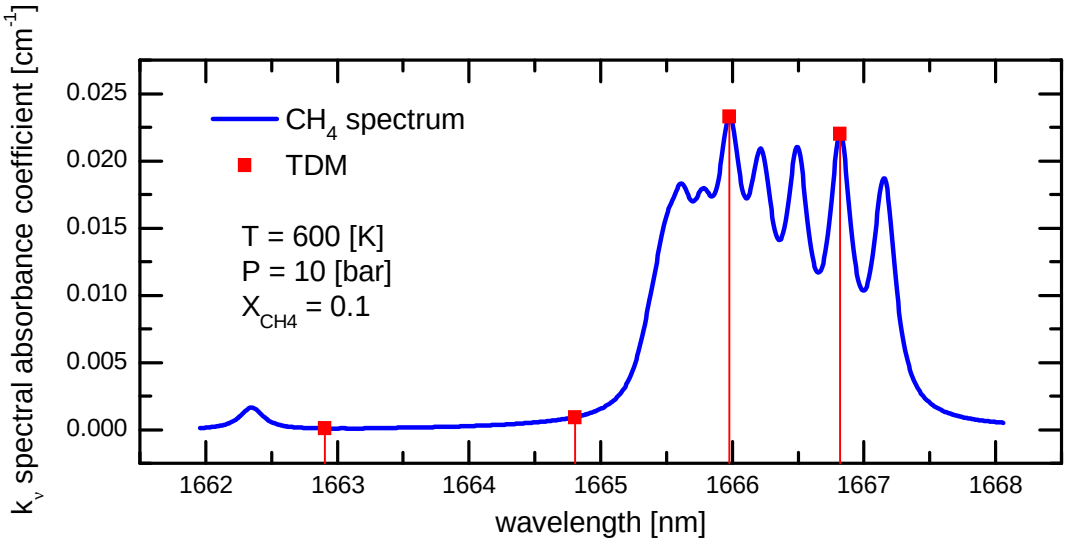

Figure 4.8: Simulated CH4 spectrum showing the four wavelengths chosen for the fuel TDM laser

The primary goal of this measurement was to monitor the fuel mole fraction. A single baseline wavelength was used to monitor non-absorptive transmission losses with the other three wavelengths monitoring features of spectroscopic relevance. The 1664 nm selection is highly sensitive to spectral line broadening and is mainly used for monitoring the effects of changes in gas pressure. The final two selections at 1665 nm and 1666 nm are useful for

inferring temperature near the nominal temperature of the experiment which was externally controlled to be at or near 600 K.

Table 4.3 TDM wavelengths used for the CH4 measurement. In total, 4 wavelengths were selected: 2 to monitor temperature-sensitive features, 1 for line broadening, and 1 for tracking baseline errors.

Design Wavelength [nm]	Measured[a] Wavelength [nm]	Description
1663.056	1662.906	Baseline (minimal absorption)
1665.142	1664.805	Pressure or broadening sensitive wavelength
1665.959	1665.858	Temperature sensitive feature
1666.630	1666.793	Temperature sensitive feature

[a]Wavelengths measured with an Agilent 86142B optical spectrum analyzer calibrated in this spectral range to the HITRAN 2004 CH_4 spectral database[22]

4.2.2 Experimental arrangement

Two separate TDM sources were deployed: the 1328 -1373 nm TDM source used to monitor the mole fraction and temperature of H_2O and the 1662.9 – 1666.7nm TDM source used to monitor the mole fraction and temperature of CH_4. Each source produced an 8.3 μs-duration color burst (composed of 10 wavelengths in the case of the H_2O source and composed of 4 wavelengths in the case of the CH_4 source) followed by a 25 μs dwell where no light was emitted, resulting in a source with a 25% duty cycle. Accordingly, the color burst was repeated every 33.3 μs, consistent with a 30 kHz measurement rate. Other signals can be time-multiplexed into the 25 μs dwell to achieve an effective duty cycle greater than 25%; in

this work, a delayed pulse referencing approach was used with both the H_2O and CH_4 sources to achieve 50% duty cycle for each source as shown in Figure 4.9 [53,55].

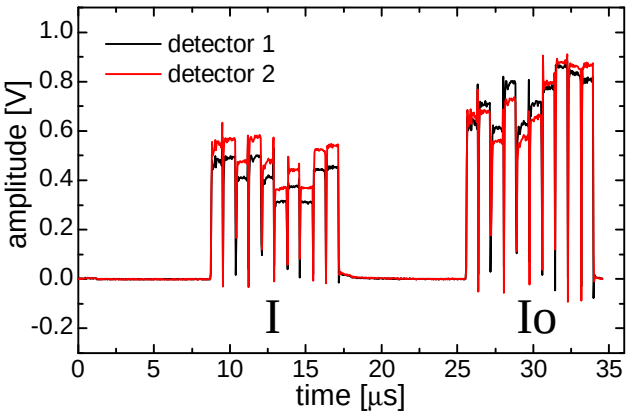

Figure 4.9: Raw single-cycle time trace of the 10-color H2O TDM laser utilizing pulse delay referencing

In this referencing approach, a replicate of each color burst was time-delayed in fiber and multiplexed back onto a single detector to permit precise measurements of reference intensities. It would be straightforward to multiplex both 50% duty cycle sources to yield a 100% duty cycle signal useful for combined measurements of H_2O and CH_4. However, CH_4 measurements were required in a different physical location from H_2O measurements, as shown in Figure 4.10: the former just downstream of the fuel injection to measure the unburned fuel-air mixture and the latter downstream of the combustion zone to monitor the H_2O vapor produced in combustion. Therefore, in this experiment, the light for both the H_2O and CH_4 sensors was not multiplexed into a single fiber.

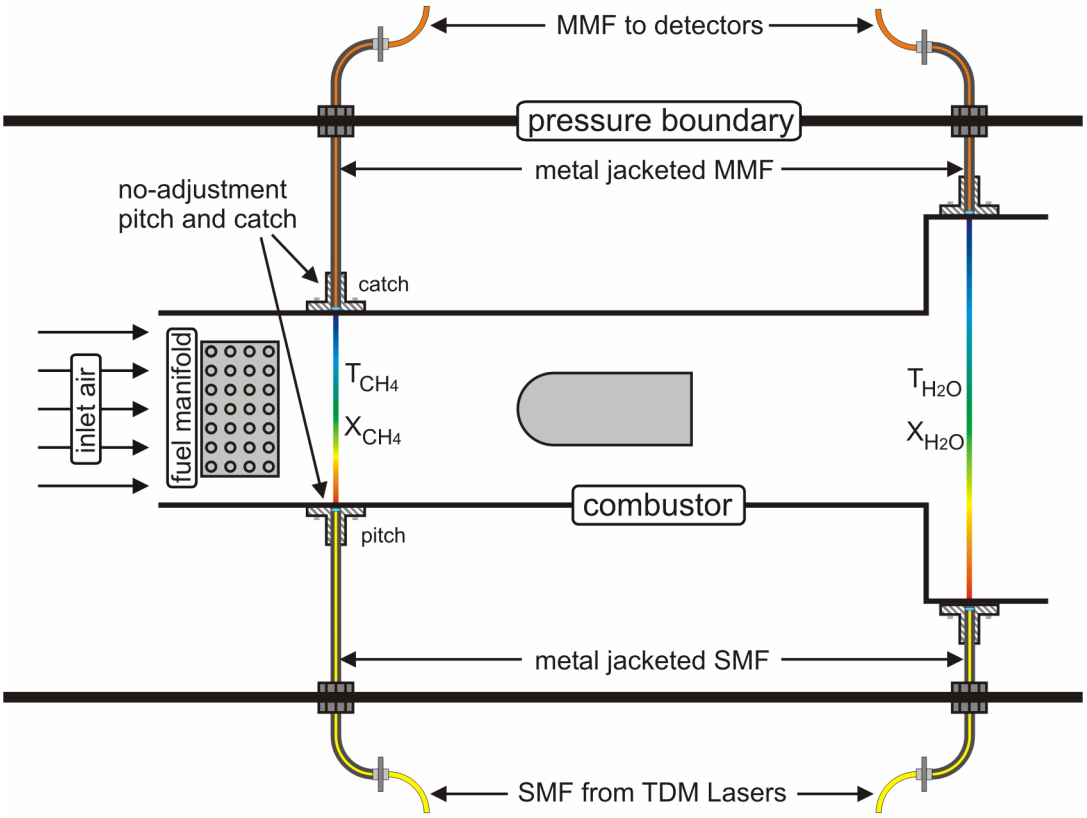

Figure 4.10: Schematic of test article showing location of fuel and water vapor measurements and illustrating the implementation of fiber-to-fiber coupling in a practical device

Optical access to the gas turbine combustor test article was achieved using an all-fiber system with no user adjustments. The system was simply installed by combustor technicians and immediately used for testing without any adjustment needed. Sensor light was delivered to the combustor using a single-mode fiber (SMF) with a collimating lens that also acted as the input window. A similar arrangement was used to collect light from the combustor and deliver it to the detection system, except that multimode fiber (MMF) was used. Ray tracing was performed to aid in the selection of lens focal lengths, fiber core diameters and NAs, and lens-to-fiber spacings. The goal of these selections was to limit transmission losses due to the

combined effects of the following misalignment sources: machining and assembly tolerances associated with the fixtures, thermal expansion of the optics and fixtures, and beam steering in the gas. Preliminary calculations showed that the dominant source from this list was the former, so only machining/assembly tolerances were considered in the final ray tracing efforts. The ray tracing converged on the selections listed in Table 4.4 for which machining/assembly tolerances of approximately 1 mm in translation and 3 degrees in rotation (both defined in terms of the axes of the pitch and catch assemblies) could be accommodated without loss of transmission. Rig machining was subsequently performed with a goal of keeping the tolerances significantly below the ~ 1 mm x 3 degree target. The fiber collimators were successfully installed in the high-pressure test rig resulting in a 100% transmission (neglecting Fresnel losses) immediately after installation for both the CH_4 test station and the H_2O test station.

Table 4.4 Fiber-optic access design parameters selected by aid of raytracing. The raytracing was designed to maintain 100% geometric coupling in the presence of the maximum acceptable machining tolerances listed. The lens-to-fiber spacing was set at room temperature by the manufacturer, then locked in place using ceramic epoxy.

λ [nm]	Fiber type	f_{lens} [mm]	To set lens-to-fiber spacing	Purpose	Machining tolerance
1670	SMF28e	2.8	Minimize spot size 58 mm from lens	Fuel pitch	2.6 degrees,
1670	MMF[a]	2.8	Minimize spot size 125 mm from lens	Fuel catch	1.1 mm
1350	SMF28e	2.8	Minimize spot size 125 mm from lens	Water pitch	2.8 degrees,
1350	MMF[a]	2.8	Minimize spot size 125 mm from lens	Water catch	0.86 mm

[a] core/clad - NA = 300/330 – 0.22

The MMF properties were selected to minimize mode noise while maintaining practicality. The 300 μm core and 0.22 NA were chosen to be large enough to maximize the speckle count and thereby minimize the mode noise [73] while small enough to easily image onto the 500 μm-diameter photodiode (Thorlabs PDA10CF). A MMF pigtail length of 30 m was

chosen to be long enough to further reduce mode noise through spectral averaging [74] while short enough to limit attenuation and cost.

The SMF fiber input and MMF fiber output assemblies were manufactured by Silicon Lightwave Technology, Inc., and designed to tolerate sustained exposure to 600°C. The collimating lenses were made of fused silica and were uncoated. The metal portions of the assembly were made of stainless steel. Ceramic epoxy served locking and strain-relief purposes. The assemblies were held into the combustor housing using spring-loaded clamps. The fibers were routed through a split-ferrule compression fitting at the pressure boundary. Light coupled into the catch MMF was guided to a photodetector (Thorlabs PDA10CF) and measured on a National Instruments PCI-5122 high-speed digitizer board operated at a nominal sample rate of 22 MSample/s/ch.

In order to utilize the delayed pulse referencing strategy, a free space 50/50 beam splitter cube (BSC) is used just ahead of the detector to allow both the engine path light pulse and reference pulse to be incident on the same detector. In order to reduce the effects of polarization dependence of the cube, both output beams were measured with two different detectors as shown in Figure 4.9 and Figure 4.11. Figure 4.11 shows the time trace of a single cycle of the 10 color TDM laser. The first color burst corresponds to the 10 colors that went through the engine path (I) and is followed by the delayed 10-color burst to be used as the reference (Io). The signal from each detector is plotted. The information sought from this time trace is the absolute absorbance for each of the 10 colors composing the burst; Figure 4.11 graphically depicts the process used to obtain this information.

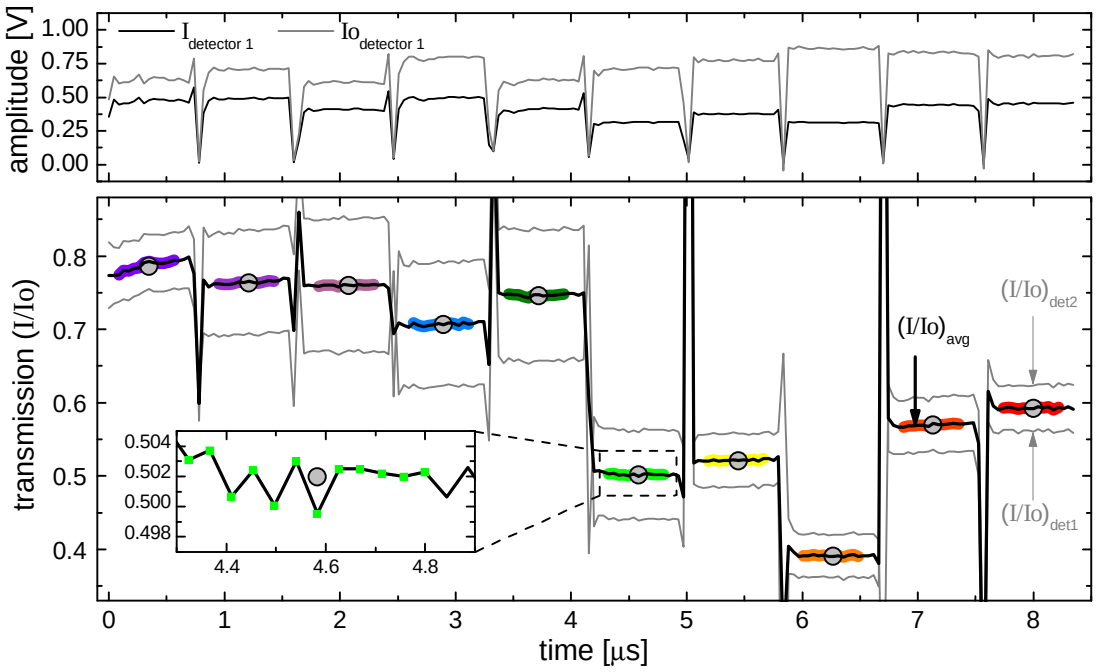

Figure 4.11: Post-processing of a single TDM data frame to a 10-wavelength spectrum. TOP PANEL: The Io trace is advanced ~ 17 μs to align it with the I trace. BOTTOM PANEL: Transmission (I/Io) for both detectors downstream of the beamsplitter cube. These two signals differ because of uneven optical splitting in the cube. The average of the two detector signals is shown as the thin black trace and this average is essentially polarization insensitive. The final transmission value at each of the 10 wavelengths is calculated by taking the average of the points in each wavelength pulse as shown by the inset graph.

In the top panel of this figure, the I and Io traces for a single detector have been plotted together. An external clock (Stanford Research Systems CG 635) based on an oven controlled crystal oscillator (OCXO) provides the data acquisition sample clock and is phase locked to the function generator driving the TDM source so that the Io delay is always an integral multiple of the time per sample, thus making the realignment process of I and Io straightforward. Acquisitions using the water TDM laser had the sample clock set to 23.1256 MHz and with the fuel TDM the sample clock was 21.915051 MHz. The timing resolution of the external clock also allowed for the I and Io signals to be sampled identically, thus

minimizing common mode noise between the two signals in this ratiometric measurement. After computing the ratio (I/Io) for each detector signal (detector 1 and 2), the two detector signals are averaged. The resulting two-detector average signal exhibits low sensitivity to polarization, although effects of changing polarization states of the input light from sources such as vibration of the optical fibers can be seen on either detector 1 or detector 2 individually. The bottom panel of Figure 4.11 shows these 3 signals. Detector 2 shows a higher transmission for each wavelength as compared to detector 1, due to the uneven splitting ratio of the BSC. Finally, points sampled during each wavelength bin are averaged leading to the final value of relative absorbance for that particular wavelength. This process is then repeated for repetitive cycles of the TDM laser resulting in a time series of relative absorbance at each wavelength which can be reduced to a time series of temperature and absorber concentration.

4.2.3 Results and discussion

CH_4 results

As discussed in the previous section, simple post-processing of the data yields the relative absorption of each wavelength versus time. However, in order to determine gas properties, the absolute absorbance is needed. Therefore, the measurement needs to be "baselined" in some fashion. In the case of the CH_4 TDM sensor, this baselining was straightforward in that data was acquired before the main fuel valve was triggered to open, thus providing a period at the start of each measurement in which no CH_4 was present in the optical path. This baseline time can be seen in Figure 4.12. During this null time, the average value of the absorbance of each color is calculated and then subtracted from the entire time history giving

rise to absolute absorption values which can then be compared with simulations based on the HITRAN2004 database [22] to infer the CH_4 gas properties.

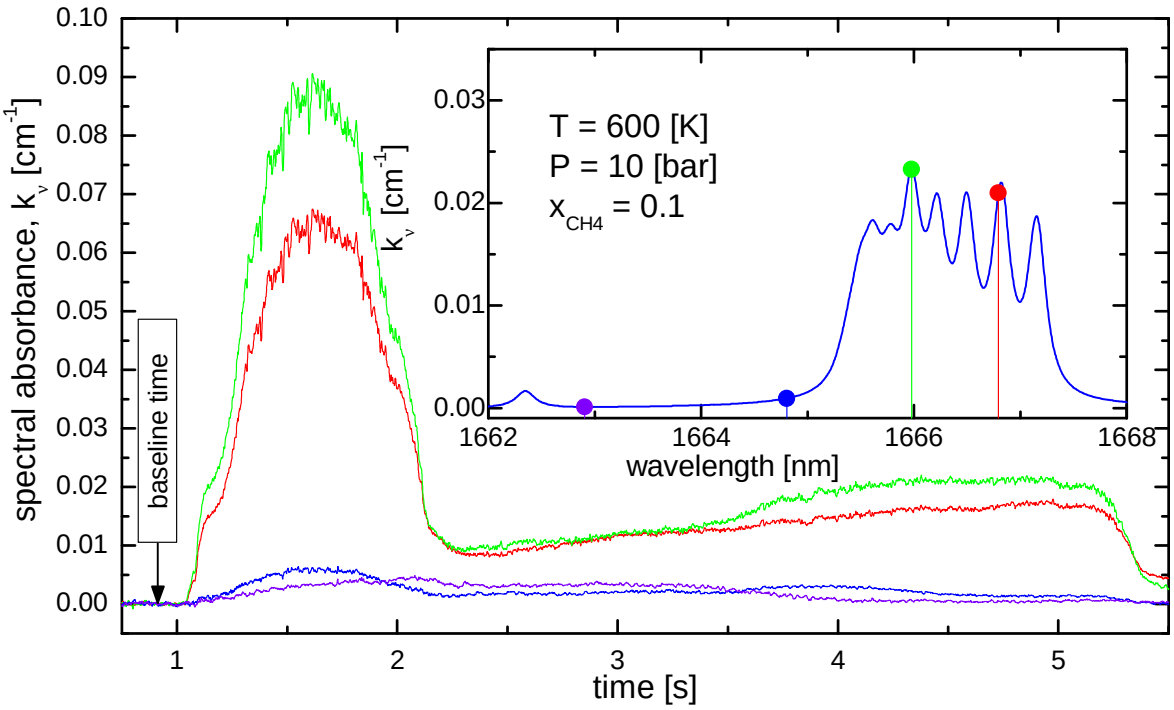

Figure 4.12 CH4 absorbance versus time at the four wavelengths highlighted in the inset spectrum

Figure 4.13 shows the resulting time trace of the CH_4 mole fraction for a single test case. In the bottom panel of this figure, the mole fraction is zero until a time of ~ 1 sec at which it begins to rise owing to opening of the fuel valve which in turn releases CH_4 into the optical path. Fuel remains present for the rest of time that optical data was acquired allowing for the simultaneous temperature and fuel mole fraction measurement as shown in Figure 4.13. Temperature was not a direct design objective for this particular sensor but reasonable estimates were also able to be inferred from the data and corroborated by means of a thermocouple in the fuel stream.

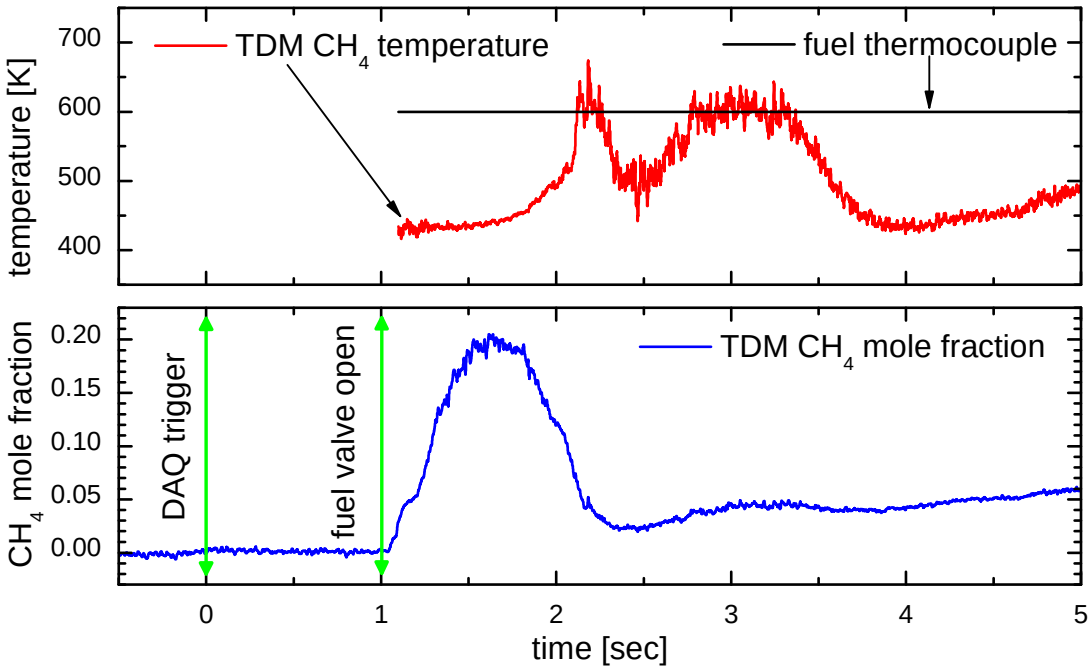

Figure 4.13: Results from the fuel TDM sensor operating at 10.5 bar. The fuel thermocouple was monitored periodically, not logged, thus it appears as a constant in this plot. The fuel TDM sensor was designed to measure fuel vapor given a thermocouple-based estimate of temperature, but temperatures inferred from the TDM spectra demonstrate the possibility of fuel thermometry by this method.

H_2O results

The TDM water vapor measurement presented the same challenge for determining absolute absorbance as the fuel TDM in needing to baseline the sensor to account for optical losses from sources other than molecular absorption. However, the H_2O TDM measurement was unique in that throughout the entire time history of acquired optical data, H_2O was present in the optical path. Therefore, there was no zero absorption point in the time history that could be used to provide a simple reference as in the case of the CH_4. In order to overcome this problem, a more advanced baselining procedure was carried out and relied on data provided by a fast response thermocouple located near the H_2O TDM optical path.

Before the main fuel was turned on, temperatures in the combustor were fairly constant and low enough to allow for confidence in the thermocouple measurement. Optical and thermocouple data was then continuously acquired before and after the main fuel thus providing a window of time in which the TDM can be baselined against the thermocouple. To do this, optical data at one time within the baselining window, the baseline time (BT), is forced to be the same temperature as the thermocouple, while the mole fraction of H_2O is treated as a free parameter in the fitting routine. An initial mole fraction guess value is prescribed at the BT fully constraining the absorption data to specific values for each of the 10 wavelengths. Spectral offsets at each wavelength are then calculated by taking the difference from the measured absorption values at BT from spectra simulated using the BT2 spectral database [23] at the set temperature and H_2O mole fraction. These offsets are then subtracted from the entire time history of the H_2O TDM data. Least-square fits of the corrected measured spectra to simulated spectra are carried out with the best fit simulated spectra chosen by minimizing the mean-square-error (MSE) of the fits [28] resulting in a time history array of inferred temperatures, mole fractions and best fit MSEs. This procedure is repeated for different initial guesses of the BT mole fraction with the final choice decided by summing the MSEs for each guess and choosing the minimum of these sums.

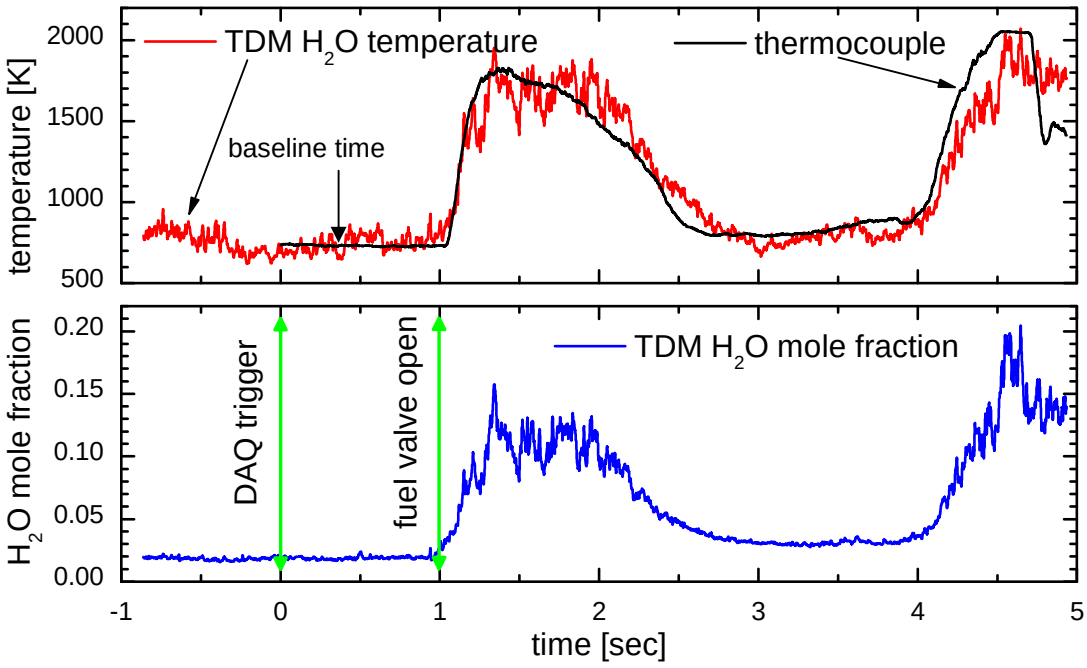

Figure 4.14: Results from the H2O TDM sensor at 10.5 bar rig pressure. TOP PANEL: Temperature inferred from the TDM measurement, along with data from a fast-response thermocouple. A free parameter in the iterative baselining scheme was fixed by forcing the TDM temperature results to match the thermocouple results at the indicated baseline time. BOTTOM PANEL: H2O mole fraction results. Significant H2O present before the main fuel was turned on prompted the iterative baselining scheme.

The final results are shown in Figure 4.14 with the TDM H_2O and thermocouple temperatures plotted in the top panel and the optical H_2O mole fraction shown in the bottom panel. Good agreement is shown between the thermocouple and the TDM temperature data. Useful information about the dynamics of the combustor during this type of operation was realized. Even though this particular utilization of the TDM relied on a concomitant measurement of temperature along with an iterative approach to setting an initial mole fraction, it should be noted that other laser based methods can be adopted in the future to measure the baseline conditions. For instance, a relatively slow wavelength-swept absorption measurement could have been easily implemented using the same optical path to

measure the initial conditions to allow for a straightforward baselining of the TDM similar to the CH_4 TDM measurement.

4.2.4 Conclusions

The successful use of custom TDM sources for measuring CH_4 and H_2O in a practical gas turbine combustor test article has been demonstrated. Measured temperature and mole fractions have been presented. Because the TDM source samples only select wavelengths, sensor data acquisition rates can be modest. Although the data acquisition rate used here was 22 MS/s/channel, even lower rates (down to perhaps 1 MS/s) could be used in future versions of such sensors without sacrificing overall engineering data rates. Low data acquisition rates are particularly attractive for sensor designs in which TDM sources would be distributed to numerous laser beam paths through the test article to enable tomographic imaging of gas properties.

Low-loss fiber-optic access to the high-pressure, high-temperature combustor was accomplished with an adjustment-free design. A 300 µm-core collection fiber which is easily coupled to ~100 MHz-bandwidth photoreceivers was used as the collection fiber.

The successes demonstrated here should help pave the way for expanded use of absorption spectroscopy in practical combustors.

4.3 ROCKET PLUME

Absorption spectroscopy is an optical technique that lends itself useful to inferring gas properties in harsh and non-uniform environments due to its ability for making non-intrusive, quantitative measurements. The primary species produced in rocket combustion using

hydrogen or hydrocarbon fuels is H_2O vapor which has an absorption signature in the 1300 – 1700 nm wavelength range. Sensors developed in this range of the electromagnetic spectrum can utilize the well-developed photonics devices of the telecommunications industry thus making them cost effective and rugged.

The spectroscopy of water vapor is rich with information about the quantum mechanical and thermodynamic state of the molecules in the probe beam path. The two main properties sought after in this work are the temperature and species concentration in the plume of a rocket. Temperature is inferred by comparing the relative populations of water molecules in different quantum states and the concentration can be deduced by measuring the intensity of a particular transition while knowing the functional dependence of the transition to temperature and pressure.

The absorption features studied in this work arise primarily from transitions in the $\nu_1+\nu_3$ and $2\nu_1$ ground state and hot bands over the wavelength range of 1380 – 1476 nm. There are lines from other vibrational bands but these transitions are below the minimum detectable absorbance of this experiment. The example spectra shown in Figure 4.15 show the dramatic effect temperature has on the absorption profile. The 300 K spectrum shown in black has a peak absorption that is approximately an order of magnitude greater than a spectrum at the same pressure and H_2O concentration but corresponding to a temperature of 2000 K. The effect of increasing temperature is to populate more energy levels thus decreasing the intensity of strong lines at room temperature (transitions at lower energy levels), while increasing the absorption of transitions from states at higher energy. This redistribution of

population of energy levels is governed by Boltzmann statistics from which the temperature of the gas can be inferred.

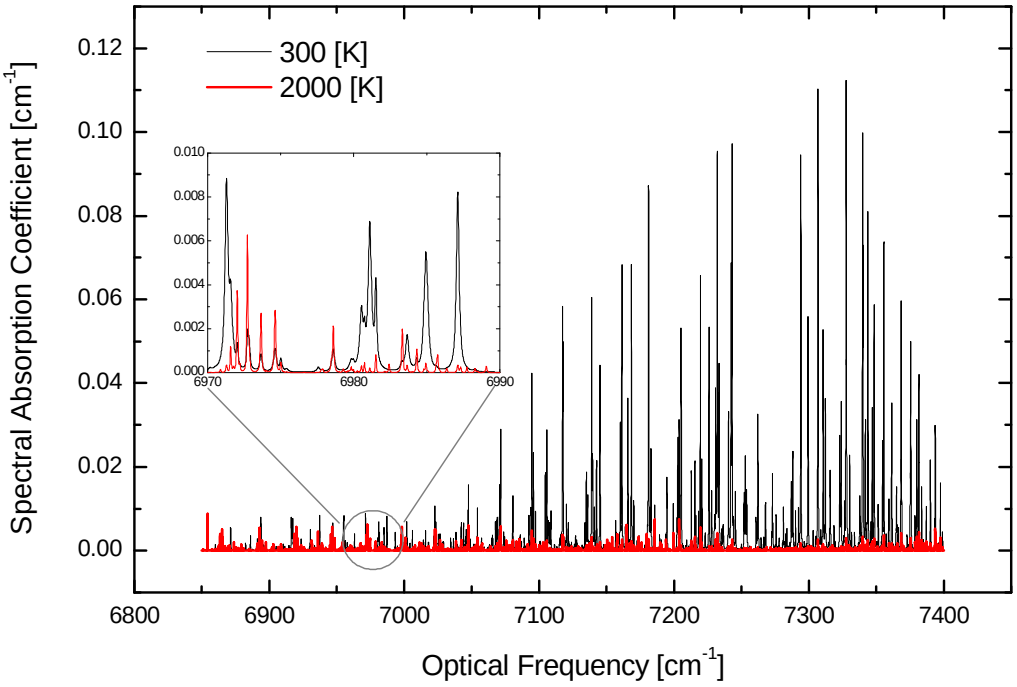

Figure 4.15 Simulated spectra in the optical range used in this study. The black curve represents a spectrum at 300 K and the red curve is representative of the absorption at 2000 K. The inset figure shows the dramatic effect temperature has on the spectrum.

4.3.1 Management of non-uniform flows

In typical laser absorption measurements, a single laser beam is passed through a sample and the path integrated average properties can be measured. If the sample volume is uniform in temperature, pressure, and concentration the thermodynamic state of the entire volume can be assessed. However, in practical applications the flow field is usually not uniform along a single path so advanced techniques are necessary. For instance, Figure 4.16 compares a measured water vapor absorption spectrum to a best fit simulation at a single temperature and

a superposition of simulated spectra over a distribution of temperature. The measured spectrum fits better to the distribution than the single temperature simulation. This type of analysis can give the temperature distribution and the optical depth (product of path length and concentration) for each temperature zone. However, the different temperature zones cannot be mapped to physical space since the single line-of-sight measurement contains no information of how to order the different zones and the actual size of the zones. For more information the reader is referred to the following publications [6, 75]

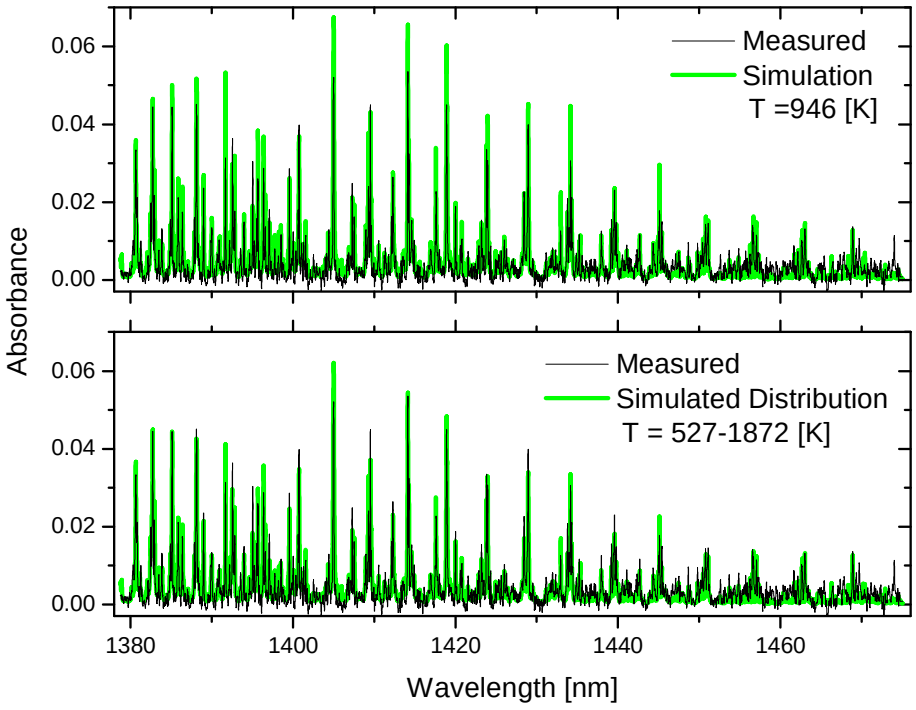

Figure 4.16 Absorption spectrum along a non-uniform path. The measured spectrum fits better to a weighted superposition of multiple temperature simulations versus a single temperature simulation.

Computed tomography is a technique in which a physical image can be reconstructed from multiple projections, where a projection is another name for a line-of-sight measurement. For this work, the rocket plumes are assumed axis-symmetric which reduces the tomography

to a 1D problem. Two different algorithms were used to reconstruct assumed axis-symmetric radial profiles of temperature and water mole fraction, an algebraic reconstruction technique (ART) and an Abel inversion.

Algebraic reconstruction technique

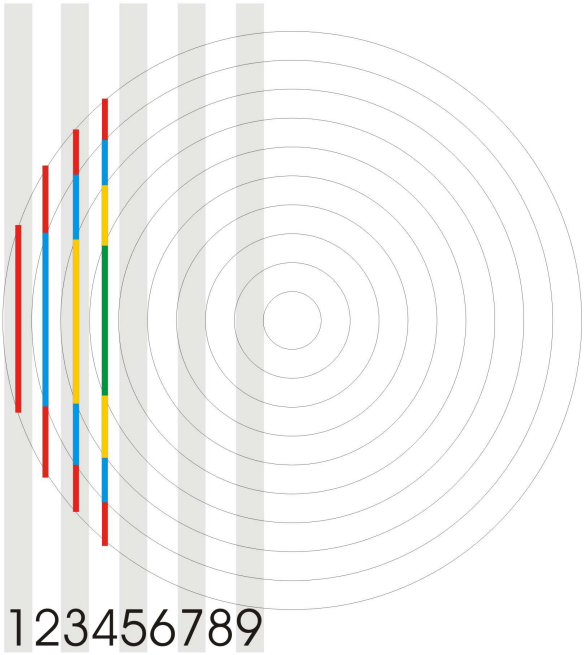

Figure 4.17 Geometric description of the algebraic reconstruction technique

The algebraic reconstruction technique used for reconstructing the radial profiles can be viewed as simply peeling the layers of an onion to probe towards the center of the distribution. Figure 4.17 gives a pictorial representation of the ART algorithm. Radial rings around each line-of-sight projection are assumed to have constant properties with a ring width equal to the spacing, Δr, of each projection P_i. The projections are depicted in the figure by the numbered alternating gray and white rectangles. To infer the properties of each

ring, the algorithm starts with the outermost projection, P_1, and calculates the temperature and water mole fraction of that projection using the path length through that section of the ring. To solve for the next inward ring, the portion of the path, P_2, contributed by P_1 is calculated and subsequently subtracted from P_2 to extract the uniform radial spectra of P_2. This process continues inward until all the radial spectra are obtained from which the radial distribution can be calculated.

Abel inversion

The absorption of water vapor in the P branch of the $\nu_1+ \nu_3$ combination band centered at 1385 nm can be quantified with Beer's Law given in Equation (4.1). Spectra are frequency resolved with the narrow line width of the laser permitting spectral line shapes to be measured with negligible instrument broadening.

$$\left(\frac{I}{I_o}\right)_{\nu,x} = \exp\left(-\int_0^L k(y;\nu)dy\right) \tag{4.1}$$

This equation is valid at each frequency of light and allows for the local spectral absorption coefficient, $k(y;\nu)$, to vary along the line-of-sight measurement shown in Figure 4.18. Each line-of-sight measurement is collectively called a projection when performing tomography in that the variable of interest is essentially projected through the non-uniform path before being recorded.

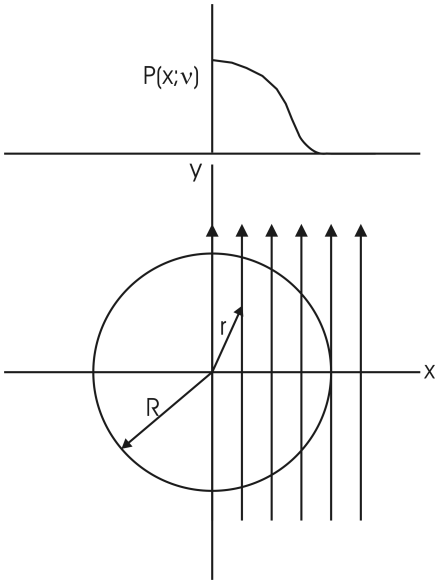

Figure 4.18 Geometric description of variables used in the Abel transform

The variable of interest in this study to be used for each projection is the natural logarithm of the recorded transmissivity which can be recast in terms of the radial coordinate shown in Equation (4.2).

$$P(x;\nu) = -\ln\left(\frac{I}{I_O}\right)_{\nu,x} = 2\int_x^R \frac{k(r;\nu)\, r\, dr}{\left(r^2 - x^2\right)} \tag{4.2}$$

$$k(r_i;\nu) = \frac{1}{\Delta r}\sum_{j=0}^{\mathbf{N-1}} \mathbf{D}_{ij} P(x_j;\nu) \qquad 0 \le i, j \le N-1 \tag{4.3}$$

In order to obtain the radial spectral absorption coefficient, a tomographic inversion is needed. The technique employed here is based on the work of Dasch and Varghese and Villarreal where a three-point Abel algorithm was developed that reduces the Abel inversion to simple matrix multiplication by introducing a linear operator. This algorithm employs a 3-point interpolation scheme to provide smoothing to the output radial function. Equation (4.3) describes the mathematics of the inversion. This equation is valid at each frequency of light and the deconvolution matrix, **D**, need only be computed once as it depends only on the

number of projections, N. The local radial spectral absorption coefficient is obtained at each frequency and these can be combined to produce an absorption spectrum at each radial node.

4.3.2 Sensor configurations

Various schemes of laser beam scanning have been developed and tested. All utilize some form of mechanical scanning in order to probe the sample space. The main requirement for axis-symmetric tomography is that half of the rocket plume be scanned so that a reconstruction of the radial profiles can be performed. There are two general techniques to carry out the spatial scanning, parallel beam and fan beam geometries. In parallel beam, the multiple beam paths through the plume are all parallel and the overall width of the scan is constant where as in fan beam the beams are angularly separated and the overall angle of the scan is constant. These two geometries are depicted in Figure 4.19. The image on the left shows the parallel beam configuration with the beam paths all aligned with the Y axis where as the image on the right shows the angular spreading of the beam paths with respect to the Y axis. Under the axis-symmetric assumption, these two geometries give the same information with the fan beam easily transformed to the parallel beam through simple coordinate axis rotation for each projection.

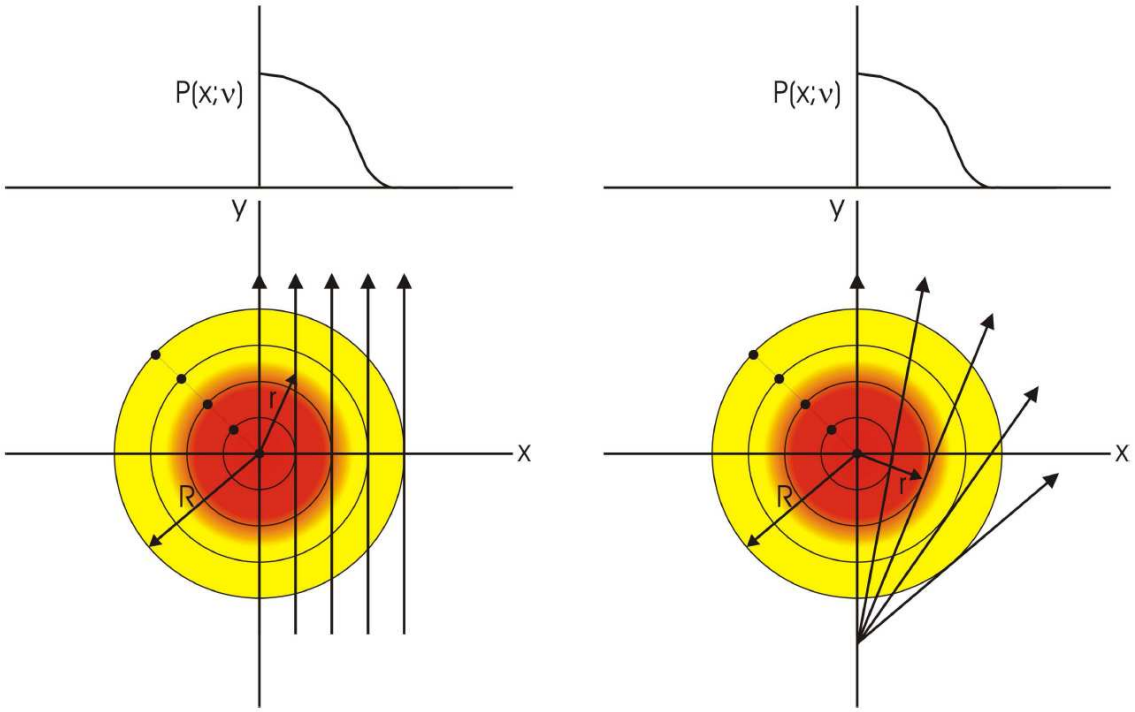

Figure 4.19 Parallel beam geometry (left) versus fan beam geometry (right). Under the axis-symmetric assumption, the fan beam is identical to the parallel beam with a coordinate axis rotation for each projection

Dual Pass Parallel Beam (DPPB)

In order to optically interrogate spatial properties of a rocket plume, a dual pass parallel beam (DPPB) system was constructed and is depicted in Figure 4.20. The laser light enters the system via a single mode optical fiber and is collimated with an aspheric lens. The collimated light is then split by a 50/50 beamsplitter with one leg dumped and the other directed towards a rapidly vibrating mirror. The vibrating mirror used throughout this project was a resonant scanner from GSI Lumonics Inc., with a nominal scan frequency of ~8 kHz and voltage adjustable scan amplitude. The vibrating mirror steers the laser beam in a raster fashion creating an angular scan comprised of a single beam at any instant of time. A 90 mm

focal length cylindrical lens is placed a focal lengths distance from the vibrating mirror to create the parallel beam scan. The parallel beams are then directed through the plume for a first pass and then reflected by a planar mirror on the same path back through the plume for a second absorption pass. The dual pass effectively doubles the signal-to-noise ratio, SNR, by doubling the absorption while the noise remains relatively constant with respect to a single pass measurement.

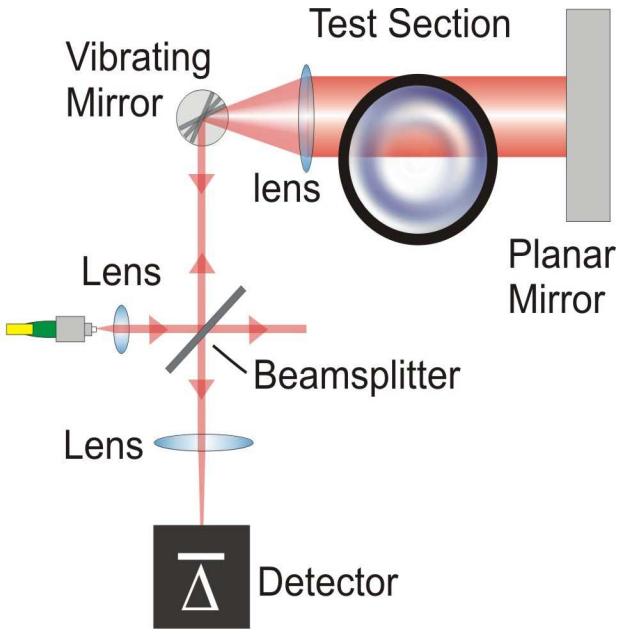

Figure 4.20 Schematic of Dual Pass Parallel Beam sensor

The parallel beams are then redirected onto the vibrating mirror by the cylindrical lens resulting in a single beam in the same spatial position as the input light to the vibrating mirror. The beam then passes through the beam splitter and onto a single photodiode to measure the transmission. It should be noted that the “laser sheet” shown going through the plume is not a sheet but rather a beam traversing back and forth due to the directional change imparted by the vibrating mirror. Since the mirror dynamics are simple harmonic oscillation,

the position of the beam with respect to time can be calculated using a sinusoidal function and thus the transmission as a function of position is known.

Dual Pass Fan Beam (DPFB)

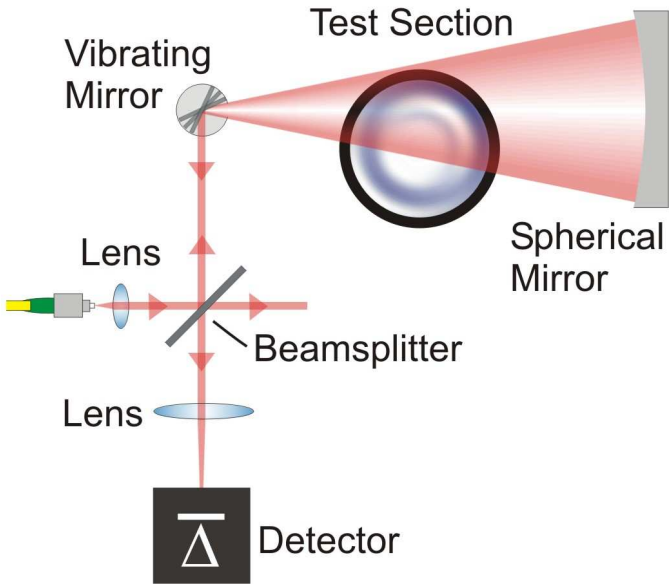

Figure 4.21 Schematic of Dual Pass Fan Beam sensor

To exploit the axis-symmetric assumption, the DPPB system was slightly modified to create the dual pass fan beam (DPFB) system shown in Figure 4.21. Simply removing the cylindrical lens and replacing the planar mirror with a spherical mirror was all that was needed to make the transformation. The mechanical operation is identical for both systems with the DPFB having better optical properties. Eliminating the cylindrical lens decreases reflection losses and allows for more compact packaging by eliminating the focal length distance needed for creating the parallel beams. The spherical mirror decreases susceptibility to beam steering by adding focusing control to the reflected Gaussian beam. Finally, the path

length through the ambient environment is the same for every spatial position simplifying data analysis.

4.3.3 Experimental results

Experiments were performed with different chamber/nozzle geometries and fuel/oxidizer combinations. Results were obtained for both the DPPB and DPFB sensor configurations using both the algebraic reconstruction technique and the Abel inversion. It was found that the ART was not a reliable algorithm for tomography in harsh flows. It will be shown that the DPFB sensor and the Abel inversion outperform the other methods with the results showing great promise for accurately reconstructing the temperature and H_2O concentration radial profiles.

Shown in Figure 4.22 is the radial temperature distribution obtained from the plume of a methane/oxygen fueled rocket using the High Performance Methane Thrust Chamber (HPMTC).

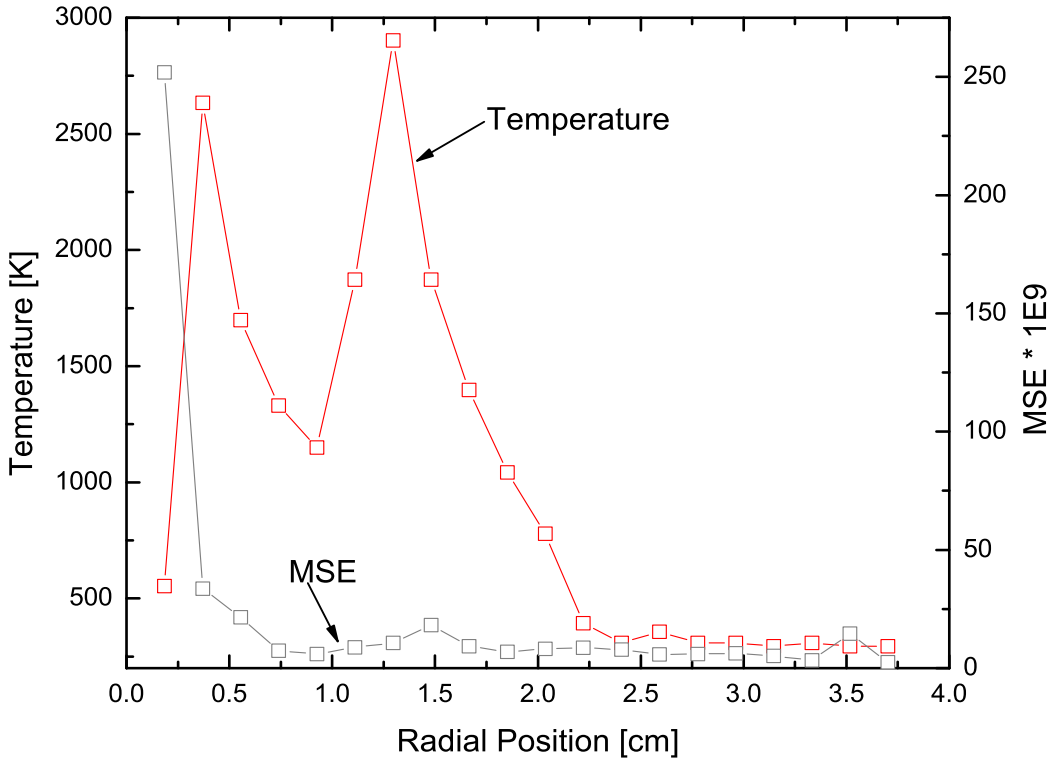

Figure 4.22 Radial temperature distribution obtained from the plume of a CH4/O2 fueled rocket using the algebraic reconstruction technique (ART). Also shown is the mean-square-error (MSE) of the fitting routine.

The measured chamber pressure was 8.846 atm with an O/F ratio of 3.5. The combustion products were expanded through a nozzle with an expansion ratio (A_{exit}/A_{throat}) of 2. The measured spectra were inverted using the algebraic reconstruction technique (ART) and then fit to a library of spectral simulations to find the best fit temperature and water mole fraction. The best fit temperature is obtained by finding the minimum mean-square-error (MSE) of the least-squares fitting of measured to simulated spectra. The measured temperatures agree well with the ambient conditions away from plume but erratic behavior is evident closer to the plume axis. Contrast this to the results shown in Figure 4.23 obtained by using an Abel

inversion on the same data. A smoother profile is extracted with the Abel inversion and the magnitudes of the MSE points are lower. However, the absolute accuracy is still questionable, especially near the center where the temperature is limited to 3000 K by the simulation library. The mole fraction appears to decrease near the center, but this would not be the case if the fitting routine were allowed to go to higher temperatures since a higher temperature best fit would result in higher mole fractions.

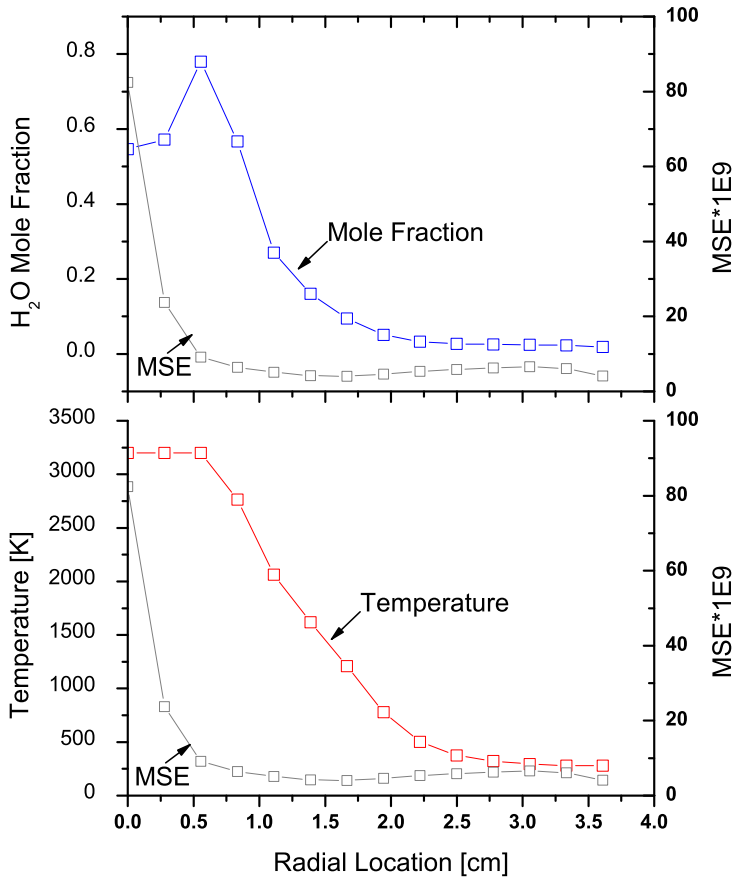

Figure 4.23 Temperature and water mole fraction radial profiles using an Abel inversion on the same experimental data used in Figure 4.22. The Abel inversion leads to better fits to simulations (lower MSE values) resulting in smoother profiles near the center of the plume.

Under these operating conditions, an ideal rocket calculation using a chemical equilibrium analysis would result in an exit temperature of 2860 K with a water mole fraction of 0.5. The measured values exceed the theoretical values near the center and this is also where the fits become unreliable. The Abel inversion allowed for a better reconstruction towards the center of the plume over the ART method but problems are still present in the measured spectra. The dual pass parallel beam sensor used for these two cases was fairly sensitive to beam steering and this resulted in a fair amount of experimental noise. The dual pass fan beam sensor was developed to reduce the noise floor to allow more accurate reconstructions especially towards the center of the plume.

Another test was performed using the DPFB sensor with the HPMTC under slightly different operating conditions. The chamber pressure was lower at 7.54 atm and the OF ratio used 3.29. Figure 4.24 shows the measured temperature profiles along with the equilibrium values obtained using the NASA CEA code. The DPFB sensor gave results with lower noise so the reconstruction was able to infer properties closer towards the center of the plume. Since the measurement plane was located 7.5 cm from the nozzle exit plane, the measured temperature never reaches the equilibrium temperature and this is attributed to heat transfer occurring before the gas reaches the measurement plane.

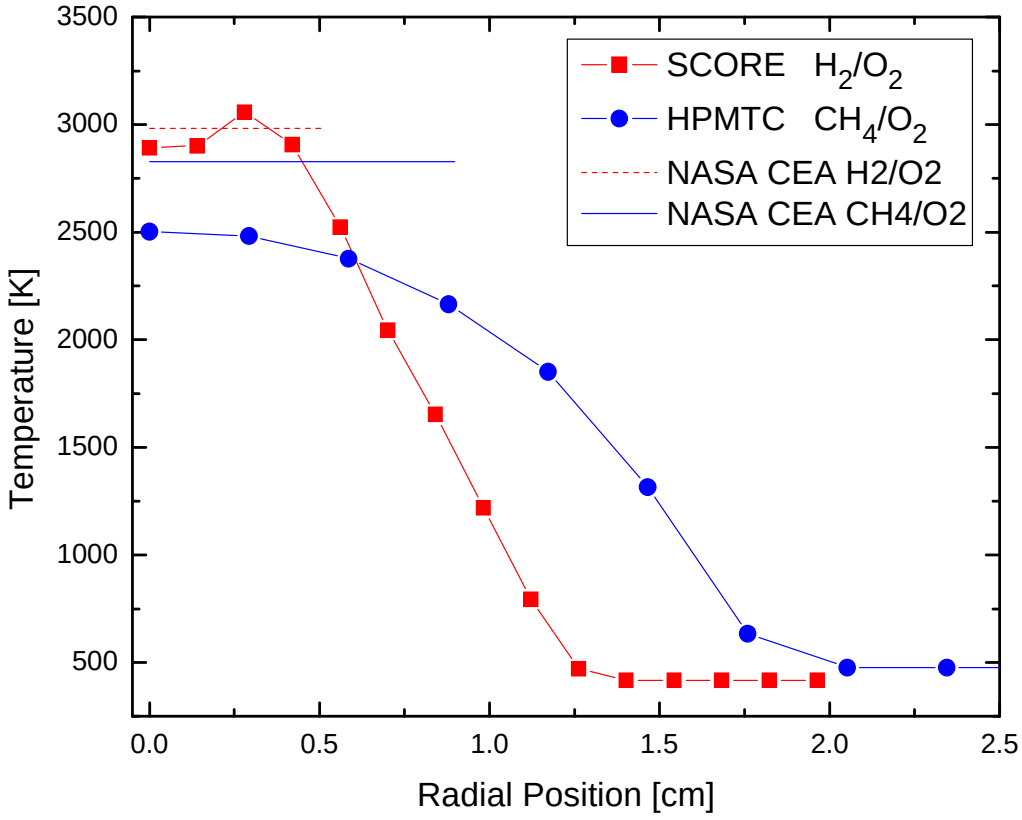

Figure 4.24 Temperature profile from measurements of the plume gas from two different rocket motors. Also shown is the calculated temperature from chemical equilibrium and the length of the CEA calculated lines represents the radius of the exit of the nozzle.

A further test of the DPFB sensor was carried out by testing a different chamber/nozzle configuration using gaseous hydrogen and gaseous oxygen as the fuel and oxidizer. This chamber produced smaller thrust values and a smaller plume diameter. The expansion ratio of the nozzle was 1.5 with a chamber pressure of 7.033 bar operating at a H_2/O_2 OF ratio of 8.08. Figure 4.24 also plots the temperature results from this test along with the chemical equilibrium results. For this case, the measurement plane was able to be located much closer (4.8 cm) to the nozzle exit plane and better agreement between the measured core temperature and the equilibrium calculation are obtained.

CHAPTER 5. CONCLUSIONS

This work has presented ideas and solutions for absorption based thermometry in combustion applications. While the key focus has been on water vapor absorption, the ideas should be tractable to other molecular species. The example applications discussed in Chapter 4. highlight the challenges experienced when making measurements in real devices and give some possible solutions for overcoming these difficulties. Of most importance, however, is the methodology laid out in Chapter 3. for analyzing and predicting the performance of these sensors. The key points of this thesis can be summarized as follows:

- Previously, two color absorption thermometry used general guidelines for choosing wavelengths such as maximizing the difference in lower state energies while keeping the ratio of the absorbances within some arbitrary range [16]. This old strategy provided guidance for selecting 1 but not both wavelengths. This work provides a method for choosing both wavelengths through the optimization of equation 3.17 and this method is quantitative.

- When considering an absorption based thermometry technique for conditions where collisional broadening dominates the line shape of the spectral features, it is desirable to analyze the performance of the sensor in terms of the absorbance since this is what is directly measured in the experiment and the spectrum offers a simple means of data compression compared to using the more fundamental parameters.

- The ratio spectrum and difference spectrum provide a quick way of estimating the best choices of wavelengths for optimizing thermometry with the ratio spectrum offering

insight into the aggregate lower state energies and the difference spectrum providing an estimate of the sensitivity of an absorption feature to temperature

- The use of the Boltzmann plot for inferring temperature is an idea that has been used for quite some time. However, using this idea for choosing wavelengths when considering experimental noise in multi-wavelength measurements is believed to be novel.

- Choosing wavelengths by minimizing an appropriate objective function through the use of a smart search algorithm (genetic algorithm) when considering measurement noise is an efficient technique that converges quickly. This is in contrast to an objective function based on iterative means of estimating the variance in temperature measurements that is costly to compute and may not converge to the true global minimum.

- The methodology laid out in section 3.4 for choosing N wavelengths for water absorption thermometry is quantitative and is based solely on what is measured in an experiment; the absorption spectrum.

- When considering wavelengths for measuring over a wide temperature range there is an optimum number of wavelengths when considering a fixed measurement time (i.e. the noise increases as the number of wavelengths considered increases). However, the improvement in choosing this optimum number of wavelengths versus measuring the entire spectrum is only on the order of a factor of 4 so it may be desirable to measure the entire spectrum for improved immunity to other noise and error sources (e.g. baseline uncertainty) at the expense of a moderate decrease in temperature precision.

This work hopefully provides a foundation for further improvements in the design of absorption based sensors especially related to the issue of wavelength selection for optimizing temperature precision. There are a few other topics related to this work that can and should be continued further in order to advance the performance of this particular class of optical diagnostic.

5.1 FUTURE WORK

The major premise of this thesis was building an understanding and optimizing performance of absorption based sensors when considering errors that only affect the precision of a measurement. The accuracy of the temperature inferred in H_2O absorption measurements is limited by the accuracy of the underlying fundamental spectroscopic parameters used to simulate the absorption spectrum (i.e. the accuracy of BT2 and other spectral line lists). In practice, it is possible to measure spectra at a variety of conditions in order to estimate the accuracy of the sensor but even this proves difficult when considering the extreme conditions encountered in practical combustion devices. Therefore, a more fundamental study is needed with experiments playing a pivotal role through the acquisition of high quality spectra at a variety of conditions that can be confirmed through concomitant measurements. Of particular interest are high temperature flame measurements at low pressure where the simple and well known line broadening mechanisms allow for better measures of the spectral line intensities and positions. This information would be useful for improving the spectral line lists either directly through updating the current parameters or indirectly by improving the empirical data used in quantum mechanical calculations of the intensities and positions of transitions.

More directly related to the main theme of this thesis, further work can be pursued in identifying optimum wavelengths for thermometry. For instance, instead of only considering noise in the absorbance, the uncertainty in the wavelength can also be included within the framework developed. Similarly, the noise used in the optimization can be expanded to include terms from shot and signal based noise in order to more closely represent the real signals in an experiment. However, the noise will be specific to a particular system so any further modifications to mimic the true measurement would not be as general as the fixed noise case used in this work. Another possible improvement would be to consider other H_2O absorption bands. There are fundamental vibrational bands at higher wavelengths that possess inherently stronger absorption. The optical devices for working at these wavelengths might not be as economical or convenient as those in the telecom range but the gains in absorption strength and the possibility of improved thermometry performance may warrant the extra expense.

REFERENCES

[1] R. K. Hanson and P. K. Falcone, "Temperature-Measurement Technique For High-Temperature Gases Using a Tunable Diode-Laser," Appl. Opt. 17, 2477-2480, 1978.

[2] E. R. Furlong, D. S. Baer, and R. K. Hanson, "Combustion Control and Monitoring using a Multiplexed Diode-Laser Sensor System" in *26th Symposium (International) on Combustion*, "Combustion Control and Monitoring using a Multiplexed Diode-Laser Sensor System" , 1996.

[3] S. T. Sanders, D. W. Mattison, J. B. Jeffries, and R. K. Hanson, "Rapid temperature tuning of a 1.4-um diode laser with application to high-pressure H2O absorption spectroscopy," Opt. Lett. 26, pp. 1568-1570, 2001.

[4] L. A. Kranendonk, R. Huber, J. G. Fujimoto, and S. T. Sanders, "Wavelength-agile H_2O absorption spectrometer for thermometry of general combustion gases," Proc. Comb. Inst. 31, pp. 783-790, 2007.

[5] E. R. Furlong, D. S. Baer, and R. K. Hanson, "Combustion Control using a Multiplexed Diode-Laser Sensor System" in *Part 2 (of 2)*, "Combustion Control using a Multiplexed Diode-Laser Sensor System," Combustion Inst, Pittsburg, PA, USA, pp. 2851-2858, 1996.

[6] S. T. Sanders, J. Wang, J. B. Jeffries, and R. K. Hanson, "Diode-laser absorption sensor for line-of-sight gas temperature distributions," Appl. Opt. 40, 4405-4415, 2001.

[7] M. P. Arroyo and R. K. Hanson, "Absorption measurements of water-vapor concentration, temperature, and line-shape parameters using a tunable InGaAsP diode laser," Appl. Opt. 32, 6104-16, 1993.

[8] L. A. Kranendonk, J. W. Walewski, T. Kim, and S. T. Sanders, "Wavelength-agile sensor applied for HCCI engine measurements," Proc. Comb. Inst. 30, 1619-1627, 2005.

[9] L. A. Kranendonk, J. W. Walewski, S. T. Sanders, J. Huber, and J. G. Fujimoto, "Measurements of Gas Temperature in a HCCI Engine Using a Fourier Domain Mode Locking Laser," SAE2006-01-1366, 2006.

[10] T. Kraetschmer, A. W. Caswell, K. D. Rein, S. T. Sanders, S. Roy, D. T. Shouse, B. V. Kiel, and J. R. Gord, "Multi-Spectral, Multi-Path Absorption Spectroscopy at 30 kHz using Time-Division Multiplexed Lasers" in *47th AIAA Aerospace Sciences Meeting*, "Multi-Spectral, Multi-Path Absorption Spectroscopy at 30 kHz using Time-Division Multiplexed Lasers" , 2009.

[11] L. Ma and W. Cai, "Numerical investigation of hyperspectral tomography for simultaneous temperature and concentration imaging," Appl. Opt. 47, 3751-3759, 2008.

[12] L. Ma and W. Cai, "Determination of the optimal regularization parameters in hyperspectral tomography," Appl. Opt. 47, 4186-4192, 2008.

[13] T. Kraetschmer and S. T. Sanders, "Simple Multiwavelength Time-Division Multiplexed Laser for H2O Absorption Measurements" Optical Society of America, 2008.

[14] T. Kraetschmer and S. T. Sanders, "Ultrastable Fourier Domain Mode Locking Observed in a Laser Sweeping 1363.8 – 1367.3 Nm" in *Conference on Lasers and Electro-Optics (CLEO)*, 2009.

[15] M. P. Arroyo, S. Langlois, and R. K. Hanson, "Diode-laser absorption technique for simultaneous measurements of multiple gasdynamic parameters in high-speed flows containing water vapor," Appl. Opt. 33, 3296-307, 1994.

[16] V. Nagali and R. K. Hanson, "Design of a Diode-Laser Sensor to Monitor Water-Vapor in High-Pressure Combustion Gases," Appl. Opt. 36, 9518-9527, 1997.

[17] E. R. Furlong, D. S. Baer, and R. K. Hanson, "Real-time adaptive combustion control using diode-laser absorption sensors," Proc.Comb.Symp 27, 103-111, 1998.

[18] J. B. Jeffries, X. Liu, X. Zhou, and R. K. Hanson, "Experimental study of H_2O spectroscopic parameters in the near-IR (6940-7440cm^{-1}) for gas sensing applications at elevated temperature," Journal of Quantitative Spectroscopy and Radiative Transfer 103, 565-77, 2007.

[19] Xin Zhou, Xiang Liu, J. B. Jeffries, and R. K. Hanson, "Development of a sensor for temperature and water concentration in combustion gases using a single tunable diode laser," Meas Sci Technol 14, 1459-68, 2003.

[20] C. Lan, A. W. Caswell, L. A. Kranendonk, S. T. Sanders, Y. Urata, and Y. Okura, "19-color H2O absorption spectrometer applied for real-time in cylinder gas thermometry in an HCCI engine," SAE 2007-01-0188, 2007.

[21] D. W. Mattison, J. B. Jeffries, R. K. Hanson, R. R. Steeper, S. De Zilwa, J. E. Dec, M. Sjoberg, and W. Hwang, "In-Cylinder Gas Temperature and Water Concentration Measurements in HCCI Engines using a Multiplexed-Wavelength Diode-Laser System: Sensor Development and Initial Demonstration" in *31st International Symposium on Combustion*, pp. 791-798, 2007.

[22] L. S. Rothman, D. Jacquemart, A. Barbe, D. C. Benner, M. Birk, L. R. Brown, M. R. Carleer, C. Chackerian Jr., K. Chance, L. H. Coudert, V. Dana, V. M. Devi, J. M. Flaud, R. R. Gamache, A. Goldman, J. M. Hartmann, K. W. Jucks, A. G. Maki, J. Y. Mandin, S. T. Massie, J. Orphal, A. Perrin, C. P. Rinsland, M. A. H. Smith, J. Tennyson, R. N. Tolchenov, R. A. Toth, J. Vander Auwera, P. Varanasi, and G. Wagner, "The HITRAN 2004 molecular spectroscopic database," J. Quant. Spectrosc. Radiat. Transfer 96, 139-204, 2005.

[23] R. J. Barber, J. Tennyson, G. J. Harris, and R. N. Tolchenov, "A high-accuracy computed water line list," Monthly Notices of the Royal Astronomical Society 368, 1087-94, 2006.

[24] L. S. Rothman, A. Barbe, D. C. Benner, L. R. Brown, C. Camy-Peyret, M. R. Carleer, K. Chance, C. Clerbaux, V. Dana, V. M. Devi, A. Fayt, J. M. Flaud, R. R. Gamache, A. Goldman, D. Jacquemart, K. W. Jucks, W. J. Lafferty, J. Y. Mandin, S. T. Massie, V. Nemtchinov, D. A. Newnham, A. Perrin, C. P. Rinsland, J. Schroeder, K. M. Smith, M. A. H. Smith, K. Tang, R. A. Toth, J. V. Auwera, P. Varanasi, and K. Yoshino, "The HITRAN molecular spectroscopic database: edition of 2000 including updates through 2001," J. Quant. Spectrosc. Radiat. Transfer 82, 5-44, 2003.

[25] L. A. Kranendonk, A. W. Caswell, C. L. Hagen, C. T. Neuroth, D. T. Shouse, J. R. Gord, and S. T. Sanders, "High-Pressure Gas-Turbine-Combustor Thermometry Using Wavelength-Agile Absorption Spectroscopy" J. Eng. Gas Turb. Power (submitted) 2006.

[26] C. L. Hagen and S. T. Sanders, "Investigation of multi-species (H_2O_2 and H_2O) sensing and thermometry in an HCCI engine by wavelength-agile absorption spectroscopy," Measurement Science and Technology 18, 1992-1998, 2007.

[27] L. S. Rothman, "The HITRAN Molecular Spectroscopic Database and HAWKS (HITRAN ATMOSPHERIC WORKSTATION): 1996 Edition," J. Quant. Spectrosc. Radiat. Transfer 60, 665-710, 1996.

[28] L. A. Kranendonk, A. W. Caswell, and S. T. Sanders, "Robust method for calculating temperature, pressure and absorber mole fraction from broadband spectra," Appl. Opt. 46, 2007.

[29] V. Nagali and R. K. Hanson, "Design of a diode-laser sensor to monitor water vapor in high-pressure combustion gases," Appl. Opt. 36, 9518-27, 1997.

[30] X. Zhou, J. B. Jeffries, and R. K. Hanson, "Development of a fast temperature sensor for combustion gases using a single tunable diode laser," Appl. Phys. B (Lasers and Optics) B81, 711-22, 2005.

[31] S. Langlois, T. P. Birbeck, and R. K. Hanson, "Temperature-Dependent Collision-Broadening Parameters of H2O Lines in the 1.4 Micron Region Using Diode Lasers Absorption Spectroscopy," J Molecular Spectroscopy 167, 272-281, 1994.

[32] V. Nagali, D. F. Davidson, and R. K. Hanson, "Shock Tube Study of High-Pressure H2O Spectroscopy Near 7100 cm-1" in *AIAA Aerospace Conference Reno,*1999.

[33] G. B. Rieker, X. Liu, H. Li, J. B. Jeffries, and R. K. Hanson, "Measurements of near-IR water vapor absorption at high pressure and temperature," Applied Physics B (Lasers and Optics) B87, 169-78, 2007.

[34] X. Liu, J. B. Jeffries, and R. K. Hanson, "Measurements of spectral parameters of water-vapour transitions near 1388 and 1345 nm for accurate simulation of high-pressure absorption spectra," Meas Sci Technol 18, 1185-94, 2007.

[35] K. V. Price, "Differential Evolution: A Fast and Simple Numerical Optimizer" in *Proceedings of the 1996 Biennial Conference of the North American Fuzzy Information Processing Society - NAFIPS, June 19,1996 - June 22,* "Differential Evolution: A Fast and Simple Numerical Optimizer" IEEE, pp. 524-527, 1996.

[36] R. Storn, "Differential Evolution Design of an IIR-Filter" in *Proceedings of IEEE International Conference on Evolutionary Computation*, "Differential Evolution Design of an IIR-Filter," IEEE, pp. 268-73, 1996.

[37] R. Storn, "On the Usage of Differential Evolution for Function Optimization" in *Proceedings of North American Fuzzy Information Processing*, "On the Usage of Differential Evolution for Function Optimization" IEEE, pp. 519-23, 1996

[38] R. Storn and K. Price, "Minimizing the Real Functions of the ICEC'96 Contest by Differential Evolution" in *Proceedings of IEEE International Conference on Evolutionary Computation*, "Minimizing the Real Functions of the ICEC'96 Contest by Differential Evolution" IEEE, pp. 842-4, 1996.

[39] Y. Bar-Shalom, *Estimation with Applications to Tracking and Navigation*, Wiley, 2001.

[40] G. Herzberg, *Molecular Spectra and Molecular Structure*, Krieger, 1945.

[41] U. Aydin, P. Roth, C. D. Gehlen, and R. Noll, "Spectral line selection for time-resolved investigations of laser-induced plasmas by an iterative Boltzmann plot method," Spectrochimica Acta - Part B Atomic Spectroscopy 63, 1060-1065, 2008.

[42] S. T. Sanders, T. Kim, and J. B. Ghandhi, "Gas temperature measurements during ignition in an HCCI engine," SAE 2003-01-0744, 2003.

[43] G. B. Rieker, H. Li, X. Liu, *et al*, "Rapid Measurements of Temperature and H_2O Concentration in IC Engines with a Spark Plug-Mounted Diode Laser Sensor" in *31st International Symposium on Combustion*, pp. 3041-3049, 2007

[44] M. E. Webber, J. Wang, S. T. Sanders, D. S. Baer, and R. K. Hanson, "In-situ Combustion Measurements of CO, CO2, H2O, and Temperature Using Diode Laser Absorption Sensors," Proc.Combust.Inst. 28, 2000.

[45] E. R. Furlong, D. S. Baer, and R. K. Hanson, "Real-time adaptive combustion control using diode-laser absorption sensors," Symp Int Combust 1, 103-111, 1998.

[46] M. Vidler and J. Tennyson, "Accurate partition function and thermodynamic data for water," J. Chem. Phys. 113, 9766-71, 2000.

[47] G. Durry, V. Zeninari, B. Parvitte, T. Le barbu, F. Lefevre, J. Ovarlez, and R. R. Gamache, "Pressure-broadening coefficients and line strengths of H2O near 1.39 [mu]m: application to the in situ sensing of the middle atmosphere with balloonborne diode lasers," Journal of Quantitative Spectroscopy and Radiative Transfer 94, 387-403, 2005.

[48] I. E. Gordon, L. S. Rothman, R. R. Gamache, D. Jacquemart, C. Boone, P. F. Bernath, M. W. Shephard, J. S. Delamere, and S. A. Clough, "Current updates of the water-vapor line list in HITRAN: A new "Diet" for air-broadened half-widths," Journal of Quantitative Spectroscopy and Radiative Transfer 108, 389-402, 2007.

[49] R. R. Gamache, B. K. Antony, and S. Neshyba, "Self-broadening of water vapor transitions via the complex Robert-Bonamy theory," Journal of Quantitative Spectroscopy and Radiative Transfer 105, 148-63, 2007.

[50] W. Koban, J. D. Koch, V. Sick, N. Wermuth, R. K. Hanson, C. Schulz, J. Walewski, K. Kohse-Hoinghaus, and J. Seitzman, "Predicting LIF Signal Strength for Toluene and 3-Pentanone Under Engine-Related Temperature and Pressure Conditions" in *30th International Symposium on Combustion* pp. 1545-1553, 2005

[51] K. Kohse-Höinghaus and J. B. Jeffries, "Applied Combustion Diagnostics," 2002.

[52] C. Brackmann, J. Bood, M. Afzelius, and P. -. Bengtsson, "Thermometry in internal combustion engines via dual-broadband rotational coherent anti-Stokes Raman spectroscopy," Measurement Science and Technology 15, 13-25, 2004.

[53] L. A. Kranendonk, X. An, A. W. Caswell, R. E. Herold, S. T. Sanders, R. Huber, J. G. Fujimoto, Y. Okura, and Y. Urata, "High speed engine gas thermometry by Fourier-domain mode-locked laser absorption spectroscopy," Optics Express 15, 15115-15128, 2007.

[54] J. W. Walewski, J. A. Filipa, and S. T. Sanders, "Optical beating of polychromatic light and its impact ontime-resolved spectroscopy. Part I: Theory," Appl. Spectrosc. 62, 220-229, 2008.

[55] J. A. Filipa, J. W. Walewski, and S. T. Sanders, "Optical beating in time-resolved spectroscopy. Part II: Strategies for spectroscopic sensing in the presence of optical beating," Appl. Spectrosc. 63, 230-237, 2008.

[56] R. Huber, M. Wojtkowski, and J. G. Fujimoto, "Fourier Domain Mode Locking (FDML): A new laser operating regime and application for optical coherence tomography," Opt. Express 14, 3225-3237, 2006.

[57] Y. Ra and R. D. Reitz, "A reduced chemical kinetic model for IC engine combustion simulations with primary reference fuels," Combust. Flame 155, 713-38, 2008.

[58] Y. Shi, R. P. Hessel, and R. D. Reitz, "An adaptive multi-grid chemistry (AMC) model for efficient simulation of HCCI and DI engine combustion," Combustion Theory and Modelling 13, 83-104, 2009.

[59] E. C. Rea and R. K. Hanson, "Rapid Laser-Wavelength Modulation Spectroscopy Used As a Fast Temperature-Measurement Technique in Hydrocarbon Combustion," Appl. Opt. 27, 4454-4464, 1988.

[60] D. S. Baer, V. Nagali, E. R. Furlong, R. K. Hanson, and M. E. Newfield, "Scanned-Wavelength and Fixed-Wavelength Absorption Diagnostics For Combustion Measurements Using Multiplexed Diode-Lasers," AIAA J. 34, 489-493, 1996.

[61] J. Hult, I. S. Burns, C. F. Kaminski, I. Rahinov, and J. W. Walewski, "Two-line atomic fluorescence flame thermometry using diode lasers," Proc Comb Inst 30, 1535-1543, 2005.

[62] S. T. Sanders, J. A. Baldwin, T. P. Jenkins, D. S. Baer, and R. K. Hanson, "Diode-laser sensor for monitoring multiple combustion parameters in pulse detonation engines," Proceedings of the Combustion Institute 28, 587-594, 2000.

[63] S. Yamashita and M. Asano, "Wide and fast wavelength-tunable mode-locked fiber laser based on dispersion tuning," Optics Express 14, 9299-9306, 2006.

[64] T. Kraetschmer, C. Lan, and S. T. Sanders, "Multiwavelength, Frequency-Division-Multiplexed Light Source Based on Dispersion Mode Locking," IEEE Photon. Technol. Lett. 19, 1607-1609, 2007.

[65] L. Ma, W. Cai, A. W. Caswell, T. Kraetschmer, S. T. Sanders, S. Roy, and J. R. Gord, "Tomographic imaging of temperature and chemical species based on hyperspectral absorption spectroscopy," Optics Express, (in press)

[66] L. A. Kranendonk, R. J. Bartula, and S. T. Sanders, "Modeless operation of a wavelength-agile laser by high-speed cavity length changes," Opt. Express 13, 1498-1507, 2005.

[67] F. Keilmann, C. Gohle, and R. Holzwarth, "Time-domain mid-infrared frequency-comb spectrometer," Optics Letters 29, 1542-1544, 2004.

[68] A. Schliesser, M. Brehm, F. Keilmann, and van der Weide, D. W., "Frequency-comb infrared spectrometer for rapid, remote chemical sensing," Optics Express 13, 9029-9038, 2005.

[69] T. Kraetschmer, J. W. Walewski, and S. T. Sanders, "Continuous-wave frequency comb Fourier transform source based on a high-dispersion cavity," Optics Letters 31, 3179-81, 2006.

[70] T. Kraetschmer, D. Dagel, and S. T. Sanders, "Simple multiwavelength time-division multiplexed light source for sensing applications," Opt. Lett. 33, 738-740, 2008.

[71] S. T. Sanders, "Designs and Applications of Hyperspectral Light Sources," Presented 5 May 2008 at the Conference on Lasers and Electro-Optics (CLEO) conference, San Jose, CA, 2008.

[72] S. T. Sanders, "Frequency Combs and Hyperspectral Sources for Absorption Spectroscopy," Presented 5 May 2008 at the Conference on Lasers and Electro-Optics (CLEO) conference, San Jose, CA, http://digital.library.wisc.edu/1793/28167, 2008.

[73] R. J. Bartula and S. T. Sanders, "Estimation of Signal Noise Induced by Multimode Optical Fibers," Opt. Eng. 47, 2008.

[74] R. J. Bartula, B. L. Conrad, and S. T. Sanders, "Estimation of Noise Induced by Multimode Optical Fibers in Optical Sensor Systems," Presented Thursday 16 August 2007 at the Gordon Research Conference on Laser Diagnostics for Combustion, Oxford, United Kingdom, http://digital.library.wisc.edu/1793/28229, 2008.

[75] X. Liu, J. B. Jeffries, and R. K. Hanson, "Measurement of Non-Uniform Temperature Distributions using Line-of-Sight Absorption Spectroscopy" in *44th AIAA Aerospace Sciences Meeting 2006, January 09,2006 - January 12*, American Institute of Aeronautics and Astronautics Inc, pp. 10029-10042, 2006